EVALUATION OF THE MECHANICAL PROPERTIES FOR REVERSION HEAT TREATED THERMALLY EMBRITTLED DUPLEX STAINLESS STEEL

Thesis

Submitted in partial fulfillment of the requirements for the degree of

DOCTOR OF PHILOSOPHY

By

SHAMANTH V.

DEPARTMENT OF METALLURGICAL AND
MATERIALS ENGINEERING
NATIONAL INSTITUTE OF TECHNOLOGY KARNATAKA,
SURATHKAL, MANGALORE – 575025
KARNATAKA STATE, INDIA

February 2018

D E C L A R A T I O N

I hereby *declare* that the Research Thesis entitled **"EVALUATION OF THE MECHANICAL PROPERTIES FOR REVERSION HEAT TREATED THERMALLY EMBRITTLED DUPLEX STAINLESS STEEL"** which is being submitted to the **National Institute of Technology Karnataka, Surathkal** in partial fulfillment of the requirements for the award of the Degree of **Doctor of Philosophy** in **Department of Metallurgical and Materials Engineering** is a *bonafide report of the research work carried out by me*. The material contained in this Research Thesis has not been submitted to any University or Institution for the award of any degree.

Register Number : **123013MT12FO5**

Name of the Research Scholar : **Shamanth V.**

Signature of the Research Scholar :

Department of Metallurgical and Materials Engineering

Place : NITK-Surathkal

Date :

C E R T I F I C A T E

This is to *certify* that the Research Thesis entitled **"EVALUATION OF THE MECHANICAL PROPERTIES FOR REVERSION HEAT TREATED THERMALLY EMBRITTLED DUPLEX STAINLESS STEEL"** submitted by **Mr. Shamanth V.** (**Register Number: 123013MT12FO5**) as the record of the research work carried out by him, is *accepted as the Research Thesis submission* in partial fulfillment of the requirements for the award of degree of **Doctor of Philosophy.**

Research Guide(s)

Dr. Ravishankar K. S.

Assistant Professor

Department of Metallurgical and Materials

Engineering

NITK, Surathkal

Chairman - DRPC

Date:

ACKNOWLEDGEMENTS

With a deep sense of gratitude, I wish to express my sincere thanks to my supervisor **Dr. Ravishankar K. S.**, Department of Metallurgical and Materials Engineering, National Institute of Technology Karnataka (N.I.T.K), Surathkal, for his excellent guidance and support throughout the work. I received very useful, encouraging and excellent academic feedback from him, which has stood in good stead while writing this thesis. His constant encouragement, help and review of the entire work during the course of the investigation are invaluable. I profoundly thank him.

I take this opportunity to thank **Dr. Udaya Bhat K**, Associate Professor and Head, Department of Metallurgical and Materials Engineering for his continuous and timely suggestions.

I wish to thank all the members of the Research Program Assessment Committee including **Dr. H S Nagaraja,** Assistant Professor, Department of Physics and **Dr. Preetham Kumar G.V,** Assistant professor, Department of Metallurgical and Materials Engineering for their appreciation and criticism all through this research work.

I acknowledge the funding support from NITK-Surathkal and experimental facility provided by the CMTI Bangalore, department of Mechanical Engineering PESIT Bangalore and department of Metallurgical and Materials Engineering at NITK-Surathkal.

I wish to express my sincere gratitude to all the faculty members of the Department of Metallurgical and Materials Engineering, N.I.T.K Surathkal for their help, encouragement and support all through this research work.

My sincere thanks to all my lab mates Mr. Prashanth, Mr. Palaksha., Mr. Sangamesh., Mr. Natesh M., and Mr. Arun T N., for their help and support to carry out this dissertation work.

I am indebted to my friends Mr. Nivish George, Mr. Hemanth K., Mr. Gangadhar N., Mr. H. S. Nithin, Mr. Rakesh K Rajan, Mr. Kiran Bharani, Mr. Sandeep B.N., Mr. Rakesh N., Mr Mohan kumar R., Mr. Naveen kumar H., Puneeth and Mr. H. S. Ashrith for their constant help and encouragement during the entire research work.

Finally, I would like to thank my parents who have trusted me throughout my life. I would like to share this moment of happiness with my parents, Raghu Mani and Vasanth Kumar K. R.; My wife Shruthi S B., sister Ekatha and my brother-in-law Darshan S L. for their constant encouragement.

Shamanth V.

Abstract

The thermal aging embrittlement of duplex stainless steels is one of the key material property degradation that would limit their industrial applicability. In this investigation, we study the effect of reversion heat treatment on the mechanical properties of the thermally embrittled steels. The samples were solutionized, aged, reversion heat treated and re-aged. The tensile strength of the aged sample had increased with respect to the solutionized condition because in aged condition, the ferrite phase was spinodally decomposed into iron rich alpha (α) and chromium rich alpha-prime (α') precipitates and also the chromium nitride precipitates was found along with these precipitates.

The 60 minutes reversion heat treated samples showed a maximum recovery in tensile strength of upto 92% with respect to the solutionized condition because the temperature of 550 ^{0} C is above the (α + α') miscibility gap, the ferritic phase was homogenized again. In other words, Fe-rich α and Cr-rich α' prime precipitates which were formed during ageing become thermodynamically unstable and dissolve inside the ferritic phase. As the reversion heat treatment time was increased the recovery induced was decreasing because of the formation of the secondary austenite and R-phase in the ferrite phase.

The 60 minutes reversion heat treated sample was then again re-aged at 475 ^{0} C for varying periods inorder to check the re-embrittlement rate and the applicability of the reversion heat treatment. The tensile and impact strength had again increased significantly, which was almost similar to that of the aged sample and there was no much difference in the re-embrittlement rate. The high resolution transmission microscopy revealed that the spinodal decomposition again remained as the primary mechanism for the embrittlement of the ferrite phase.

From fatigue test it was clear that fatigue strength was sensitive to the heat treatment condition. In this study the fatigue strength in embrittled state was higher than solutionized and reversion heat treated condition. In all heat treated conditions, the major resistance to crack growth came from α/γ phase boundaries because the α/γ phase boundary offers more resistance to the slip transfer as compared to α/α and γ/γ grain boundaries.

TABLE OF CONTENTS

List of Figures

Figure **Page**

List of Tables

Chapter 1 Introduction

Stainless steels are alloys of iron containing at least 11% chromium by weight. They exhibit superior corrosion resistance compared to other steels mainly due to the passive film of chromium oxide which forms on the surface. However, in order for a stainless steel to retain its "stainless-ness" in aggressive chemical environments, larger amounts of chromium needs to be added to the alloy (Lippold and Kotecki 2005). In addition to chromium, other alloying elements such as nickel, molybdenum, manganese, nitrogen etc. are also added in order to provide better resistance to different forms of corrosion. Some alloying elements are also added to enhance mechanical properties and weldability without compromising on the corrosion resistance (Ki Leuk Lai et al. 2012). Stainless steels can be classified into five groups based on their microstructures: Ferritic, Austenitic, Martensitic, Duplex and Precipitation Hardening stainless steels (Davis 1994).

Duplex stainless steels (DSS) have a microstructure consisting of ferrite and austenite in nearly equal proportions and exhibit better corrosion resistance and mechanical properties in comparison to single phase stainless steels (Kazior et al. 2004). They provide excellent resistance to pitting corrosion and stress corrosion cracking even in chloride environments (Singh Raman and Siew 2010). DSS can be classified into three families based on their pitting resistance equivalent numbers (PREN). They are: "lean duplex" alloys having a PREN slightly higher than that of austenitic stainless steel grades and contain up to 20 wt% Cr and no molybdenum, "standard duplex" alloys with around 22 wt% Cr and 3 wt% Mo, having a PREN lying between 33 and 36, and, "superduplex" alloys with more than 25 wt% Cr, 3.5 wt% Mo and 0.2 - 0.3 wt% N, with a PREN greater than 40. Recently, special grades called "hyperduplex" stainless steels with much higher chromium and nitrogen levels have also been developed (Alvarez-Armas and Degallaix-Moreuil 2009).

DSS find applications in various industries which involve hostile environments and such as chemical and petrochemical, oil and gas, pulp and paper, power generation, hydrometallurgy, marine transportation, construction etc. which involve hostile environments (Gunn 1997). A major limiting factor in the applicability of DSS is their susceptibility to thermal embrittlement when exposed to temperatures in the range of 280 to 525 ^{0} C. This

form of embrittlement is popularly known as "475 ^{0} C embrittlement" since the rate of embrittlement within this temperature range is maximum at 475 ^{0} C (Chung 1992). The embrittlement is believed to be because of the formation of Cr-rich precipitates called "α'" in the ferrite phase. The embrittlement is accompanied by a drop in corrosion resistance because of the depletion of chromium levels within the ferrite phase and around the precipitates (Chen et al. (2002).

Studies conducted on ferritic and duplex stainless steels have shown that the changes in microstructure and mechanical properties associated with the 475 ^{0} C embrittlement can be undone by subjecting the material to a short term "reversion" heat treatment within the range of 550-600 ^{0} C (Konosu 1992). Although the effect of subjecting a 475 ^{0} C embrittled DSS to reversion heat treatment has been studied by investigators in the past. In our investigation the focus was mainly on the recovery of microstructure and mechanical properties. However, when cast austenitic stainless steels are exposed to the 550 ^{o}C or higher for a long time, various types of detrimental intermetallic phases, such as sigma (σ) phase, Chi (χ) phase, R phase, and $M_{23}C_6$ carbides could be formed in the ferrite phase or at ferrite phase boundaries. As a result, the mechanical properties will be significantly degraded (Gunn, R. 1997). Therefore, to apply the reversion heat treatment to alleviate the thermal aging embrittlement, the possibility of inadvertent embrittlement of DSS by the reversion heat treatment has been carefully investigated. However, it was not completely clear that how these microstructural changes translate on mechanical properties of DSS and vice-versa. In addition, there was a concern that the recovered DSS after the reversion heat treatment could be re-embrittled faster when it is subjected to the service temperature of nuclear power plants (Jang, H. et.al 2014). Therefore, understanding the re-aging behaviors of the recovered DSS is also important to determine the applicability of the reversion heat treatment. In this regard, the Scope of present work was aimed to develop an economic approach to extend the service life of long term working duplex stainless steel components which are susceptible for embrittlement.

The objectives of the research program are outlined below:

1. To study the effect of 475 ^{0} C embrittlement on the tensile properties (viz. ultimate tensile strength, yield strength and ductility), impact and fatigue behavior of solutionized DSS and correlate with its microstructure using scanning electron microscopy and transmission electron microscopy.
2. To study the changes in microstructure, tensile, impact and high cycle fatigue properties, after reversion heat treatment of a thermally embrittled S2250 duplex stainless steel for varying periods
3. To study the strain hardening behavior of the material after reversion heat treatment.
4. To correlate the variation in strain hardening exponent with the deformation behavior.
5. To find the optimum reversion time required to obtain maximum recovery of properties.
6. To study the effect of re-aging on the microstructure, tensile and impact behavior of the reversion heat treated S2205 DSS.

The thesis is divided into five chapters which includes the introduction as first chapter. The second chapter summarizes the outline of the theoretical background based on which the scope of the present investigation was defined. The experimental techniques employed to achieve the objectives of the present investigation are described in the third chapter. The results obtained during the present investigation are presented and discussed with the results obtained by other international research groups in the fourth chapter. The concluding remarks and scope for further research in this area of investigation are discussed in the fifth chapter.

Chapter 2 Literature Review

2.1 Duplex Stainless Steels: Development and applications

The development of stainless steels began in the early twentieth century in the United Kingdom and Germany. The austenitic Fe-Cr-Ni steels became the largest group of stainless steels even though the earliest grades were martensitic and ferritic Fe-Cr steels. The minimum carbon levels in these steels were high (around 0.08%), due to existing furnaces and refining techniques, making them prone to grain boundary carbide precipitation during heat treatment and welding, and sensitive to intergranular corrosion attack.

The first reference to Fe-Cr-Ni duplex stainless steels with between 30% and 70% ferrite was made by Bain and Griffith in 1927. Soon after, several countries explored such steels in cast form. The first commercial duplex stainless steel product, a grade called 453E, was made in 1929 with an approximate composition of 25%Cr-5%Ni followed by a modified grade, 453S, with 25%Cr-5%Ni-1%Mo which was marketed in 1932. Applications in the form of castings involved autoclaves for gunpowder production and valves for sulphide pulping and as coolers of the Brobeck type in the form of plate and forgings. By the late 1940's, duplex stainless steels with high volume fractions of ferrite in an austenitic matrix, which were not sensitive to intergranular corrosion (IGC) even in the most aggressive media were available and marketed simultaneously in France, Sweden and the USA.

Development of low nickel-content duplex alloys was encouraged due to nickel shortage following the Korean War in 1950-51, and it became apparent that a balance of ferrite and austenite provided better resistance to stress corrosion cracking (SCC) in chloride medium than fully austenitic grades. In France a grade with 20-35% ferrite called UR50 (UNS32404) was marketed in various forms for industries such as oil refining, food processing, pulp and paper, and pharmaceuticals. These steels were produced in high frequency induction furnaces with a partial vacuum that ensured carbon removal, rudimentary de-oxidation and restricted nitrogen ingress.

The understanding of the physical metallurgy of DSS had not progressed sufficiently to offer a material having good ductility and toughness that was easy to manufacture and

fabricate. This gave them a reputation for crack sensitivity until the 1960s. During the late 1960s and early 1970s, there was another nickel shortage and pushed the price of austenitic alloys. With the introduction of vacuum and argon oxygen decarburization practices, steel production techniques had improved dramatically, leading to steels with low carbon, sulphur and oxygen contents along with greater control of nitrogen content. The maximum carbon content in the UNS S31500 was 0.03%. The chemical composition was controlled to optimize the ferrite-austenite phase balance and to enhance resistance to SCC. The addition of nitrogen improved corrosion resistance and stability of austenite in the heat affected zone (HAZ). However, they were still susceptible to IGC under certain conditions due to high Cr/Ni equivalent ratio, which led to an almost fully ferritic HAZ after welding. Carbides and nitrides precipitated along grain boundaries because of the very low solubility of carbon and nitrogen in ferrite. Higher levels of nickel and nitrogen were added to overcome this problem and the IGC resistance was significantly improved.

Through the 1970s and 1980s, several duplex grades were developed with emphasis on improved weldability and better resistance to corrosion in aggressive environments. Highly alloyed duplex grades such as the UNS S32550 with 25% Cr and up to 2% Cu, were developed as castings such as pumps and valves, and have been used extensively in the offshore industry and for sulphuric acid service. The superduplex grades containing about 25%Cr, 6-7%Ni, 3-4%MO, 0.2-0.3%N, 0-2%Cu and 0-2% W have pitting resistance equivalent numbers (PREN) greater than 40. In making superduplex alloys, care was taken to balance the Cr and Ni forming elements and higher levels of nitrogen were added. These factors stabilized the Heat affected zone (HAZ) during welding, but promoted intermetallic precipitation (Gunn R. 1997).

Table 2.1 shows the common grades of duplex stainless steels and their nominal compositions (in wt %). In recent years duplex grades have emerged as an alternative to austenitic grades such as 316 and 304. Lean DSS are used in bridges, storage tanks and also for construction of transport vehicles. Super duplex grades such as Zeron 100 (UNS S32760) were developed to compete with super austenitic grades and are used in large quantities in umbilical’s for the control of sub-sea systems. DSS have also replaced austenitic grades in flue gas cleaning systems and desalination plants (Liljas 2008).

In natural gas pre-heaters, S32304 are selected for exchanger tubing where grade steam low is used for heating purposes. For applications where higher chloride contents are present, tubing is made from S31803/S32205. This grade is also used for reactors, storage tanks and heat exchangers in the production of detergents comprising of fatty amines and chlorides, in plastic production, in steam sterilization of bi-products of sodium cyanide production and so on. Cast 32550 is used in phosphoric and sulphuric acid production and also as stud bolts in ammonia injectors and valve internals in urea recycle lines.

Grade S31803/S32205 has been extensively used for the construction of advanced chemical tankers for marine transportation since 1987. Duplex grades are also used as propeller shafts, thrusters, water jet engines and other components subjected to high mechanical loads. Super duplex grades such as S32760 are used in pumps to handle potash at around 80 ^{0} C and hot bauxite slurry in the Bayer process. Other uses for this grade include pipe work in a titanium dioxide refinery for spent hydrochloric acid lines. Low alloy grades such as S32304 are selected for water heaters, calorifiers and hot water tanks in breweries and similar industries (Gunn R. 1997). The cast DSS of the CF series finds applications in nuclear power plants for reactor coolant and auxiliary system piping (Byun and Busby 2012).

Table 2.1 Common grades of Duplex Stainless Steels and their nominal compositions (in Wt %)

UNS Number	Common Name	C	Mn	P	S	Si	Cr	Ni	Mo	N	Cu
S32750	2507	0.03	1.2	0.035	0.02	0.8	24-26	6-8	3-5	0.24-0.32	0.5
S32205	2205	0.03	2.0	0.03	0.02	1.0	22-23	4.5-6.5	3.0-3.5	0.14-0.2	……
S32304	2304	0.03	2.5	0.04	0.03	1.0	21.5-24.5	3-5.5	0.05-0.60	0.05-0.2	0.05-0.6
S32001	2101	0.03	5.0	0	0	0.7	21.5	1.5	0.3	0.22	0.3

2.2 Metallurgy of Duplex Stainless Steels

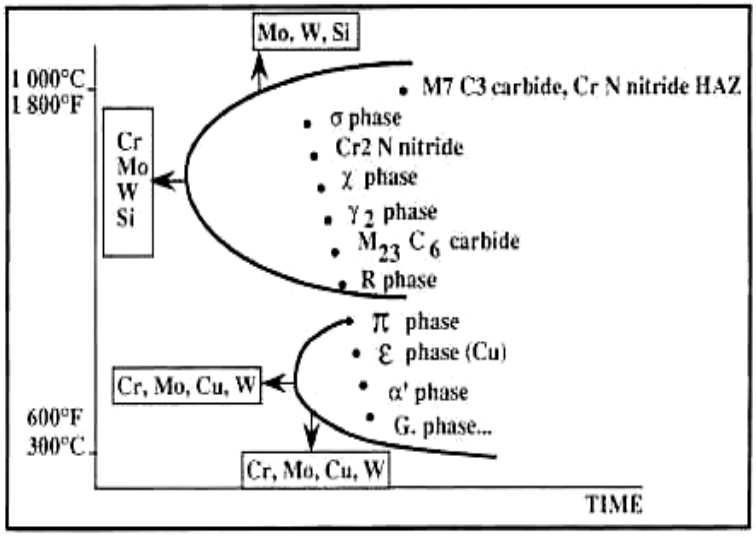

Figure 2.1 A schematic TTT curve for formation of precipitates in DSS and the effects of alloying elements in the temperature ranges of formation for various precipitates (Gunn 1993).

During solidification of the DSS melt, the first solid that forms is δ-ferrite. As the temperature drops, austenite formation takes place. After complete solidification, the microstructure is that of austenite islands in a matrix of ferrite. The volume fraction of ferrite-austenite depends on the chemical composition. The large amounts of alloying elements added to DSS results in the formation of various carbides, intermetallic and other secondary phases which form over different temperature ranges at varying rates (Figure 2.1).

2.2.1 Secondary Phases

2.2.1.1 Sigma phase

The Sigma (ζ) phase is a Cr, Mo rich hard embrittling precipitate which forms between 650 and 1000 ^{0} C is often associated with reduction in impact toughness and corrosion resistance (Gunn R. 1997). Since the mobility and concentration of Mo and Cr in ferrite is higher than in austenite, ζ-phase precipitation generally occurs in the ferrite phase. It also forms in the HAZ during welding. It has a tetragonal crystal structure with 32 atoms per unit cell and 5 different crystallographic atom sites. The morphology of ζ-phase changes with

temperature. At around 750 ^{0} C, it has a coral-like structure; at 950 ^{0} C it is bigger and more compact (Pohl et al. (2007).

The depletion in Mo content is a lot more pronounced compared to that of Cr, indicating that Mo is the main element controlling the precipitation of ζ-phase. The formation of ζ-phase is rapid and a very high cooling rate is required to avoid it formation during quenching from solutionising temperature. For a 2205 DSS, a cooling rate of 0.23K/s is necessary to avoid more than 1% ζ-phase formation (Sieurin and Sändstorm 2007).

2.2.1.2 Chi phase

The enrichment of ferrite with intermetallic forming elements during long term thermal exposure at temperatures around 700 ^{0} C, favors the precipitation of Chi (χ) phase. It often nucleates at the δ/γ interface and grows into the δ matrix (Redjaimia et al. 1991). It is difficult to study its influence on corrosion and toughness since it often co-exists with ζ-phase (Gunn R. 1997). Increase in ageing time causes an enrichment of Mo and depletion of Fe in the χ-phase (Michalska and Sozanska 2006). During isothermal ageing, the χ-phase always precipitates before ζ-phase, but during continuous cooling, χ-phase appears only at low cooling rates (Calliari et al. 2010).

2.2.1.3 Secondary Austenite

The mechanism and rate of formation of secondary austenite (γ_2) may vary depending on the temperature. In the temperature range of 700-900 ^{0} C, typical mechanism is by the eutectoid reaction, which is facilitated by rapid diffusion along the δ/γ boundaries giving rise to ζ-phase and γ_2 in prior ferrite grains. This also reduces the Cr and Mo content in the ferrite. When Cr2N precipitates cooperatively, γ_2 has been found to be poor in Cr, making it highly susceptible to pitting corrosion. At temperatures above 650 ^{0} C, at which diffusion rates are higher, γ_2 is formed as Widmanstätten precipitates. Below 650 ^{0} C, ferrite transforms to γ_2 by a mechanism quite similar to that of martensite formation. The γ_2 formed in this manner has a similar composition to the ferritic lattice thus indicating that the transformation was diffusionless (Nilsson 1992).

2.2.1.4 R-phase

Isothermal treatment of duplex stainless steels between 550 and 650 ^{0} C results in the uniform and very fine distribution of R-phase throughout the δ grains (Redjaimia et al. 1991). The R-phase is a Mo rich intermetallic having a trigonal crystal structure. Its formation reduces the toughness and critical pitting temperature in DSS. R-phase precipitates may be intergranular or intragranular in nature; the former perhaps more deleterious with regard to pitting corrosion since they may contain up to 40% Mo (Nilsson 1992). With the increase in ageing time, R-phase transforms into ζ-phase due to diffusion of Mo from the R-phase into the ζ-phase, which eventually results in the decrease in the volume fraction of R-phase (Hwang et al. 2014).

2.2.1.5 Chromium Nitrides

The solubility of nitrogen at about 1000 ^{0} C in ferrite is high, but drops on cooling and the ferrite becomes supersaturated in nitrogen, leading to the intergranular precipitation of needle-like Cr_2N (Gunn R. 1997). Isothermal heat treatment in the temperature range of 700 to 900 ^{0} C usually results in precipitation of Cr_2N either on the δ/δ grain boundaries or the δ/γ phase boundaries. The hexagonal Cr_2N formed under these conditions has a negative influence on pitting corrosion resistance. In HAZ of welds, however, the cubic Cr_2N is the predominant nitride that has been observed (Nilsson 1992). Cr_2N precipitates display film-like or tiny platelet-like morphology (Jinson 2001).

2.2.1.6 Carbides ($M_{23}C_6$ and M_7C_3)

M_7C_3 forms at the δ/γ grain boundaries in the temperature range of 950-1050 ^{0} C but can be avoided by ordinary quenching methods since its formation takes at least 10 minutes. $M_{23}C_6$ precipitates rapidly between 650 and 950 ^{0} C, predominantly at the δ/γ boundaries where Cr-rich ferrite intersects with C-rich austenite. Several precipitate morphologies have been recorded including cuboidal, acicular and cellular form; each having an associated Cr depleted zone in its vicinity. Since modern duplex grades contain less than 0.02%C, carbides of either form are rarely seen (Gunn R. 1997).

2.2.1.7 Alpha Prime

Alpha Prime (α′) is a Cr-rich precipitate that forms in the temperature range of 280-525 ^{0} C (Chung 1992). The main cause for formation of α′is the miscibility gap in the Fe-Cr system whereby ferrite undergoes spinodal decomposition into Fe-rich δ-ferrite and Cr-rich α′. Within the miscibility gap but just outside the spinodal, classical nucleation and growth of α′ occurs. The α′ precipitate has a body-centered crystal structure and is the main cause of hardening and 475 ^{0} C embrittlement in ferritic stainless steels (Gunn R. 1997).

2.2.1.8 Epsilon phase

In duplex alloys containing copper, the supersaturation of ferrite due to decrease in solubility at lower temperatures leads to the precipitation of extremely fine particles of Cu-rich Epsilon (ε) phase within the ferrite grains after 100 hours at 500 ^{0} C. This significantly extends the low temperature hardening range for duplex stainless steels. Often, ε-phase has been mistaken for γ2 due to similar temperature ranges of formation (Gunn R. 1997).

2.2.1.9 G, π and τ phases

The G-phase develops at α/α′ interfaces between 300 and 400 ^{0} C after several hours of exposure, due to enrichment of Ni and Si at these locations (Gunn R. 1997).

The π-nitride is a Cr and Mo rich precipitate with a cubic crystal structure that forms at intergranular sites in DSS welds after isothermal treatment at 600 ^{0} C for several hours (Gunn R. 1997).

The η-phase is a heavily faulted precipitate with needle-like morphology that forms due to heat treatment in the temperature range of 550-650 ^{0} C. It has an orthorhombic crystal structure (Redjaimia et al. 1991).

2.3 Effect of alloying elements

2.3.1 Chromium

The primary role of chromium in stainless steels is to improve the localized corrosion resistance, by the formation of a passive Cr-rich oxy-hydroxide film. This film extends the passive range and reduces the rate of general corrosion. The beneficial effect of adding very

high levels of chromium is, however, negated by the enhanced precipitation of intermetallic phases which often lead to a reduction in ductility, toughness and corrosion resistance. Apart from this chromium also stabilizes ferrite (Gunn R. 1997). Although, other alloying elements can influence the effectiveness of the passive film, none of them can create the properties of stainless steel, by themselves. However, it is often more efficient to improve corrosion resistance by addition of other elements, with or without increasing the chromium content to ensure that the mechanical properties, fabricability, weldability or high temperature stability remain largely unaffected (Davison et al. 1987).

2.3.2 Nickel

Nickel, when added in sufficient quantities, stabilizes austenite; this greatly enhances mechanical properties and fabrication characteristics. Nickel effectively promotes re-passivation, especially in reducing environments and is particularly useful in resisting corrosion in mineral acids. Increasing nickel content to about 8-10% decreases resistance to SCC, but on further increase, SCC resistance is restored and is achieved in most service environments at about 30%Ni (Davison et al. 1987).

In order to maintain 40-60% ferrite, balance austenite in DSS, the ferrite stabilizing agents need to be balanced with the austenite stabilizers. For this reason, the level of nickel added to a DSS will depend primarily on the chromium content. Excessive nickel contents may enhance intermetallic precipitation when the alloy is exposed to the temperature range of 650-950 ^{0} C, due to enrichment of ferrite in Cr and Mo. High Ni contents also accelerate α' formation. Although nickel does have some direct effect on corrosion properties, it appears that its main role is to control phase balance and element partitioning (Gunn R. 1997).

2.3.3 Molybdenum

Molybdenum, in combination with chromium, effectively stabilizes the passive film in the presence of chlorides. Molybdenum is effective in increasing the resistance to the initiation of pitting and crevice corrosion (Davison et al. 1987). Its effect on ferrite stability is similar to that of chromium. To prevent ζ-phase formation in the hot working temperature range, i.e. above 1000 ^{0} C, the upper limit of Mo addition of is limited to about 4% (Gunn R.

1997), since Mo is the main element controlling the precipitation of ζ-phase (Sieurin and Sandstrom 2007).

2.3.4 Manganese

Although manganese acts as an austenitic stabilizer in austenitic stainless steels, mixed results have been obtained for DSS in which it has little effect on the phase balance. It appears that Mn increases the temperature range and formation rate of ζ-phase. Manganese increases abrasion and wear resistance and tensile properties of stainless steels without loss of ductility. Further, Mn increases the solubility of nitrogen, thus allowing for higher nitrogen contents. However, Mn additions in excess of 3% and 6%, for nitrogen levels of 0.1% and 0.23% respectively, significantly decrease the critical pitting temperature (CPT). Nevertheless, the combination of Mn and N in modern DSS improves the pitting resistance and counteracts the singular problems associated with Mn (Gunn R. 1997).

2.3.5 Nitrogen

Nitrogen enhances pitting resistance by retarding the formation of ζ-phase and diminishes Cr and Mo segregation and also raises the corrosion resistance of the austenitic phase in DSS (Davison et al. 1987). Nitrogen has also been reported to increase crevice corrosion resistance. Nitrogen strengthens austenite by dissolving at the interstitial sites in solid solution. Addition of nitrogen to DSS, suppresses austenite dissolution and encourages austenite reformation in the HAZ (Gunn R. 1997).

2.3.6 Copper

Copper reduces the corrosion rate of high alloy austenitic grades in non-oxidising environments, such as sulphuric acid. In some DSS with 25% Cr, 1.5% Cu is added to obtain the optimum corrosion resistance in 70% H_2SO_4 at 60 ^{0} C. For boiling HCl, an addition of 0.5% Cu decreases both active dissolution and crevice corrosion rates. Copper additions in DSS are limited to about 2%, since higher levels, reduce hot ductility and can lead to precipitation hardening. Exposure at temperatures between 300-600 ^{0} C can lead to precipitation of tiny Cu-rich precipitates which do not significantly reduce corrosion

resistance or toughness but can be exploited for improving abrasion-corrosion resistance in duplex pump castings (Gunn R. 1997).

2.3.7 Tungsten

Up to 2% tungsten additions have been made in DSS to improve pitting resistance. Tungsten also increases crevice corrosion resistance in heated chloride solutions. Tungsten encourages intermetallic formation in the 700-1000 ^{0} C temperature range, and also encourages γ_2 formation in weld metal. Thermodynamically, it is believed to be equivalent to Mo with respect to ζ-phase formation, but this is not the case in terms of kinetics. Levels between 1% and 3% have been shown to restrict ζ-phase formation to the intergranular sites instead of phase boundaries; the influence of the large tungsten atom on the diffusion of Mo and W at the phase boundaries is thought to be the reason. Tungsten alloyed weld metal has been shown to form χ-phase more rapidly than in welds without W additions. Generally, the tungsten content is limited to 1% in a 4% Mo DSS, and 2% in DSS with about 3% (Gunn R. 1997).

2.3.8 Silicon

Silicon enhances high temperature oxidation resistance and is also beneficial for concentrated nitric acid service. DSS bearing high silicon (3.5 to 5.5%) have enhanced pitting corrosion resistance and a claimed immunity to SCC. However, it is preferred to limit Si additions to 1% since Si is generally considered to enhance ζ-phase formation (Gunn R. 1997).

2.3.9 Carbon, sulphur and phosphorous

The carbon content of most wrought DSS is limited to 0.02 to 0.03%, primarily to suppress precipitation of Cr-rich carbides along the grain boundaries. Sulphur and phosphorous contents are controlled but not eliminated. The presence of S is important for weld bead penetration. Modern steel making processes such as Argon Oxygen Decarburization (AOD) and Vacuum Oxygen Decarburization (VOD) help in controlling the levels of S and C, while P contents can be reduced by using good melting practice (Gunn R. 1997).

2.4 Effect of Heat Treatment

2.4.1 Solution annealing

Element solubility in ferrite falls with decreasing temperature, increasing the probability of precipitation during heat treatment. During solidification, DSS solidifies completely as ferrite and then undergo solid state transformation into austenite. This is a reversible process and as a result, any large increases in temperature above 1000 ^{0} C lead to an increase in ferrite and also a reduction in the partitioning of substitutional elements between phases. In addition, ferrite becomes enriched in interstitial elements such as carbon and nitrogen.

Heat treatment in the temperature range 1100-1200 ^{0} C can have a dramatic influence on the microstructure of a wrought product. Prolonged treatment at high temperatures can lead to equiaxed grains, whereas, cooling at intermediate rates can render the grains acicular, with Widmannstätten morphology. Step quenching, with or without simultaneous mechanical strain can lead to a dual structure, consisting of both coarse and fine austenite grains.

Duplex alloys with high contents of Cr, Mo and W are most susceptible to intermetallic precipitation. Mo and W extend the stability range of intermetallics to higher temperatures. For this reason, higher solution annealing temperatures, i.e. above 1000 ^{0} C are necessary. In order for the precipitates to re-dissolve, solution annealing temperatures for superduplex grades must be performed at 1050 ^{0} C and above. For grades such as S32550 and S32750, a few minutes at 1050-1070 ^{0} C are sufficient, whereas, for tungsten bearing grades such as S32760, 1100 ^{0} C has been recommended (Gunn R. 1997). Lo et al. 2011, during their investigation of a hyper duplex stainless steel without W additions, solution annealed the samples at 1100 ^{0} C for 1 hour and obtained a microstructure of ferrite and austenite with no secondary phases. Jeon et al. 2012 solution treated a hyper duplex alloy with high W additions at 1090 ^{0} C for 30 minutes and found no secondary phases.

2.4.2 The 475 ºC embrittlement

Reidrich and Loib (1941) were the first to report embrittlement, caused by elevated temperature exposure of iron–chromium alloy system. They conducted bend test and observed that steels containing 19–23 wt. % chromium showed poor ductility after

1000 hours exposure at 500 ºC. However, the ductility was not impaired when the samples were aged at 550 ºC. This observation indicated that the embrittlement is sensitive to temperature in a very narrow range. (Fisher et al. 1953) were the first to suggest the decomposition of the ferritic phase in a binary iron–chromium alloy to chromium-rich phase (α') and an iron-rich phase (α), in the temperature range of 280–500 ºC. They observed fine spherical precipitates of diameter 200Å in steel samples containing 28.5 wt. % chromium aged at 475 ºC for 1–3 years. The precipitate observed by them had BCC structure containing about 80 at.% chromium and was non-magnetic in nature. The lattice parameter of these precipitates was reported to be between that of iron and chromium. After the detection of precipitates caused by aging treatment and the resulting embrittlement, the focus of research shifted to identify the phases in iron–chromium binary alloy system in the temperature range of 280–500 ºC that cause the embrittlement.

R.O. William (1958) was the first to propose explicitly, the existence of a miscibility gap in the iron–chromium phase diagram in the temperature range of 280–500 ºC as the cause of precipitation of α′ as shown in Figure 2.2 (a). According to the phase diagram as shown in the figure 2.2 (b) 475 ºC embrittlement may be expected at temperatures below 516 ºC in the composition range of 12–92 wt.% chromium in iron–chromium binary alloy system. So this study was a confirmation of the earlier study by Reidrich and Loib (1941) on the redissolution of α′ precipitate when aged at 550 ºC. Blackburn and Nutting (1964) completely redissolved the α′ after 24 hours of aging at 550 ºC. The neutron diffraction studies conducted by Vintaikin and Loshmanov (1966) confirmed the clustering and decomposition of ferritic phase in the temperature range of 280–500 ºC.

Some of the critical reviews on the theory of decomposition in metastable ferritic alloys were done by Cahn (1961) and Hilliard (1970). These reviews discussed the thermodynamical distinction within the miscibility gap in: (a) spinodal decomposition; (b) nucleation and growth of α′. Spinodal decomposition refers to a reaction where two phases of the same crystal lattice type, but different compositions and properties, form due to the existence of a miscibility gap in the alloy system by means of uphill diffusion without nucleation. Thermodynamically this is possible at concentration between the points where the second derivative of the free energy with composition equals zero. This phase separation

process occurs at a very fine scale (of the order of only a few nanometers) and the presence of the α′ phase can only be detected through an atom probe field ion microscope (Grobner, P. J. 1973).

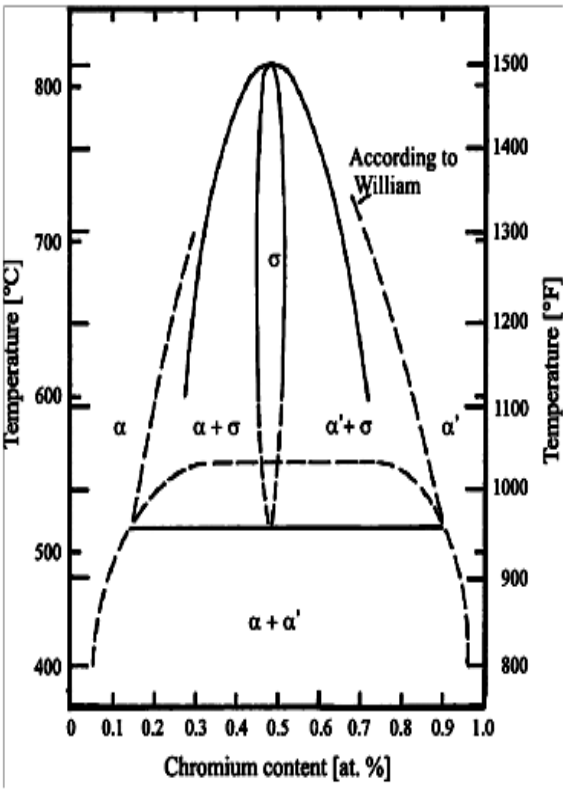

Figure 2.2(a) Phase diagram of the iron–chromium binary system (R.O. William 1958).

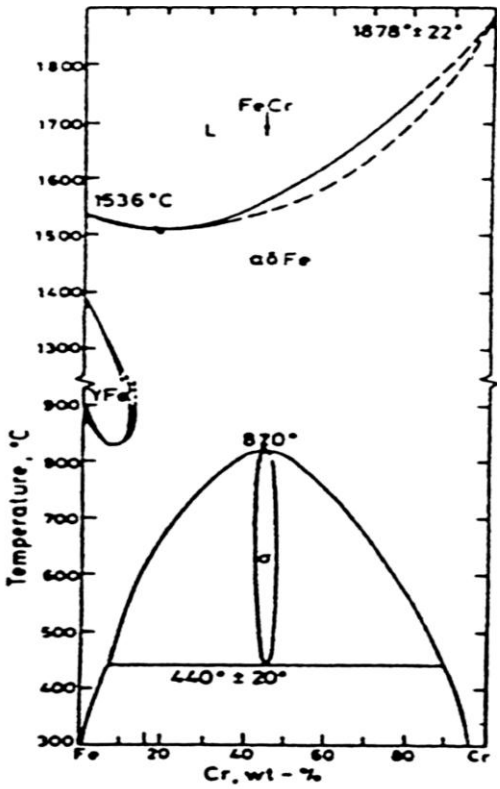

Figure 2.2(b) Fe-Cr Binary Phase Diagram (Hansen *et al., 1958).*

According to Cahn (1961) there should be no change in molar volume with composition in an infinite isotropic solid free from imperfections in order to have spinodal decomposition. So the sustainability of spinodal decomposition is very stringent for a multi component ferritic phase as in DSS, where many alloying elements other than chromium are partitioned to the ferritic phase. Chandra and Schwartz (1971) tried to calculate the solubility of chromium in iron in the temperature range of 280–500 ºC and predicted the boundaries within the miscibility gap for spinodal decomposition, nucleation and growth. Figure 2.2 shows the miscibility gap as proposed by William (1958) and the calculated chemical

spinodal by the dashed line. The coherent spinodal line in the diagram is the corrected chemical spinodal, taking into account the elastic strain energy due to 0.6% difference in the atomic size of iron and chromium. They studied the Mossbauer effect of 475 ºC embrittlement of a series of iron–chromium binary alloys by varying the chromium content and estimated the solubility of chromium in iron to be 12 wt. % at 475 ºC. They predicted that only alloys with chromium content in excess of 12 wt. % exhibit 475 ºC embrittlement. Another important observation was that alloys with chromium content 12–30 wt. % decomposed via a nucleation and growth mechanism.

Studying DSS via Mossbauer spectroscopy is always difficult as γ-austenite is paramagnetic and obscures the detection of paramagnetic α′ phase. However, Solomon and Levinson (1978) successfully studied the effects of other alloying elements on 475 ºC embrittlement with the help of Mossbauer spectroscopy and transmission electron microscopy in DSS and seven single-phase ferritic alloys. They showed that nickel promoted the formation of α′ whereas manganese, silicon and molybdenum did not influence the formation of α′. Miller and Russell (1996) also have reported similar results.

Sahu (2008) investigated a wrought grade of DSS, DINWNr. 1.4462 and observed needle-shaped precipitate after aging treatment at 475 ºC for 100 hours in the ferritic grains as shown in Figure 2.3a. He identified these precipitates as needles of α′. He also observed stacking of these needles into arrays as shown in Figure 2.3b.

Weng et al. (2004) carried out detailed investigations on the nanoscaled structure of the low-temperature aged specimens of a 2205 wrought alloy with the help of field-emission gun transmission electron microscopy. They noticed the ferritic phase giving a modulated contrast, after aging and there is a sudden change to an even contrast in austenitic phase, when observed under TEM. This mottled image with the gradient in contrast, which has the appearance of an orange-peel, is shown in Figure 2.4. The modulated microstructure coarsens with the time of aging, maintaining the similar morphology. This group has further studied the extent of phase separation that takes place due to 475 ºC embrittlement using a FEG-TEM containing an EDS. The fine scale isotropic spinodal decomposition of ferritic phase revealed chromium-rich, bright image domains and iron-rich dark image domains, i.e. α and

α′ phases, separately. It also revealed that molybdenum and manganese were partitioned to the α′ phase, while nickel was partitioning to the α phase.

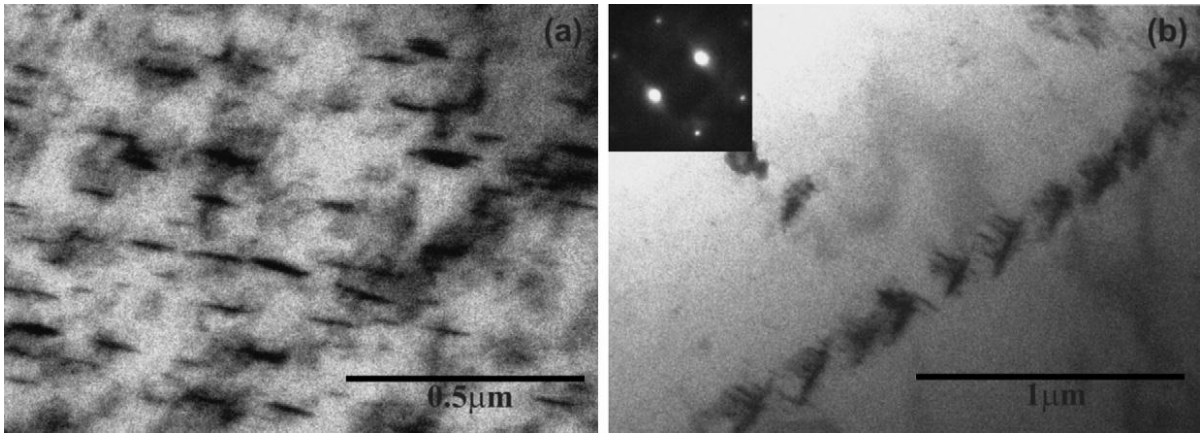

Figure 2.3 (a) Needle like precipitates observed in the ferritic phase of DSS grade DINWNr. 1.4462 After aging treatment at 475 ºC for 100 hours; (b) same grain observed in g = (011) diffraction condition (Sahu, J. K. 2008).

The three-dimensional α′ phase had been reconstructed by Miller and Bentley (1990) and they suggested that the α′ phase forms a typical complex interconnected network structure from the studies conducted by atom probe field ion microscope. Similar atom probe field ion microscopy studies on CF series of cast alloys also had been performed (Kawaguchi. et al 1997 and Bugat, S. et al. 2001), and the morphology, size distribution and chemical concentration profile of the α′ precipitates have been determined. The studies on the cast alloys revealed that the phase boundary carbides played a significant role in thermal embrittlement at temperatures greater than 400 ºC, but has insignificant effect on the embrittlement at exposure temperatures less than 400 ºC (Cortie, M. B., and Pollak, H. 1995).

Mateo et al. (1997) studied the G-phase precipitation in detail in an AISI 329 grade of DSS and observed an incubation time from the completion of spinodal decomposition to the nucleation of G-phase. After 200 hours aging treatment at 475 ºC, they observed very fine spots in TEM bright field image. The uniform G-phase particles in the grain body were observed only after 15,000 hours of aging at 475 ºC. This indicates that the possibility of G-phase precipitation in the ferritic phase requires long duration aging treatment at 475 ºC. The

carbide and nitride precipitates are mostly observed in grain boundaries (Technical Report of International Atomic Energy Agency (2003) and Johnson Jr et al. (2001).

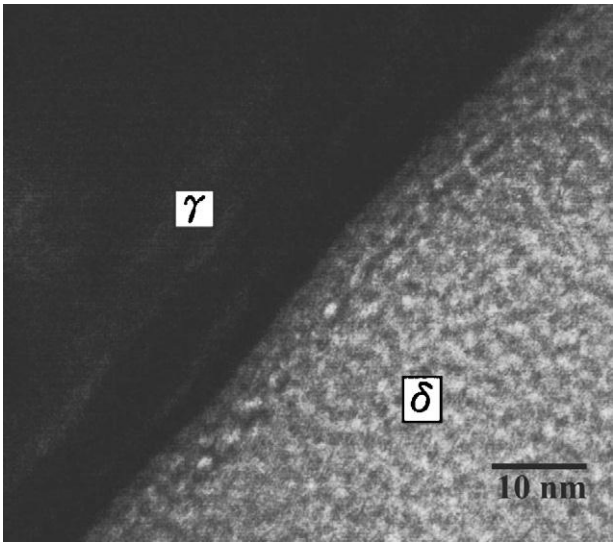

Figure 2.4 Modulated contrast observed in the ferritic phase of DSS grade 2205 aged at 475 ºC for 2 hours (Weng, K. L et al. 2004).

Recently Bliznuk et al. (2005) studied the effect of nitrogen on the short-range atomic order in the ferritic phase of duplex steel and observed that with increasing content of nitrogen in steel, its concentration in ferrite increases. They obtained that an increase in the nitrogen content from 0.17 mass % in steel SAF2205 to 0.25 mass % in steel SAF2507 led to short-range atomic ordering of chromium and molybdenum atoms, whereas a further increase of the nitrogen content (0.62 mass %) was accompanied by their clustering. The opposite behavior is obtained for the distribution of nickel atoms. However, nitrogen-caused changes in the distribution of chromium, molybdenum and nickel atoms in ferrite could not prevent the 475 ºC brittleness caused by the decomposition of the ferritic phase.

So the different possibilities for the segregation or precipitation in the ferritic phase resulting from the aging treatment at 475 ºC reported so far are:

1. Formation of α′ either through spinodal decomposition (infinitesimal composition fluctuation in a solid solution) or through the mechanism of nucleation and growth.

2. Formation of G-phase.

3. Precipitation of carbides and nitrides at grain boundaries.

The kinetics of 475 ºC embrittlement have been determined through indirect observations such as changes in certain mechanical properties like hardness (Miller, M. K., and Russell, K. F. 1996), impact energy (Sahu 2008) or saturation of certain microscopic features (Weng et al. 2004). The kinetics of precipitation plays a very important role for some of the critical engineering components, particularly in nuclear power plants. So the majority of investigations on kinetics of 475 ºC embrittlement in DSS is reported from laboratories working on the materials used in nuclear power plants (Devillers-Guerville et al. 1997), Sahu et al. (2009) and Druce, S.G. et al. (1988) These investigations are mostly reported on CF3, CF8 and CF8M cast grades of DSS.

Sahu J K (2008) observed that the deterioration of impact energy for DSS grade DINWNr. 1.4462 fit into a sigmoidal shape when plotted on a semi-log scale with time of aging at 475 ºC as shown in Figure 2.5. He obtained a value of 8J for 100, 200 and 300 hours of aging treatment and concluded that the embrittlement reaches saturation in 100 h for the investigated grade.

Miller and Russell (1996) made a comparison of the rate of decomposition of the ferrite in iron 45 wt. % chromium, 5 wt.% nickel alloys and two CF3 grades of DSS during long-term aging at 400 ºC. According to this group the addition of nickel to the binary iron–chromium alloy accelerated the kinetics of decomposition and significantly increased the hardness of the alloy as shown in Figure 2.6. Although the hardness data from the ternary alloys are similar to those of the ferritic phase in the DSS, they observed significant differences in the scale and composition amplitudes of the α and α′ phases. They investigated the extent of phase separation by determining the difference in the composition amplitudes of the α and α′ phases as a function of aging time at 400 ºC. It is evident that the kinetics of precipitation plays an important role in the deterioration of mechanical properties. As shown by Miller and Russell the composition also plays a key role in determining the kinetics of precipitation. When in one hand there is a constant effort to improve the mechanical properties by alloying DSS further with copper, nitrogen, etc., the effect of these alloying elements on α′ precipitation is a subject of extensive further research.

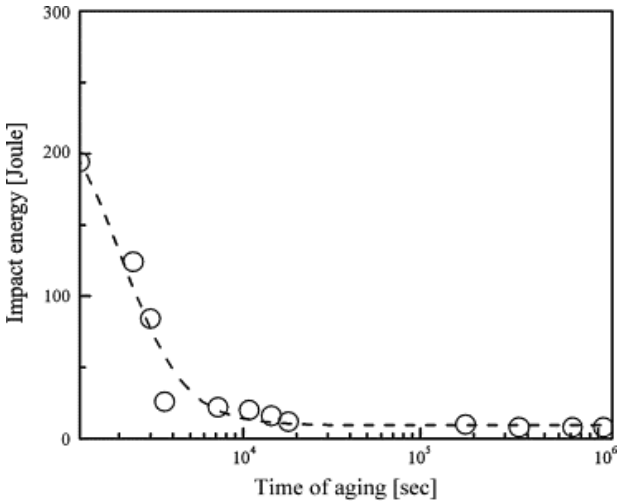

Figure 2.5 Variations of impact energy with time of aging at 475 ºC for DSS grade DIN W Nr. 1.4462 (Sahu J K (2008).

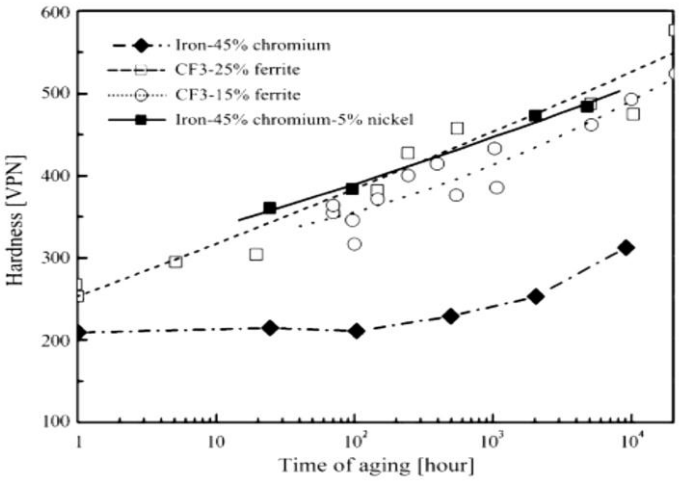

Figure 2.6 Hardness of the iron–45% chromium–5% nickel alloy as a function of aging time at 400 ^{0} C. Comparable data from the iron–45% chromium binary alloy and the ferrite phase in two CF3 stainless steels for the same temperature are included for comparison (Miller and Russell (1996).

Grobner (1973) reported that in the temperature range of 371 to 482 ºC iron–chromium alloy with 18 at.% chromium embrittled in times as short as 2 hours, whereas with 14 at.% chromium embrittlement was observed after longer exposure time. This is a clear indication of the sensitivity of this embrittlement to alloy composition. According to Grobner interstitial element accelerated the embrittlement caused by precipitation of α′ phase on dislocation

whereas substitutional alloying elements such as molybdenum and titanium did not substantially affect the kinetics of embrittlement.

The distribution of ferritic phase in the matrix, their grain size and grain shape plays a very important role in determining the degree of embrittlement. As only the ferritic phase is embrittled during aging at 475 ºC, the degradation in material properties directly depends on the amount and the morphology of the ferritic phase. It has been established that 475 ºC embrittlement is a major concern only when the volume fraction of the ferrite exceeds approximately 15 to 20% (Technical Report of International Atomic Energy Agency 2003). When the ferrite content in the microstructure is less than or equal to 15%, it remains as isolated pools contained within the austenite. In this case, the overall toughness of the alloy is not significantly affected even if the ferritic phase is embrittled. However, when ferrite levels are greater than 15% in the microstructure a continuous path of embrittled phase is formed during aging affecting the toughness of the component considerably. However, some recent evidences in the nuclear power plant components shows that ferrite levels in the range of 10 to 15% in the CF8M cast stainless steel castings may also be subjected to significant thermal embrittlement (Sahu 2008). The grain size tends to be large, and the ferrite spacing (average distance between ferrite islands) is increased in heavy-section castings. With increasing ferrite spacing at constant ferrite content, the size of the ferrite island increases and the probability of a continuous path of ferrite through the thickness of the cast component increases. Bonnet et al. (1990) selectively dissolved the austenite phase from samples of CF8M and found that the ferrite phase remains continuous at ferrite volume fractions as low as 5%.

Fei et al. (2009) conducted accelerated thermal ageing experiments on a cast DSS at 400 ^{0} C for up to 3000 hours in order to replicate 20 years of ageing at service temperatures (288-327 ^{0} C) in Light Water Reactors according to the Arrhenius equation:

$$k = A \exp(-E_a RT)$$

where k is the rate coefficient, A is the pre-exponential factor, E_a is the Arrhenius activation energy, R is the universal gas constant and T is the absolute temperature.

Chandra et al. (2010) aged a duplex stainless steel at 400 ^{0} C for 5000 hours and found that the yield strength and ultimate tensile strength increased, and the ductility decreased due to the embrittlement caused by the precipitation of α′ in the ferrite phase.

2.4.1.1 Effect of 475 ^{0} C embrittlement on mechanical properties

It is established that aging, in the temperature range of 280-500 ^{0} C, results in a significant deterioration of mechanical properties. The embrittlement affects tensile, fracture and fatigue behavior. In this section the effect of 475 ^{0} C embrittlement on tensile, fracture and fatigue behavior is reviewed in separate sections.

2.4.1.1.1 Tensile behavior

Before discussing the results obtained on the effect on 475 ^{0} C embrittlement on tensile behavior of DSS, it is important to note that the structural incompatibility between the ferritic and austenitic phase modify the tensile behavior (Johansson et al. 2000) .When it comes to tensile strength ferrite is usually stronger than austenite for the same interstitial content. However, the solubility of carbon or nitrogen in austenite is much higher compared to ferrite (Gunn R. 1997). In DSS nitrogen gets preferentially partitioned in a way that austenite becomes stronger than ferrite (Ager et al. 2000). It was reported that in super DSS grades the amount of nitrogen dissolved in austenite is as high as 0.45 wt. % when the average nitrogen content is 0.27 wt. % and despite the higher strength due to preferential nitrogen partitioning more plastic deformation occurred in austenite compared to ferrite as compressive residual stress build up in the ferritic phase during cooling. Strength is also grain size dependent. The grain size in a DSS is usually smaller than that of ferritic and austenitic stainless steel of corresponding chemical composition. This is explained by mutual hindering of growth of the ferrite and austenite grains. If the effect of grain size and partitioning of interstitial is compensated, then the strength of DSS is controlled by the stronger ferritic phase. Toughness of DSS is very high due to the presence of austenite in the matrix. Austenite retards the cleavage fracture of ferrite. However, toughness is reported to be very sensitive to the precipitation of secondary phases.

Zielinski et al. (2003) studied the evolution of dislocation structure in a solution annealed DSS by in situ TEM straining experiment and reported that the evolution of dislocation

structure during straining was dependent on the orientation relationship between the two phases. In the case of special orientation relationships, the slip markings in the ferrite, produced by the dislocations emitted from the boundary, indicate the compatibility of easy slip systems in the two phases, which favors a strong localization of strain. In the case of random orientation relationships, the incompatibility of the easy slip systems in austenite and ferrite results in the cross slip of the dislocations emitted from the boundary into the ferrite grains leading to multiplication and the formation of dislocation loops and debris. They attributed the high flow stress of DSS to the particular slip transfer mechanism related to the random orientation relationships between the austenite and ferrite. Bugat et al. (2001) performed in situ tensile test on DSS aged at 400 ^{0} C for 700h to characterize strain fields and monitor the sites of damage nucleation. According to them damage preferentially initiates in areas, where the common slip system of the bi-crystal has a low Schmid factor.

Hilders et al. (1999) studied the effect of 475 ^{0} C embrittlement on fractal behavior and tensile properties of DSS and observed dimple type of the fracture mode for small aging times and transgranular as well as dimple rupture for 24, 40, and 120 hours of aging. They also observed a decrease in fractal dimension and the true fracture strain with an increase in time of aging.

Girones et al. (1999) studied the dynamic strain aging effects on super DSS at temperatures ranging from 275 to 475 ^{0} C. They reported that the activation energy for serrated flow, which is used as a parameter to identify the mechanism of dynamic strain aging, is too high for interstitial solutes and too low for substitutional ones to migrate to mobile dislocations to pin them through bulk diffusion both in austenite and ferrite.

2.4.1.1.2 Fracture behavior

The most significant effect of the 475 ^{0} C embrittlement is the sudden drop in impact toughness. Sahu J K (2008) observed that the impact energy of DSS grade DINWNr. 1.4462 drops from 260J in the annealed condition to 8J after aging treatment at 475 ^{0} C for 100 hours. He attributed the drop in impact energy value to the inability of the ferritic phase to form deformation twins in the aged condition through TEM examination.

Devillers-Guerville et al. [24] showed that the micromechanism of impact fracture at room temperature of a cast grade of DSS containing about 20 wt.% ferrite, embrittled at 400 ^{0} C are:

(i) Nucleation of cleavage cracks grouped in millimetric clusters in the ferritic phase;

(ii) Growth of the cavities by the plastic deformation of austenitic phase; and

(iii) Coalescence of the cavities to form a macroscopic crack.

They observed no strain rate effect on the embrittled material when tested at room temperature. Druce et al. (1988) studied the effect of notch depth, notch acuity and side grooving on the impact fracture behavior of a cast DSS containing 25 wt. % ferrite in the temperature range of −200 to +300 ^{0} C. They reported that increasing specimen constraint is found to have a marked influence on fracture mode, the temperature for the onset of low to high fracture energy transition, and the fracture energy per unit ligament area associated with fracture at elevated temperature. On the basis of these test data they came out with optimum specimen geometry for monitoring the effect of 475 ^{0} C embrittlement on toughness and determining embrittlement kinetics.

The embrittlement at 475 ^{0} C causes severe impairment of the fracture toughness of DSS (Vogt et al. (2002), Jaye gendrot et al. (2000), Miller et al. (1978) and Brown et al. (1991). For the wrought grades like 2205, which are used in areas, where fracture based design is not extensively used, work reported on the fracture evaluation of these grades of DSS is very scarce. However, cast DSS grades like CF3, CF8, CF8M, used in many parts in the reactor vessel internal (RVI) such as in the lower support casting or forging, flow-mixing device and in the primary piping section such as in the combustion engineering surge nozzle at the hot leg, in combustion engineering safety injection nozzle and the elbows of PWR in nuclear power plants, are designed based on fracture mechanics approach. The lowering of fracture toughness as a result of 475 ^{0} C embrittlement is a matter of grave concern for these grades of DSS. The operating temperature of a PWR typically falls between 280 and 300 ^{0} C and at this temperature aging takes place after prolong exposure. For this reason the fracture toughness of an embrittled material has never been a matter of concern for the design

engineers at the time of initial installation of the component. However, after exposure for long years the embrittlement results in a drop of fracture toughness and estimation of residual fracture toughness of a service-exposed material has been a major concern for engineers. The fracture toughness for these components is either estimated by using some empirical relation or by some alternative experimental technique as normal laboratory techniques are extremely difficult for the service-exposed components.

Tujikura and Urata (1999) evaluated the integrity of the primary coolant piping for an initial PWR plant in Japan by means of elastic plastic fracture mechanics (EPFM) analysis. They applied EPFM mathematics to evaluate fracture toughness, as fracture in DSS after thermal embrittlement is recognized to be ductile (Technical Report of International Atomic Energy Agency (2003). So it was appropriate to apply this concept for the evaluation of the stability of the assumed crack. For this study they had chosen the location to be the hot leg piping at the reactor vessel outlet nozzle since both the temperature and imposed load are more severe and ferrite content was relatively high in the evaluating plant. The evaluation results showed that the crack will not grow into an unstable fracture and the integrity of the piping will be secure, even when such through-wall crack length is assumed to be as large as the fatigue crack length grown for a service period of up to 60 years.

Jayet-Gendrot et al. (1998) attempted fracture toughness assessment with mini-CT specimens taken from the skin of primary circuit elbows. They carried out the tests for six different parts (Ref. Table 2.1) of primary circuit elbows and compared the results obtained from a 0.4T-CT specimen to 1T-CT specimen. It can be seen from Figure 2.7 that for all the materials, the (J, Δa) points obtained using mini-CT specimens are in good accordance with the points obtained using 1T-CT specimen. Scatter for both the geometries are of the same order. They also compared the results with the fracture toughness values obtained from predictive formulae. After the validation, they showed that such mini-CT specimens were representative and have proposed guidelines for further practice.

Le Delliou et al. (1999) had conducted bending tests in an elbow of the main primary circuit of a pressurized water reactor, which contained a semi-elliptical circumferential notch

as well as casting defects located on the flanks and had shown that the notch did not initiate even at the maximum applied bending moment.

Mathew et al. (1999) used automated ball indentation method to evaluate the degradation in mechanical and fracture properties as a result of low-temperature aging. They carried out tests after aging at 400 ^{0} C for 6, 12, 18 months and have reported that there was a progressive decrease in indentation energy to fracture.

Earlier estimation of residual fracture toughness was made using predictive formulae based on chemical composition and aging conditions. Chopra and Chung (1985) had made a conservative estimation of fracture toughness and J‑R curve of DSS after thermal aging from the estimated room temperature Charpy V-notch impact energy. This curve defined the resistance of thermally aged cast stainless steel material to ductile, stable crack growth. The J‑R curve was expressed by the power law relation in Eq. (1).

$$J = C A_a n \text{ ……..(1)}$$

Where, J was determined according to ASTM Specifications E 813-85 and E 1152, A_a was the crack extension, C and n were constants. Correlations were developed between these constants and the estimated Charpy V-notch impact energy to determine the lower bound J‑R curve at PWR operating temperatures. These correlations accounted for differences between statically and centrifugally cast materials. The degree of conservatism in this J‑R curve is low if both the estimated room temperature and operating temperature Charpy V-notch impact energies are on the upper shelf (greater than about 80 J/cm^2), but the degree of conservatism is higher if the room temperature impact energy is on the lower shelf. These correlations and the calculated values of CV_{sat} can be used to estimate lower bound fracture toughness after long-term thermal ageing.

Table 2.2 The parts of primary circuit elbows and heat treatment conditions for fracture toughness study (Jayet-Gendrot et al. (1998)).

Products	Mark	Thermal aging treatment
90^0 Elbow	EL	3000 hours at 400 ^{0} C
Plate	CC	1000 hours at 400 ^{0} C
Plate	DI	10,000 hours at 400 ^{0} C
50^0 Elbow	EK	30,000 hours at 350 ^{0} C
Plate 50^0	DI	700 hours at 400 ^{0} C
Elbow	EK	30,000 hours at 325 ^{0} C

Example estimates of the lower bound fracture toughness of Grade CF8 and Grade CF8M cast stainless steel that are within ASTM Specification A 351 and have a ferrite content greater than 15% are listed in Table 3. The corresponding values of CV_{sat}, the constants C and n for the J-R curves at 290 ^{0} C, and the lower bound fracture toughness, J_{Ic} (J at crack extension of 0.2 mm), for both statically and centrifugally cast materials are also listed in Table 2.2 (Technical Report of International Atomic Energy Agency. (2003). The lower bound fracture toughness of Grade CF8M is lower than that of Grade CF8. In addition, the lower bound fracture toughness of a statically cast material is lower than that of centrifugally cast material. These lower bound toughness values are for steels with ferrite content greater than 15%, which is higher than the typical average ferrite content in the nuclear industries.

In spite of the fact that safe values of residual fracture toughness can be predicted through empirical formulae based on chemical composition and aging conditions, efforts have been put to experimentally determine the fracture toughness values of the service-exposed material. Though standard fracture toughness tests are not possible due to severe operating conditions in the areas of PWR, non-standard tests are proposed to determine the fracture toughness values.

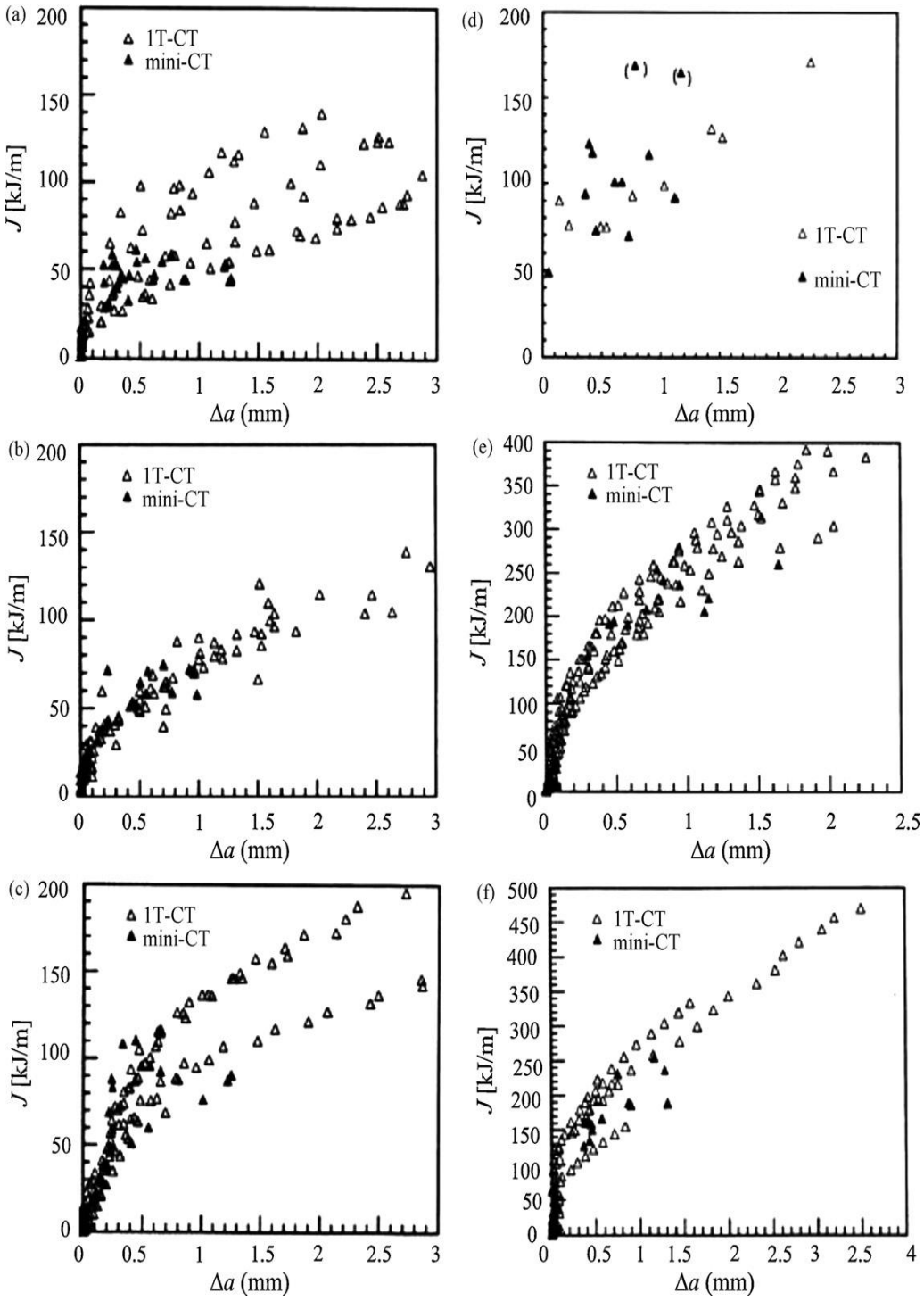

Figure 2.7 J-Δa results at 320 ^{0} C for material: (a) EL aged 3000 h at 400 ^{0} C; (b) CC aged 1000 h at 400 ^{0} C; (c) DI aged 10,000 h at 400 ^{0} C; (d) EK aged 30,000 h at 350 ^{0} C (the crack deviated from side groove plane and the result was not taken into account); (e) DI aged 700 h at 400 ^{0} C; (f) EK aged 30,000 h at 325 ^{0} C (Jayet-Gendrot et al. (1998).

Table 2.3 Estimates of service temperature (290 ^{0} C) lower bound fracture toughness of cast grade DSS CF8 and CF8M, both statically cast and centrifugally cast with ferrite volume fraction greater than 15% (Technical Report of International Atomic Energy Agency. (2003).

Cast grade DSS	Saturation room temperature impact energy CV_{sat} (J/cm^2)	Statically cast DSS			Centrifugally cast DSS		
		C	n	J_{Ic} (kJ/cm^2)	C	N	J_{Ic} (kJ/cm^2)
CF8	25	251	0.32	150	330	0.32	197
CF8M	20	167	0.30	103	195	0.30	120

2.4.1.1.3 Fatigue behavior

The factors those are known to influence the fatigue behavior of DSS are:

1. Alloy composition.

2. Volume fraction of ferrite.

3. Processing route (cast and wrought).

4. Texture.

Some of the above-mentioned factors also are known to have pronounced effect on the change in cyclic stress‑strain behavior and fatigue life of DSS due to aging treatment at 475 ^{0} C. So a discussion on the change in fatigue behavior of DSS due to aging treatment at 475 ^{0} C must be done in conjunction with the above-mentioned factors. For example, Llanes et al. (1996) observed ferrite like deformation mechanism and fatigue softening at $\Delta \varepsilon_{pl}/2=1.2\times10^{-3}$ for the AISI 329 grade of DSS in the aged condition (0.074 wt. % nitrogen, 38%γ and 62%α, wrought), while Vogt et al. (2002) for their alloy B_oA920 grade of DSS (0.4 wt.% nitrogen, 70%γ30%α,wrought) observed no change in fatigue resistance even at $\Delta \varepsilon_{pl}/2 = 5.3\times10^{-3}$ after aging treatment at 475 ^{0} C. This difference may be attributed to several factors such as nitrogen content, ferrite volume fraction.

DSS is undergoing continuous evolution to newer grades primarily based on adjusting the chemical composition. The most important is the increase in nitrogen content. Nitrogen affects the cyclic stress‑strain behavior and fatigue life of DSS (Akdut (1999), Alvarez et al. (2007) and Takemoto et al. (1986). It is austenite stabilizer and strengthens austenite by solid solution strengthening mechanism. A stronger austenitic phase results in strain partitioning to the ferritic phase. And the response of the ferritic phase to this strain partitioning will be different in plane annealed and aged conditions. Moreover, recently nitrogen is also found to have establishing short-range order of chromium in δ- ferrite (Mateo et al. (1997).

Nitrogen addition is thought to be beneficial for the fatigue life of the material. However, Akdut (Akdut 1999) observed that contrary to single-phase austenitic stainless steels only increasing the nitrogen content in DSS did not increase fatigue life, but nitrogen in combination with the morphological scale and anisotropy apparently altered the cyclic stress strain curve. This means the beneficial effect of nitrogen on fatigue behavior can be realized only with certain morphology. The conventional concept of microstructural barrier in single-phase materials sometime does not explain the low cycle fatigue behavior adequately. Stolarz and Foct (2001) described that the physical properties and the degree of plastic deformation in the neighbouring grain or particle determine the resistance of a barrier. Girones et al. (2004) studied the influence of texture on the surface damage mechanisms developed in cyclically loaded aged DSS. The rolling or recrystallization texture is known to determine the local crystallographic orientation and this in turn influences the evolution and growth of surface damage (Duber 2007) and Alvarez-Armas (2006). Alvarez-Armas et al. (2007) observed that the most important feature of the dislocation structure developed just beneath the surface of the fatigued specimen corresponds to the intense shear bands oriented in the direction of the shear plane crossing grains and phases when the K‑S relationship is satisfied. This observation further strengthens the studies made by Girones et al. (2004) on the indirect influence of texture on fatigue damage.

Sahu, J. K. (2008) conducted total strain controlled fatigue test at $\Delta\varepsilon/2$ values 4.0×10^{-3}, 6.0×10^{-3}, 8.0×10^{-3} and 1.0×10^{-2} for DSS grade DIN W Nr. 1.4462 in annealed and embrittled (aged at 475 ºC for 100 hours) condition and observed that the deformation curves in the annealed condition have three discernible stages: (i) cyclic hardening, (ii) cyclic softening,

and (iii) cyclic saturation. In the aged condition he observed two discernible stages: (i) cyclic hardening and (ii) cyclic softening till final failure for all values of strain amplitudes. The life span of each of the above stages was observed to be a function of strain amplitude both in annealed and aged condition, e.g. (i) he observed a prolonged cyclic saturation at $\Delta\varepsilon/2 = 4.0\times10^{-3}$ and the period of cyclic saturation decreased with increase in strain amplitude in the annealed condition, (ii) cyclic softening was gradual at $\Delta\varepsilon/2 = 4.0\times10^{-3}$, 6.0×10^{-3} and 8.0×10^{-3}, whereas rapid softening was observed for $\Delta\varepsilon/2=1.0\times10^{-3}$, and (iii) cyclic softening was rapid with increase in the value of strain amplitude in the aged condition as shown in the Figure 2.8.

Alvarez-Armas et al. (2006) conducted total strain controlled fatigue testing ($\Delta\varepsilon/2 = 3.5\times10^{-3}$, 4.0×10^{-3}, 5.0×10^{-3}, 8.5×10^{-3}, 9.5×10^{-3}) of SAF 2507 grade of super DSS containing 0.236 wt. % nitrogen. They categorized the cyclic hardening softening response observed by them into three well-defined plastic strain ranges shown in Figure 2-17a. Plastic strain ranges between 7.5×10^{-4} and 2.5×10^{-3} are identified by a long softening followed by a long saturation stage, while between 4.0×10^{-3} and 6.0×10^{-3}, a small initial cyclic hardening followed by a continuous softening stage characterized these strains. Lastly, between 8.5×10^{-3} and 1.25×10^{-2}, an important initial cyclic hardening followed by a pronounced softening stage, which turned into a nearly saturation stage near the end of the fatigue life.

Llanes et al. (1996) studied the hardening softening response of an AISI 329 grade of DSS in the annealed ($\Delta\varepsilon/2$ values 2.0×10^{-3}, 3.0×10^{-3}, 4.0×10^{-3}) and two aged conditions mentioned in. One set of specimen was aged at 475 ºC for 25 hours ($\Delta\varepsilon/2$ values 3.0×10^{-3}, 6.0×10^{-3}) and another set of specimen were aged 475 ºC for 200 hours ($\Delta\varepsilon/2$ values 4.5×10^{-3}, 6.0×10^{-3}). They observed hardening in the first few cycles as shown in Figure 2-17b. At low and intermediate $\Delta\varepsilon_{pl}/2$, such hardening was followed by either slight and rapid (low $\Delta\varepsilon_{pl}/2$) or gradual (intermediate $\Delta\varepsilon_{pl}/2$) softening. At both $\Delta\varepsilon_{pl}/2$ values a steady state of saturation was finally attained. At large $\Delta\varepsilon_{pl}/2$ annealed and aged specimens experienced a continuous softening, after hardening, till fracture. This softening behavior was much more pronounced in the aged materials than in the annealed steel. For the largest amplitudes applied, the first few cycles of each step were characterized by load drops accompanied by audible noises characteristic of twinning. Similar hardening–softening responses were found in aged

materials at large values of $\Delta\varepsilon_{pl}/2$ in spinodally decomposed high chromium ferritic stainless steels subjected to LCF (Park et al. 1985).

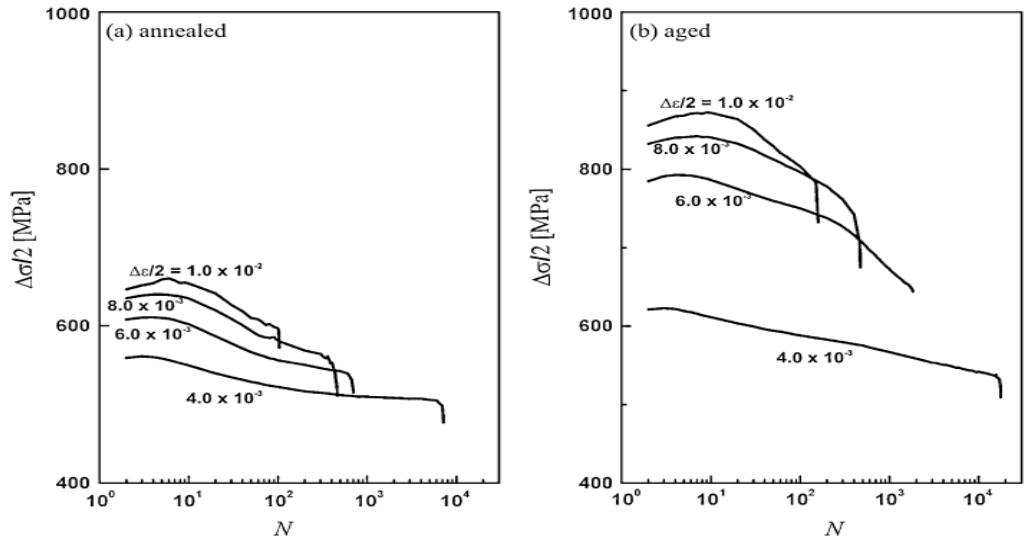

Figure 2.8 Cyclic hardening/softening curves for DSS grade DINWNr. 1.4462 (a) annealed (b) aged (475 ºC for 100 hours) condition (Sahu, J. K. 2008).

Vogt et al. (2002) conducted strain controlled fatigue testing of two grades of DSS designated UR52N+ and BoA920 having nitrogen content 0.24 and 0.4 wt.%, respectively, with $\Delta\varepsilon/2$ values of 4.0×10^{-3} and 1.0×10^{-2} in the annealed and aged conditions (aged at 475 ºC for 200 hours). The deformation curves for both alloys are shown in Figure 2.9 c and d. The aging treatment at 475 ºC treatment did not affect the fatigue resistance, which even improved at low strain amplitude for these alloys. The aging treatment resulted in a strong increase of the stress levels for both alloys at low and high strain amplitudes. At $\Delta\varepsilon/2 = 4.0\times10^{-3}$ the curves shifted to 100MPa higher (UR52N+) and 70MPa higher (B_oA920) but their qualitative aspect remained similar to that usually reported for as quenched DSS (slight hardening followed by a softening and a stabilization of the stress amplitude). However, the fatigue behavior of the aged materials significantly differed from that of the annealed ones for the tests conducted at $\Delta\varepsilon/2=1.0\times10-2$, i.e. where the plastic strain was high. In the case of the aged UR52N+ steel, the initial hardening was very pronounced. This hardening period was accompanied by a typical noise caused by twinning. On the contrary, the B_oA920 steel did not exhibit such a pronounced hardening and the cyclic deformation occurred without any characteristic twinning noise. However, this material exhibits a stronger softening at high

strain amplitude (δ_s = 0.199 in the aged condition instead of 0.148 in the annealed condition) during about N= $0.7N_f$ of the fatigue life.

Mateo et al. (2001) conducted experiments in an extended range of plastic strain amplitude ($2.9\times10^{-5} < \Delta\varepsilon_{pl}/2 < 6.6\times10^{-3}$) and the Coffin- Manson curve in their case is subdivided into three regimes: stage I $\Delta\varepsilon_{pl}/2 < 1.0\times10^{-4}$ with austenite like behavior; stage II, $< 1.0\times10^{-4} < \Delta\varepsilon_{pl}/2 < 6.0\times10^{-4}$ with mixed austenite–ferrite like response; stage III, $\Delta\varepsilon_{pl}/2 > 6.0\times10^{-4}$ with pure ferrite like behavior. But the above works were reported for DSS grades containing 0.07wt.% nitrogen. And the multiple factors that can affect the fatigue life can be realized from the studies conducted by Akdut N (1999). He studied the phase morphology and fatigue life of nitrogen alloyed duplex stainless steels and observed the fatigue lives of DSS were influenced by numerous parameters such as processing history and chemical composition and, thus by morphological anisotropy, morphological scale and nitrogen content. He showed that change in increasing morphological anisotropy and decreasing morphological scale has an increasing effect on the fatigue life of DSS. Contrary to single-phase austenitic stainless steel, increasing the nitrogen content in DSS did not appear to increase the fatigue life. However, nitrogen in combination with the morphological scale and anisotropy apparently alters the extent of each of the three regime proposed by Mateo et al. (2001). Akdut N (1999) also postulated the dependence of fatigue life on crystallographic texture.

Nystrom and Karlsson (1996) suggested that a careful balance of the ferrite content in a duplex microstructure can eliminate the effect of embrittlement to a certain extent, retaining the advantage of duplex microstructure. They showed that with an alloy containing 25% ferrite and 75% austenite, the high cycle fatigue properties are little affected by aging at 475 ºC for 100 hours. The nominal fatigue crack growth rates, da/dN, as a function of the stress intensity range, ΔK, are shown in Figure 2.10. As can be seen, the annealing at 475 ºC of the duplex material has only a minor influence on the crack growth properties with a slight shift to the left of crack growth curve for the embrittled condition. This means that the crack growth resistance is essentially insensitive to the hardening caused by the heat treatment.

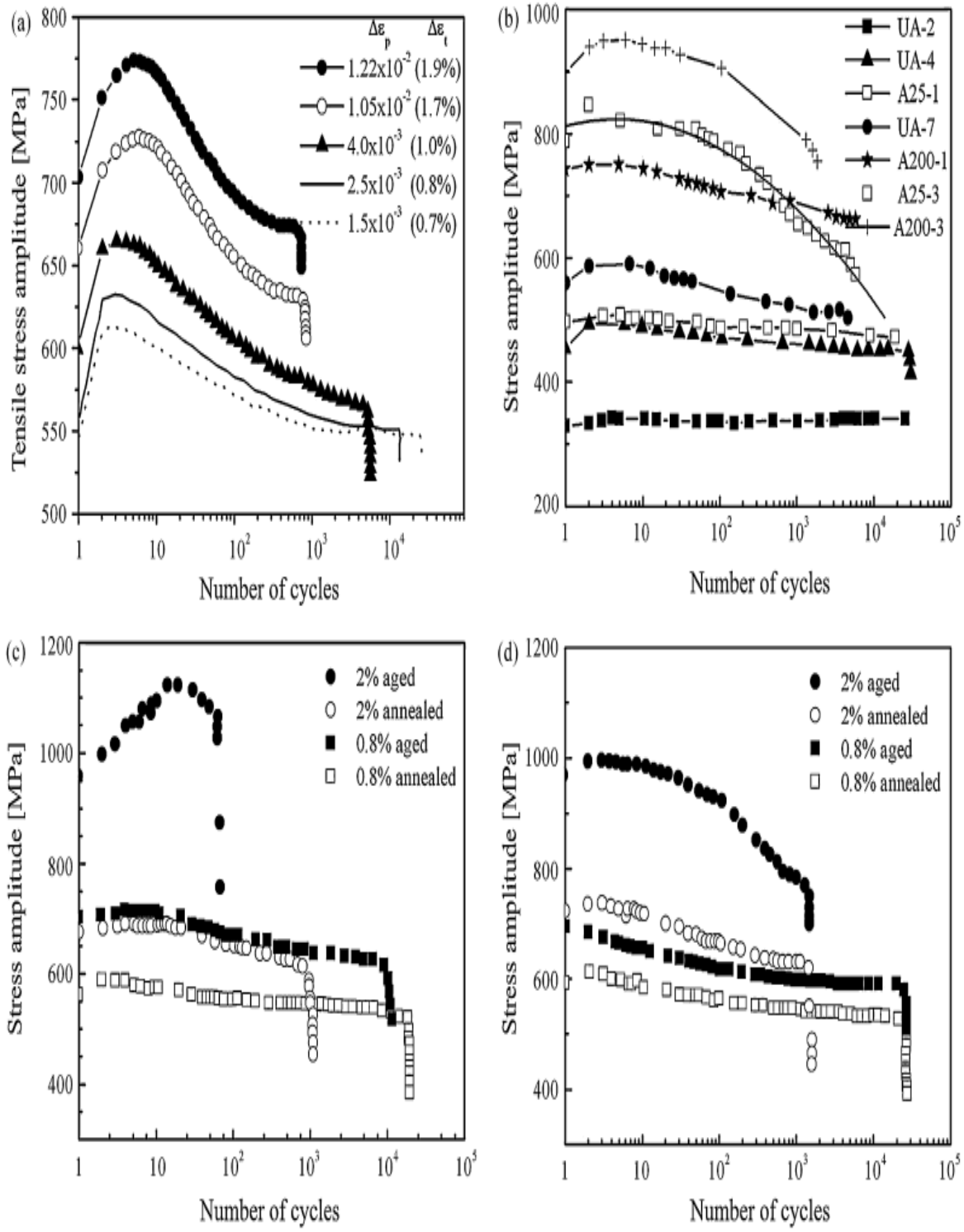

Figure 2.9 Cyclic hardening/softening curves for DSS grades (a) SAF 2507 at different plastic strain ranges ; (b) (f) AISI 329 unaged (UA) and aged (A25, A200) condition; (c) UR52N+ in the annealed and aged condition; (d) B_oA920 in the annealed and aged condition (Vogt et al. 2002).

Llanes et al. (1997) in their work on high cycle fatigue behavior of aged DSS showed that the large increase in the overall monotonic strength is not completely reflected in its fatigue strength. They tested one set of samples in the unaged condition (UA) and another after aging treatment at 475 ºC for 200 hours (A200) S–N plot is shown in Figure 2.11. They observed that the high cycle fatigue strength is strongly affected by the crack nucleation stage in the softer phase The fatigue strength improvement results from the higher cyclic yield stress of the spinodally hardened ferrite which induces an increasing difficulty for early propagation of microcracks nucleated within austenite into and through the ferritic matrix.

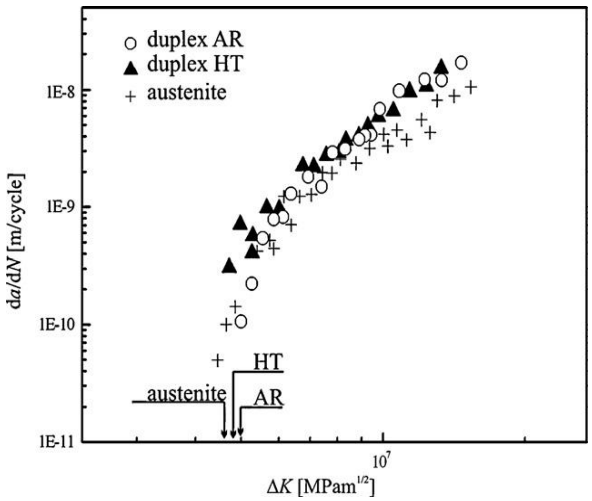

Figure 2.10 da/dN–ΔK relationship for DSS and austenitic grade stainless steel (Nystrom and Karlsson 1996).

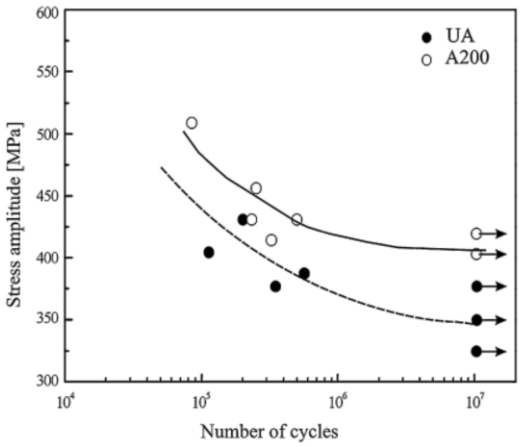

Figure 2.11 HCF behavior for unaged (UA) and aged (A200) DSS grade AISI 329 (Llanes et al. 1997).

2.4.1.1.4 Fatigue crack initiation in DSS embrittled at 475 ^{0} C

Evolution of surface roughness, subsequent nucleation and growth of short crack in DSS by cyclic loading is strongly influenced by the microstructural parameters, i.e. grain size, grain orientation, grain and phase boundary geometry or the new phase called grain boundary character distribution and precipitates. The crack initiation and growthin particular grain in DSS depend on the orientation, inherent strength and toughness properties of neighbouring grains and it is very important to know and understand how these factors determines fatigue damage evolution. Taisne et al. (2006) in a recent study on the role of interfaces in fatigue deformation mechanism in DSS bicrystal observed that interphase interface geometry and elasticity affects the dislocation transmission process. Duber (2007) in a recent investigation on the same grade of DSS showed that crack propagation in the short crack regime can be subdivided into two basic mechanisms: operating either by single-slip (crystallographic propagation) and double-slip (propagation perpendicular to loading axis), giving rise to substantially different propagation rates. Additionally, it was found that a crack, which has grown in double-slip, can change to the single-slip mechanism again, when entering a new grain and no adequate second slip plane is available. They also determined that the $\alpha\gamma$ phase boundary offers more resistance to slip transfer as compared to $\alpha\alpha$ and $\gamma\gamma$ grain boundaries. Alvarez-Armas et al. (2007) observed that the efficiency of the coupling between phases seems to play an important role in the crack formation process. Stolarz and Foct (2001) on their study on specific features of two phase alloys response to cyclic deformation observed that the short crack initiation sites (brittle or ductile phase, interfaces), the cyclic damage mode (single or multiple cracking) and consequently the fatigue life, depend both on morphological and topological parameters of the microstructure and on the difference on the mechanical properties of constitutive phases. These studies justify the increasing interest in the study of the influence of microstructural parameters on the evolution of surface fatigue damage and the subsequent crack nucleation.

In DSS aged at 475 ^{0} C, the difference between the mechanical properties of austenite and ferrite become more pronounced. In the case of cyclic loading of DSS in annealed condition, slip bands represent the main crack initiation site either in austenite or ferrite depending on the applied strain amplitude. However, the slip incompatibilities created at the

interphase boundaries after the aging treatment at 475 ^{0} C may lead to a non-uniform distribution of surface damage. In a recent investigation, in situ tensile tests have been performed on a thermally aged DSS and EBSD technique has been used to correlate local phase morphology with crystallographic properties (Girones et al. (2004). Sahu (2008) conducted completely reversed (R = −1) interrupted stress-controlled fatigue test at $\Delta\sigma/2$ = 400 and 500MPa to identify the crack initiation sites and relate these to the crystallographic parameters obtained from EBSD-OIM scans and observed that the crack initiation sites are the slip markings corresponding to {111} plane traces in the austenitic grains at $\Delta\sigma/2$ = 400MPa and Σ3 CSL boundary in the austenitic grain at $\Delta\sigma/2$ = 500MPa as shown in Figure 2.12

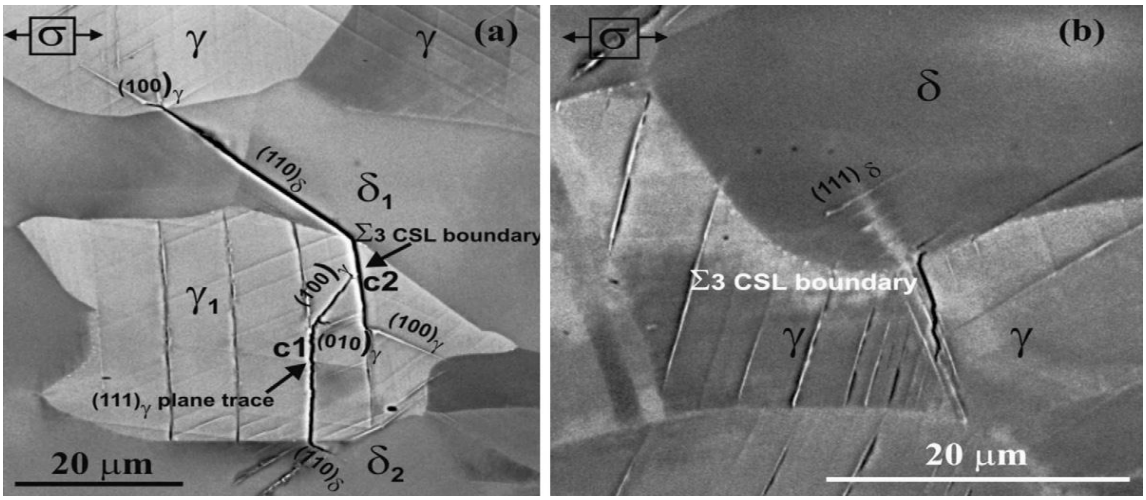

Figure 2.12 Fatigue crack initiation in a DSS grade DIN W Nr. 1.4462 aged at 475 ^{0} C for 100 hours. (a) The growth of crack c2 observed after N= 27,000 cycles at $\Delta\sigma$ /2 = 400MPa; (b) crack initiation at Σ3 CSL boundary at $\Delta\sigma$ /2=500MPa (Sahu 2008).

2.4.3 Reversion treatment

Chung and Chopra (1987) obtained a DSS from a boiling-water reactor pump after ~12 years of nominal service and annealed it at 550 ^{0} C for 1 hour. They found a large increase in Charpy impact energy after annealing. They also found that the mottled image of α′ precipitates in the as-aged condition was replaced by a clear image of high density of dislocations indicating an easy dislocation movement during the impact test due to the dissolution of α′ during the annealing treatment.

The recovery of a long-term ageing embrittled duplex stainless steel by annealing was investigated by Li et al. (2013). The DSS was aged at 400 ^{0} C for up to 20,000 hours and then annealed at 550 ^{0} C for 1 hour. On analysing the microstructure, they found that the spinodal decomposition precipitates (α′) had dissolved into ferrite. The annealing process caused the elimination of these precipitates which lead to the recovery of mechanical properties to the level of the un-aged material.

Jang et al. (2014) studied the effects of reversion heat treatment on the recovery of thermal ageing embrittlement of cast DSS. The material was aged for 1000 hours at 400 ^{0} C and then reversion heat treated at 550 ^{0} C for 30 minutes. The microhardness of the ferrite phase decreased significantly while that of the austenite phase was unaffected. However, the microhardness did not reduce to the level of the un-aged condition. Microstructural analysis revealed that the mottled contrast in the image of the aged specimen mostly disappeared in the ferrite phase after the reversion heat treatment, indicating that the Cr-rich α′ precipitates had dissolved. But they also found unidentified Mo-rich particles had formed during the reversion treatment. They attributed the incomplete recovery of microhardness to the precipitation of this Mo-rich phase which may have been one of the Mo-rich phases known to form in the ferrite phase in the temperature range of 550-700 ^{0} C, like Sigma, Chi, Tau or R-phase. Hwang et al. (2014) aged a superduplex alloy at 600 ^{0} C for various time periods from 1 minute to 300 hours and observed that the volume fraction of R-phase was maximum (~6%) after around 30 hours of ageing beyond which it decreased due to transformation into ζ-phase. They found that even an R-phase volume fraction of 3%, which was achieved after almost 2 hours of ageing, was sufficient to cause significant embrittlement.

Scope of the present work

Studies on single phase ferritic stainless steels have shown that the microstructural changes associated with "475ºC embrittlement" can be reverted by a short reversion treatment at temperatures within the range of 500ºC-600ºC. DSS have two major deviations from the conventional iron-chromium alloys:

1. It has both ferrite and austenite in the microstructure and the ferrite content vary from 9 to15 wt.% for cast DSS to 30 to 50 wt.% in wrought DSS.

2. The ferrite in DSS contains additional alloying elements such as chromium, nickel, molybdenum, copper and nitrogen

However, there are no much conclusive evidences on how the microstructural changes evolve during reversion heat treatment and translate on the mechanical properties of DSS and vice-versa. In addition, it is not clear how fast that the recovered DSS after the reversion heat treatment could be re-embrittled, when it is subjected to the service temperature of nuclear power plants. Therefore, understanding the re-aging behaviors of the recovered DSS is also important to determine the applicability of the reversion heat treatment. In this regard the current investigation was aimed to study and correlate the microstructural changes occurring during the reversion heat treatment with the mechanical properties.

Chapter 3 Experimental work

This chapter describes the experimental techniques used in the present investigation.

3.1 Material

The material used for this investigation is commercially pure DSS, S2205. The chemical composition of the material was determined by Optical Emission Spectrometry and is given in table 3.1. The material was supplied in the form of a rod of 25 mm diameter.

Table 3.1 Chemical composition (wt. %) of the investigated steel.

C	Si	Mn	P	S	Cr	Mo	Ni	N	Fe
0.020	0.53	1.415	0.033	0.02	21.91	2.504	4.751	0.1871	68.65

3.2 Heat treatment

As received samples were subjected to solutionising heat treatment in which the samples were heated in a muffle furnace at 1060 ºC for 60 minutes and then water quenched. Annealed samples were then subjected to thermal ageing before the application of the reversion heat treatment (RHT). The TTT diagram for the start of 475 ºC embrittlement obtained from the supplier of the material is shown in Figure 3.1. The specimen was then heated to 475 ºC and was kept at this temperature for different intervals from 25 hours, 50 hours, 100 hours, 250 hours, 500 hours and 1000 hours followed by water quenching. Then to study the recovery behavior of thermally embrittled DSS, the samples were subjected to reversion heat treatment (RHT), in which samples were heated at 550 ºC for 30, 45, 60, 75, 90 and 120 minutes. Figure 3.2 depicts the heat treatment cycle.

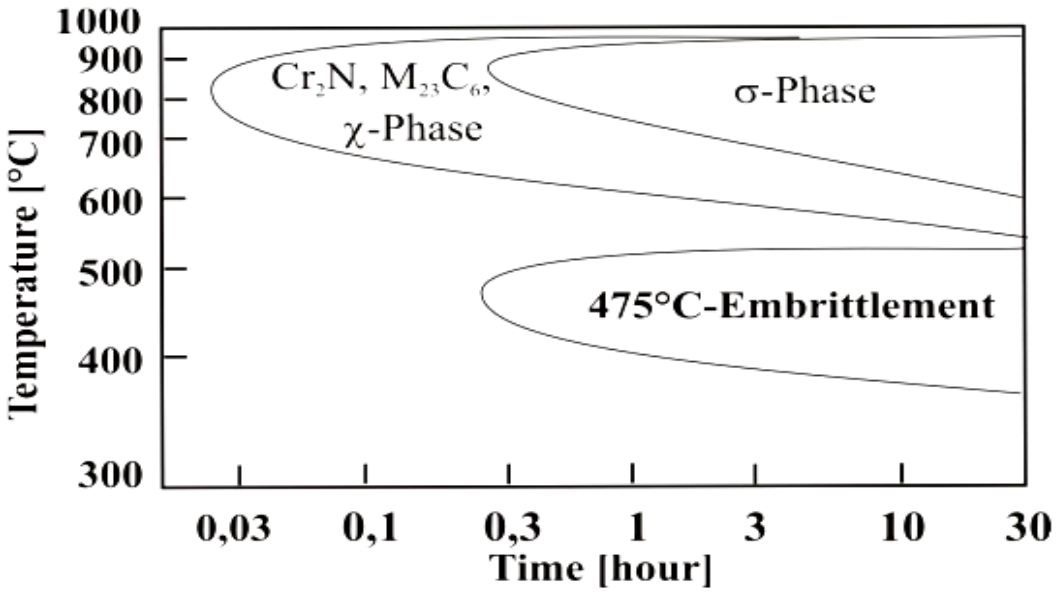

Figure 3.1 TTT diagram of S2205 DSS (Gunn, R1997)

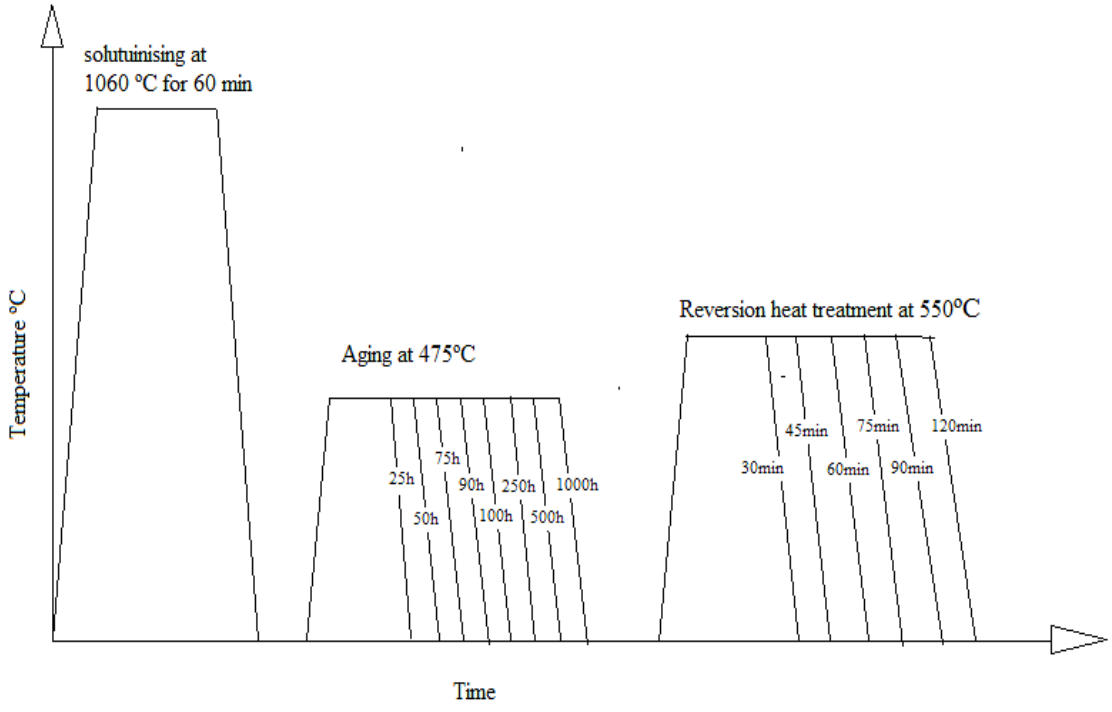

Figure 3.2 Heat treatment cycle.

3.3 Metallography

Standard metallographic techniques were used to prepare the samples for microstructural studies. This includes polishing, etching, and optical microscopy.

The solutionized sample was first roughly polished using a belt grinder until both sides were flat and parallel. It was then polished using SiC sandpapers of 200, 400, 600, 800, 1000 and 1200 grits in succession. After that it was polished to a mirror finish on a velvet cloth mounted on a motor driven polishing wheel and using alumina suspension.

The polished sample was then etched by immersing the sample in the etchant and holding for 120 seconds with agitation. The composition of the solutions used for electro polishing and etching during the investigation is given in Table 3.2.

A Zeiss AXIO Lab.A1^{TM} optical microscope was used to study the microstructure of the polished and etched sample. Images were taken at a suitable magnification to show the distribution and morphology of the ferrite and austenite phases.

Table 3.2 Solutions used for electropolishing and etching in the investigation

Type of microscopy	**Type of treatment**	**Composition**
Optical and SEM	metallography	Beraha‟s tint etchant consisted of 20 mL of HCl, 0.5-1 g of potassium metabisulfite ($K_2S_2O_5$) and 100 mL of distilled water.
TEM	Twin jet polishing	10 vol. % perchloric acid 90 vol. % acetic acid

3.4 X-Ray Diffraction

To identify the phases present in the heat treated samples, samples were subjected to X-ray diffraction studies. The samples were characterized by using JEOL-JDX-8P X-ray diffractometer, (operated with Cu-Kα radiation at 30KV and 20mA). The 2θ range was selected between 40^0 to 50^0 . This range was selected as most of all the major intense peaks of the phases expected in the sample are present in this region. The X-ray diffraction profile consisted of two peaks within this angular range, namely (111) peak of austenite and (110) peak of ferrite. The direct comparison method suggested by (Culity, B. D., and Stock, S. R. 1978) was used to determine the volume fraction of austenite and ferrite. Integrated intensity of the peaks was obtained by measuring the area under the peaks using Origin-Pro 9.0 software. Then the volume fraction of austenite and ferrite were estimated using the following relationship:

$$I\gamma/I\alpha = (R\gamma * X\gamma)/(R\alpha * X\alpha) \quad \text{.....(3.1)}$$

Where Iγ and Iα are the intensities of (111) peak of austenite and (110) peak of ferrite respectively, Xα is the volume fraction of ferrite and Xγ is the volume fraction of austenite; the constants Rα and Rγ are given by the following expression for each peak

$$R = [l/V^2]\,[F.p.\,(LP)]\,e^{2m} \quad \text{.....(3.2)}$$

Where V is the atomic volume of unit cell, F is the structure factor, p is the multiplicity factor, LP is the Lorentz Polarization factor and e^{2m} is the temperature factor.

3.5 Scanning Electron Microscopy (SEM) and Energy Dispersive Spectroscopy (EDS)

The microstructures and fracture surface of all product forms were analyzed at higher magnifications in a JEOL JSM-6380LA scanning electron microscope using the secondary electron (SE) and backscattered imaging modes. The EDS (Energy Dispersive spectroscopy) analysis of the samples was also carried out for the elemental analysis of micro and macro constituents.

3.6 Transmission Electron Microscopy

TEM specimens were prepared by mechanical polishing followed by dimpling down to 20 μm. The dimpled sample was electropolished using a twin jet electropolishing machine. The samples were then analyzed using FEI Tecnai T20 U-TWIN TEM operated at 200KV.

3.7 Charpy Impact Test

Charpy impact tests were conducted on the material to determine the ageing time required for saturation of embrittlement in the material. Charpy impact testing was performed according to ASTM E23 using Charpy specimen with the dimension of 10mm x10mm x55mm. A Charpy V notch inclusive angle of 45^0 a depth of 2mm and a root radius of 0.25mm are machined in the center of the specimen, as shown in Figure 3.3.

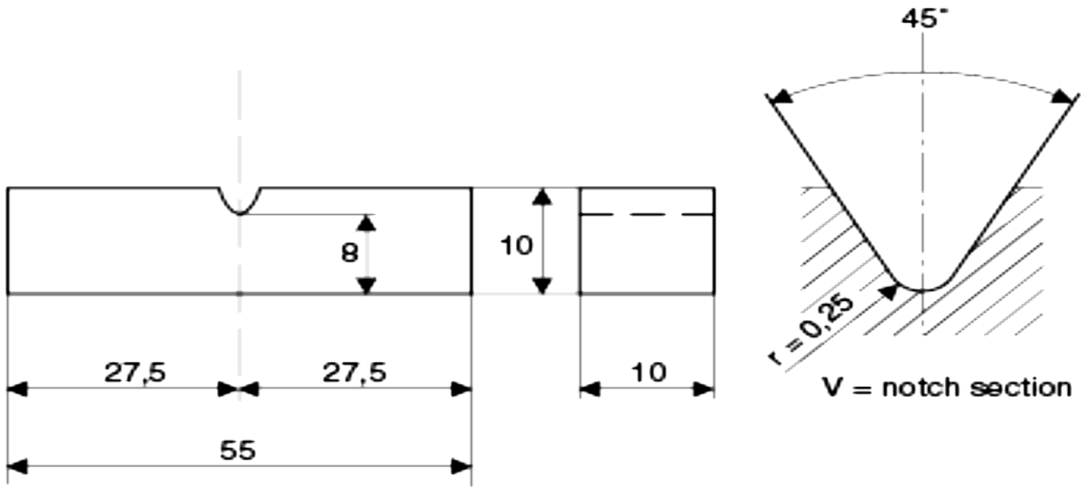

Figure 3.3 Charpy Impact Test specimen geometry (all dimensions are in mm).

3.8 Tensile testing

The tensile samples were machined from the rolled bars in accordance with ASTM A370-14 standard for mechanical testing of steel products. The gauge length of the tensile specimens was 30 mm and the gauge diameter was 6 mm, as shown in Figure 3.4. The tensile testing was carried out as per ASTM E8-M standard using a Shimadzu AG-X plus™ 100kN universal testing machine. A strain rate of 1 mm/min was employed for each specimen. Three samples were tested under each heat treatment condition and the values reported are an

average of these three values. The stress-strain curves obtained during each test were used to estimate tensile properties such as yield strength and tensile strength, whereas, the percentage elongation was estimated by measuring the dimensions of the samples before and after fracture.

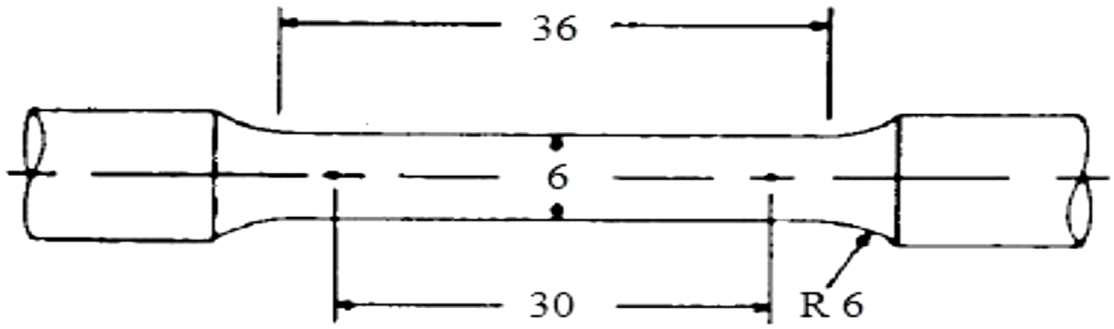

Figure 3.4 Tensile sample geometry (all dimensions are in mm).

3.9 High cycle fatigue test

The high cycle fatigue test was carried out in a resonant fatigue testing machine which is as shown in the Figure 3.5. These tests were carried out at a frequency of 250Hz under fully reversed load condition. The fatigue limit was evaluated as the stress amplitude at which the sample did not fail in 10^7 cycles.

The heat treated specimens are subjected to rotating bending machine. On this machine, cylindrical smooth specimens were mounted and loaded from both ends using rotating chucks. A weight is suspended from one side of the specimen to vary the bending stresses experienced by the specimen surface. Initially, the specimen will experience tensile stresses at its top surface and compressive stresses at its bottom. As the specimen rotates 180 degrees, the stresses will be reversed and the top will be under compressive stresses while the bottom will be under tensile stresses. When the specimen completes one full rotation, the specimen surfaces would have experienced one full loading cycle. The maximum bending stress acting on the specimen surface is given by

$$\sigma = 32\ M/\pi d^3$$

where, σ = the maximum bending stress.

M = the bending moment at the specimen cross-section (weight*distance).

d = specimen diameter.

According to ASTM E466 standard, samples were prepared which is as shown in the Figure 3.6. Ten samples were tested for each stress amplitudes and the number of cycles it would take to fail is recorded. The S-N curve is a plot of the applied stresses versus the logarithm of the number of cycles to failure (N) was plotted for each heat treated condition. The specimens were tested till fractured.

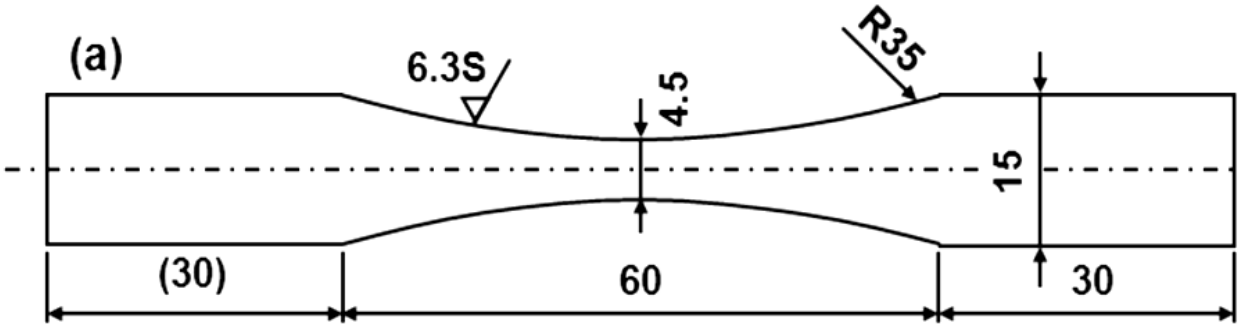

Figure 3.5 Fatigue test sample geometry (all dimensions are in mm).

3.10 Microhardness

The microhardness of the ferrite and austenite phases under each heat treated condition was measured using a Shimadzu HMV-G 20ST micro-Vickers hardness tester with a 25 g load. The samples were polished to a mirror finish and etched so that the ferrite and austenite grains could be distinguished. The load was selected so as to get indentations that are large enough to give accurate results and at the same time, small enough not to be influenced by the adjacent softer or harder phase. For each sample, 10 readings were taken on each phase, and the average of the 5 closest values was reported.

Chapter 4 Results and Discussion

In this chapter the present investigation results are introduced, discussed and compared with the results obtained by other researchers. The chapter is divided into 4 sections. The results of the solutionising heat treatment, 475 °C aging, reversion heat treatment and re-aging heat treatments are presented in section 4.1, 4.2, 4.3 and 4.4 respectively.

4.1 Solution heat treatment

In our investigation it was important to calculate the appropriate solution heat treatment temperature and time because the ferrite content increases with increasing solutionising temperature and time. From the literature (Shilei Li et al. 2015) it is well known that as the ferrite content increases the extent of degradation of the material also increases, hence in order to get required amounts of austenite and ferrite ratio the selection of solution heat treatment temperature and time was very important. The pseudo binary diagram of 70 wt. % Fe-Cr-Ni as shown in Figure 4.1 was used as the reference to evaluate the microstructural evolution and composition distribution in stainless steels during solution heat treatment (Gunn R. 1997).

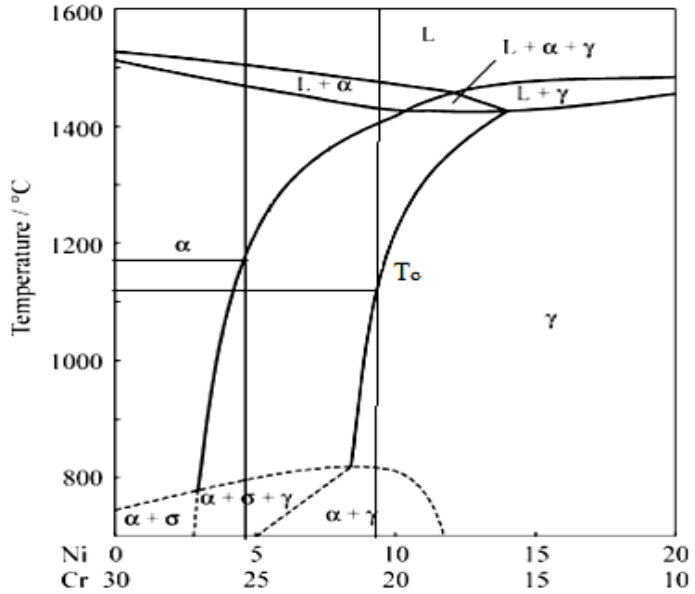

Figure 4.1 The Pseudo binary diagram of 70wt% Fe-Cr-Ni

The temperature T_o as shown in the Figure 4.1 for our material was calculated by using Cr and Ni equivalent relations which is given below,

$$\text{Cr (equivalent)} = \%\text{Cr} + \%\text{Mo} + 0.7 \times \%\text{Nb}$$

$$\text{Ni (equivalent)} = \%\text{Ni} + 35 \times \%\text{C} + 20 \times \%\text{N} + 0.25 \times \%\text{Cu}$$

By substituting the chemical composition (%wt) of the elements, the $Cr_{(equivalent)}$ value was found to be 24.414 and $Ni_{(equivalent)}$ value was 9.193. Using these values the T_o value was obtained from the pseudo binary diagram of 70wt% Fe-Cr-Ni (T_o= 1060 ^oC).

If the solution treatment temperature (T_o) is increasing the volume fraction of the ferrite phase will also increase with larger ferrite grain size and there will be no change in the chemical composition of austenite phase even though the volume fraction is decreased. Within the ferrite phase the Cr content will be decreased and the Ni content will be increased which in turn will increase the probability for the formation of secondary austenitic phase in the dual phase matrix (J.K.L. Lai et al. 1995). Extending the solution treatment time the ferrite phase will gradually dissolve into the austenite phase and the undissolved ferrite will become finer and disconnected. (Li S.L et al. 2013) Hence solution treatment time of 60 minutes was selected in our investigation.

4.1.1 Microstructure

Figure 4.2 shows the SEM micrograph of the as-received S2205 DSS in the wrought form in which austenitic islands are embedded in the ferritic matrix with some undissolved precipitates. Hence, in order to dissolve these harmful precipitates samples were subjected to solution heat treatment by heating it to 1110 ^oC for 60 minutes. The solution heat treatment was also done to adjust the austenite and ferrite phase proportions which can be seen in the Figure 4.3. If any macro segregations are present in the sample the solution heat treatment will help to eliminate them.

4.1.2 X-ray Diffraction

The solutionized sample was quantitatively analyzed by an X-ray diffractometer to determine the volume fractions of ferrite and austenite. Figure 4.4 shows the X-ray

diffraction pattern obtained from the sample. It shows the (111) peak of austenite and the (110) peak of ferrite. The integrated intensities of these peaks were calculated and substituted in equation 3.1 along with the other constants. The volume fraction of ferrite was found to be 54% and that of austenite, 46%. The relative volume fraction was found to be the same under each heat treated condition.

4.1.3 Mechanical properties

The yield strength of 456 MPa and the ultimate tensile strength of 726 MPa with 42% ductility was obtained in the solution heat treated condition. It had the impact strength of 296 J. The fractured surface of solution heat treated tensile sample observed under SEM and is as shown in the Figure 4.36. The fractured surface morphology was fully ductile with dimples and no inclusions were found throughout the fracture surface.

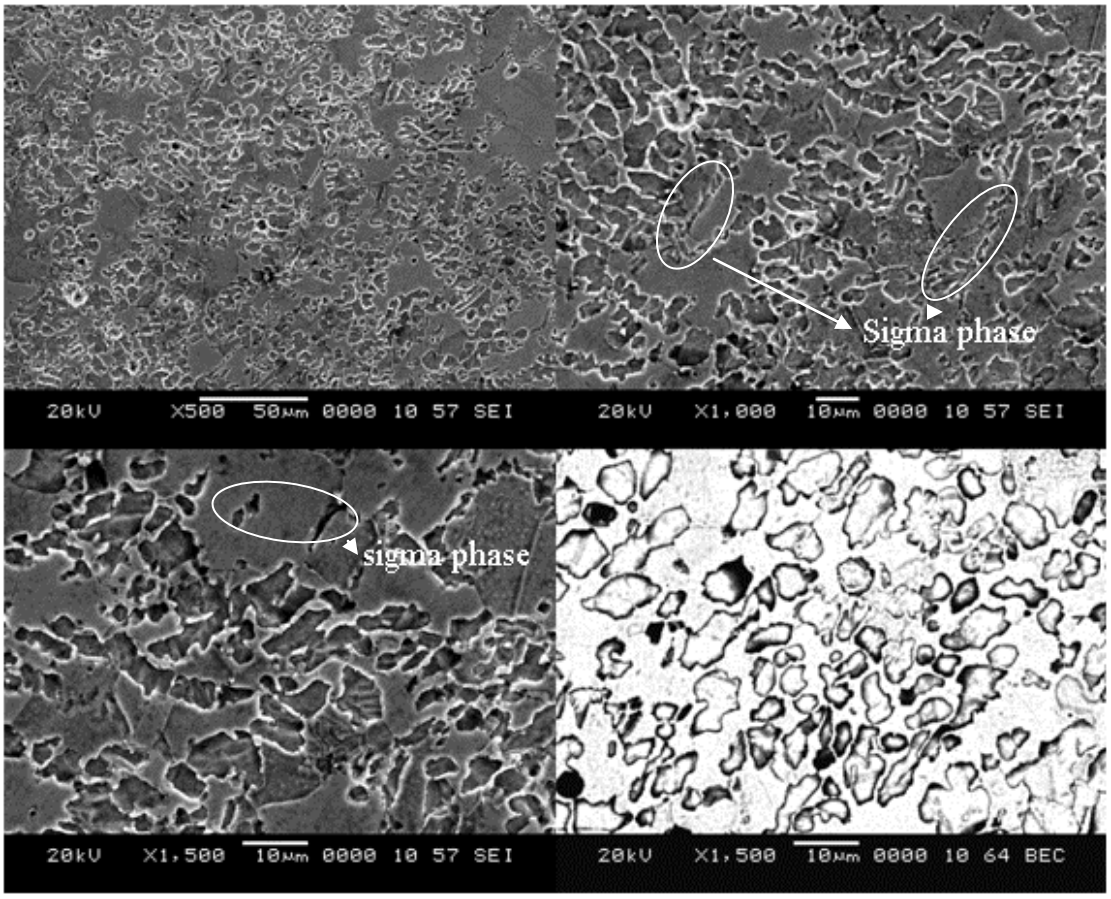

Figure 4.2 Microstructure of as received S2205 duplex stainless steel sample (Etchant: Beraha's tint etch).

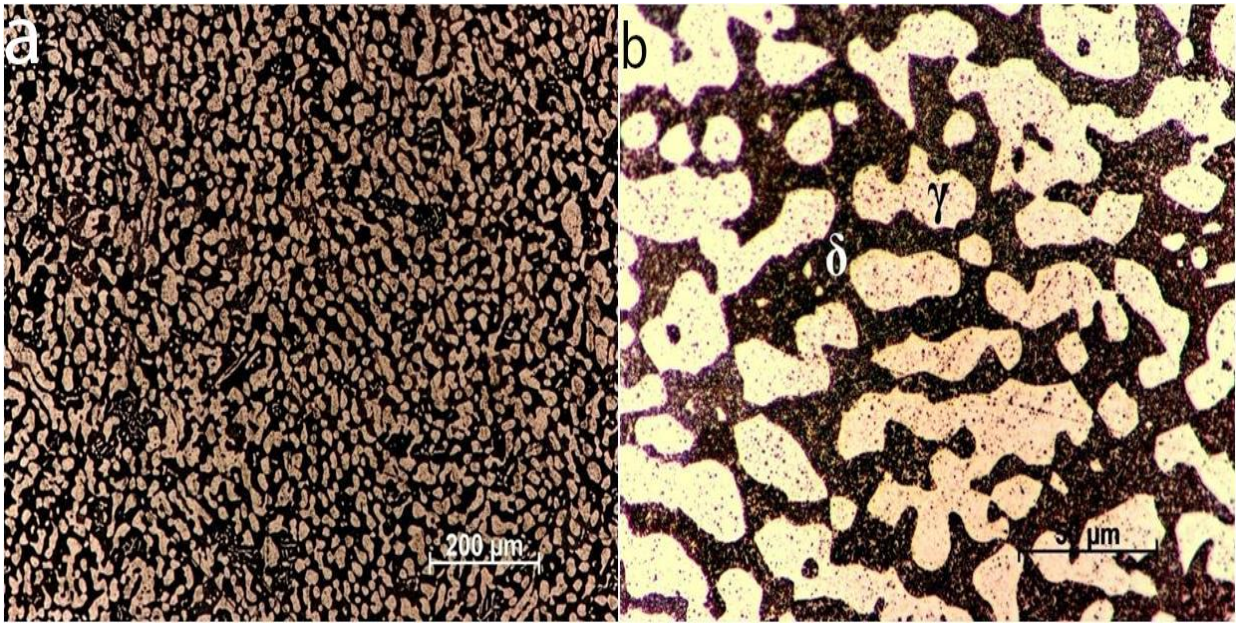

Figure 4.3 Microstructure of S2205 after solution heat treatment (a) OM image of distribution of austenite grains in the ferrite matrix (Magnification: 100X). (b) OM image of phase morphology (Magnification: 500X).

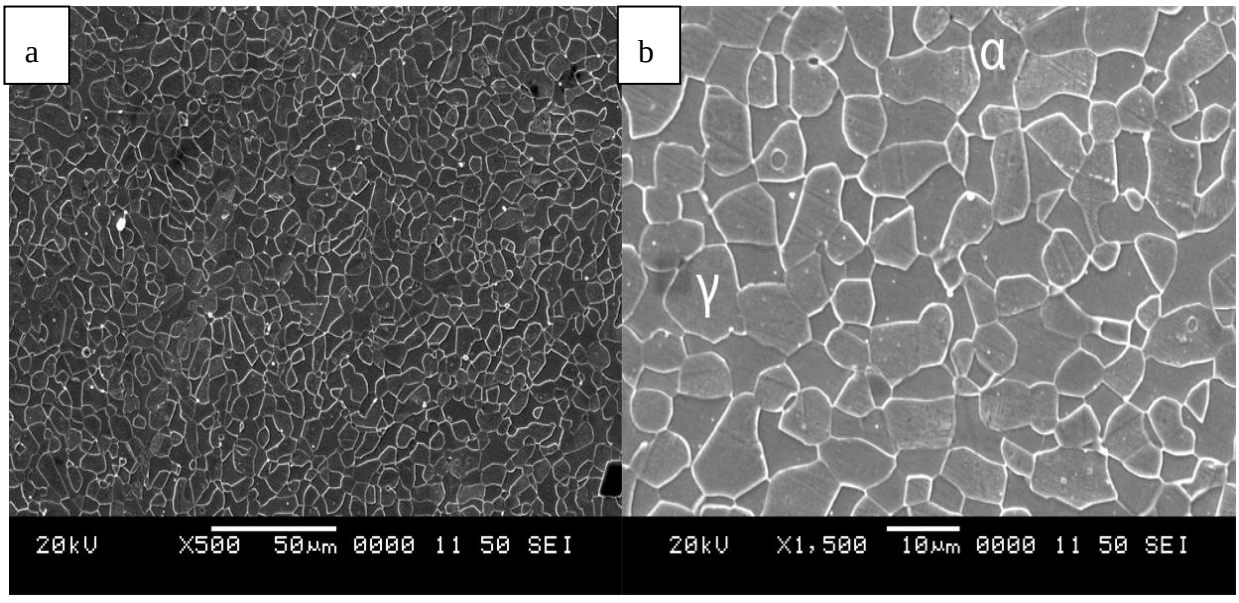

Figure 4.4 (a) SEM image of distribution of austenite grains in the ferrite matrix(Magnification: 500X). (b) SEM image of phase morphology (Magnification: 1500X). Etchant: Beraha's tint etch.

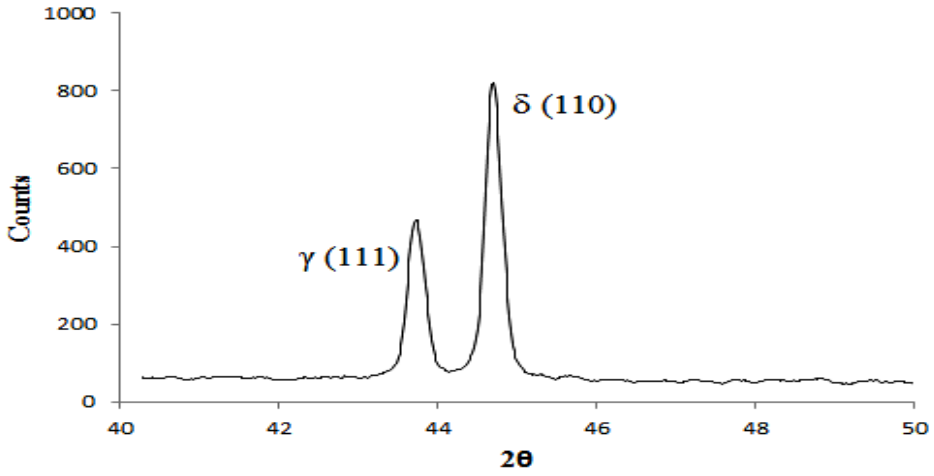

Figure 4.5 X-Ray diffraction pattern of S2205 DSS in solution heat treated condition.

4.2 Effect of 475 ^{0}C embrittlement on the microstructure of the annealed DSS.

The embrittlement rate is highest at 475 ºC hence it is commonly known as 475 ºC embrittlement (Sahu.J.K et al. 2009). In our investigation the annealed samples were aged at 475 ^{0}C for varying periods and their mechanical properties were correlated with the corresponding microstructural changes.

The Figure 4.6 depicts the scanning electron microscopic image of 1000 hours sample. We could not distinguish any major microstructural changes associated with the 475 ºC from Scanning electron microscopy hence the 1000 hours aged samples were further examined under High resolution transmission electron microscope (HR-TEM). Figure 4.7 to 4.10 shows the HR-TEM image of the [1100^{0} C annealed for 1 hour + 1000 hours aged at 475^{0} C] sample. In Figure 4.7 we can see the mottled contrast in the ferrite matrix at nano-scale which is the typical indication of the presence of Fe-rich α and Cr-rich α' precipitates formed by the spinodal decomposition (Sahu.J.K et al. (2008). But we could not distinguish between α and α' precipitate from HR-TEM results even at higher magnifications since they both have similar lattice parameter as that of Fe (Li.S.L et.al (2013). In this study, we also found that the α' precipitate associated with the co-precipitation of Cr_2N precipitates in the ferrite matrix. The Figure 4.8 depicts the HAADF-STEM images were we can see the majority of Cr_2N precipitates precipitated intergranularly and along the ferrite-austenite interface which can also be seen in the Figure 4.9 and Figure 4.10. The Cr_2N precipitates is having a small

rod like morphology near the ferrite-austenite interface, whereas they look like larger rods with bifurcated ends in the interior ferrite matrix which is evident in the Figure 4.9. The results from EDS and elemental mapping results is as shown in Figure 4.11 and from the results we can say that the Cr_2N precipitates are rich in Cr, Ni and Mo atoms.

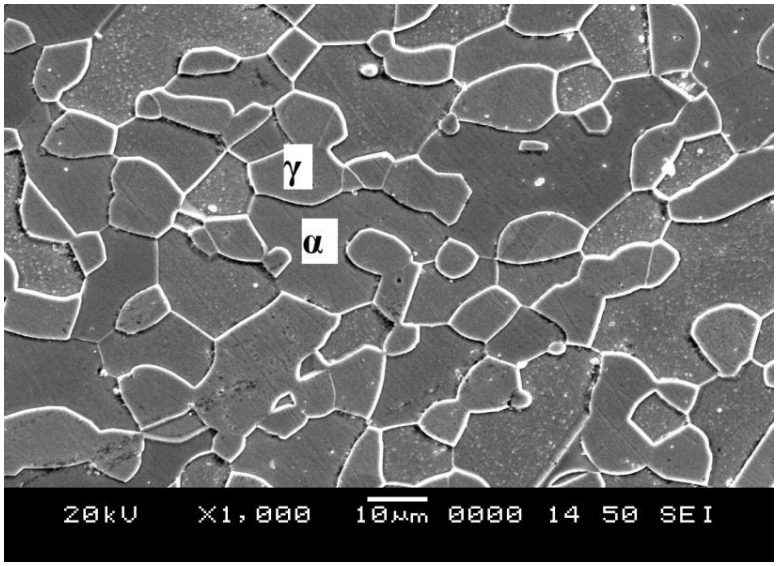

Figure 4.6 SEM micrograph of 1000hrs aged sample.

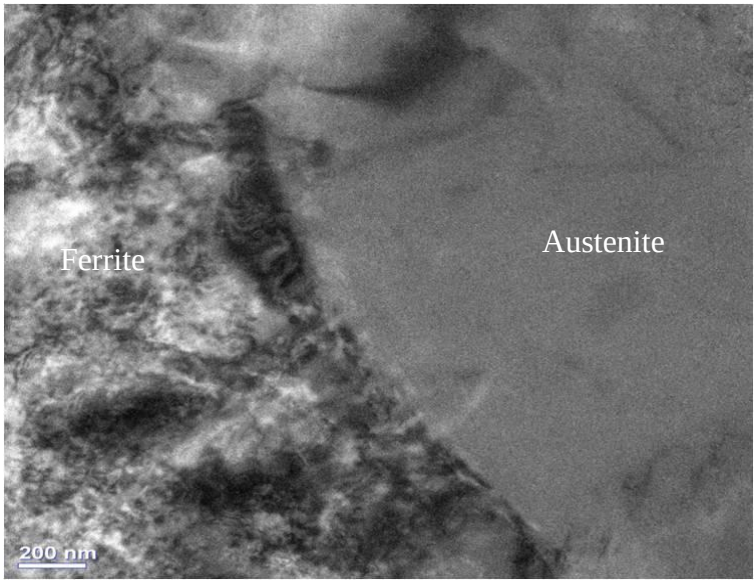

Figure 4.7 HR-TEM image of 1000 hours aged sample showing mottled contrast ferrite region and precipitate free austenitic phase.

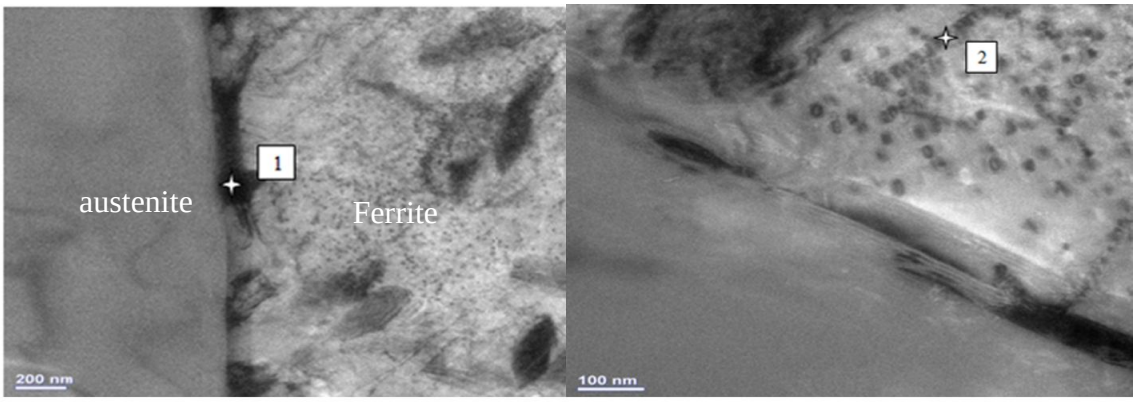

Elements(%wt)	Cr	Ni	Mo
Point 1	72	4	22
Point 2	64	1.3	6

Figure 4.8 HR-TEM image of 1000 hours aged sample with EDS result of Cr_2N [point 1] and alpha prime precipitate [point 2].

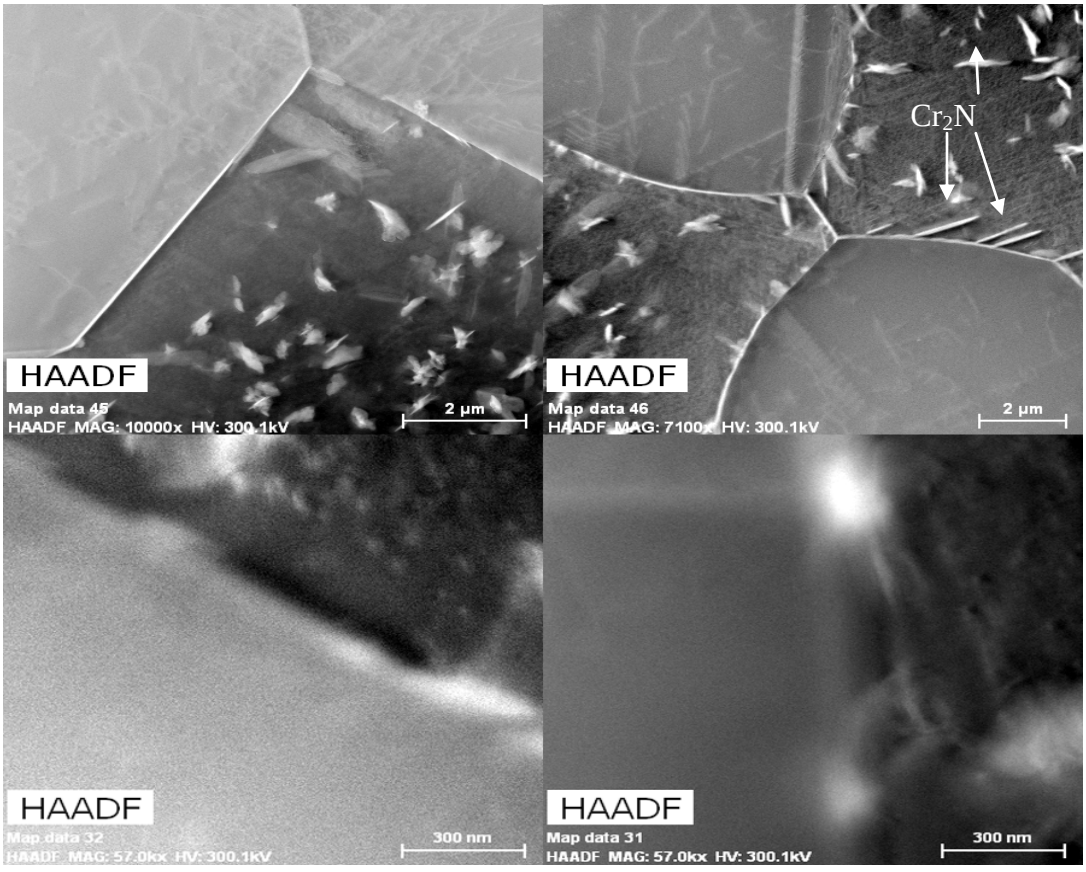

Figure 4.9 HAADF STEM image of 1000hours aged sample.

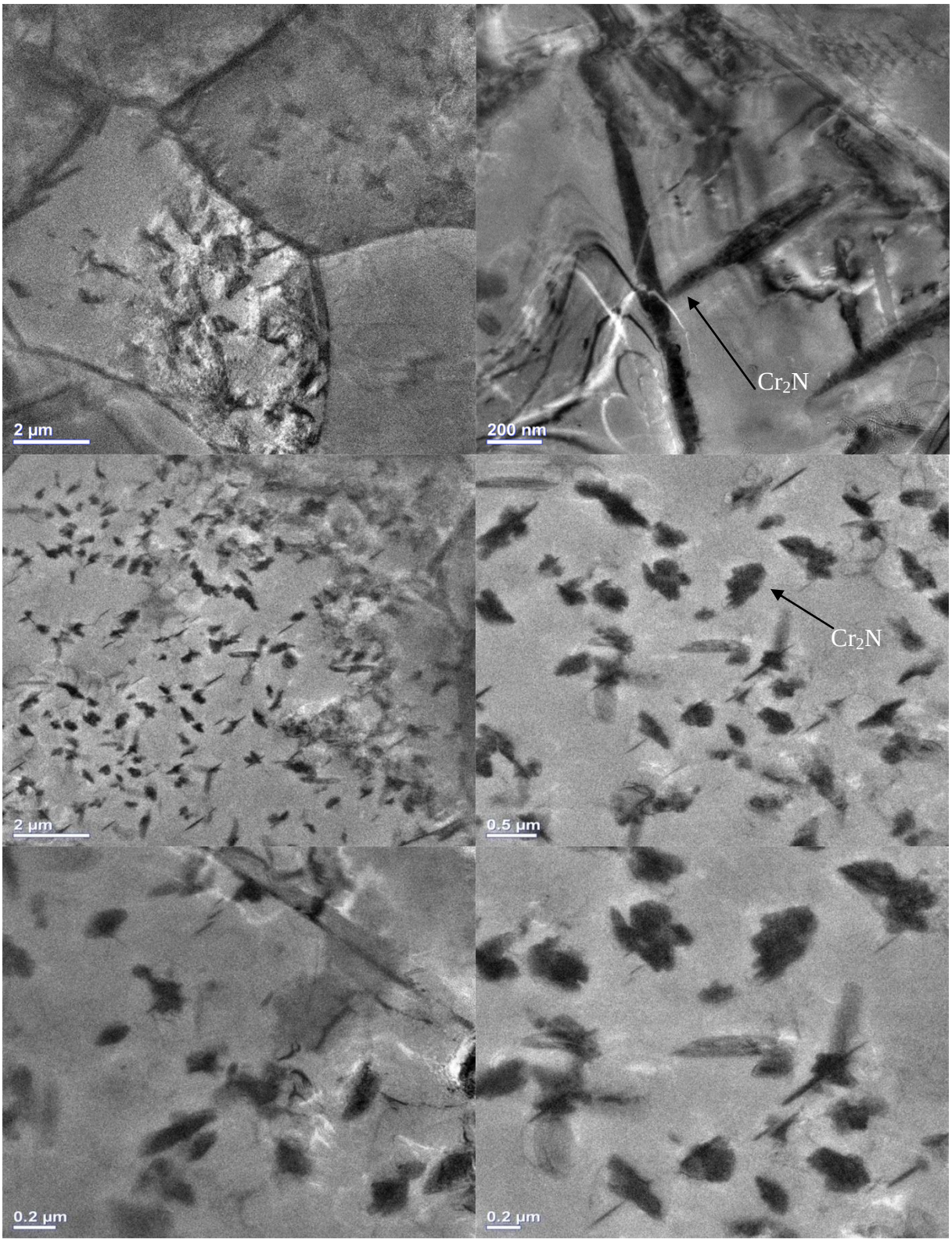

Figure 4.10 HR-TEM image of 1000 hours aged sample showing the morphology of Cr_2N precipitates in ferrite matrix.

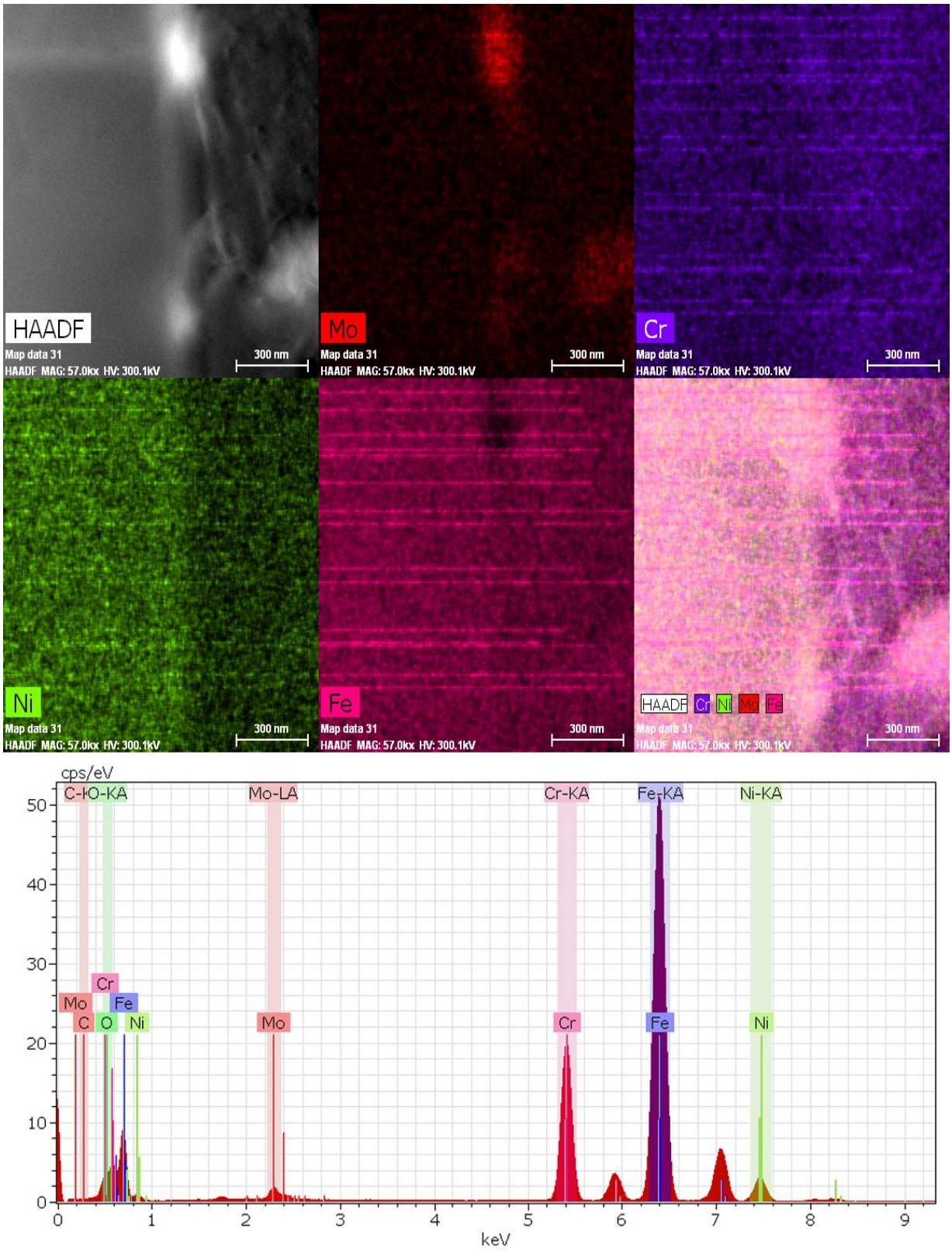

Figure 4.11 Elemental mapping and spectra analysis result of 1000 hours aged sample.

4.3 Effect of Reversion heat treatment on the microstructure of thermally embrittled DSS

Figure 4.12 to 4.14 shows the HR-TEM image of the [annealed + 1000hrs aged + 60minutes RHT d] sample and Figure 4-16 depicts the elemental mapping results.

From the Figure 4.12 it is evident that the mottled structure as found in embrittled sate is being disappeared in the ferritic matrix after reversion heat treating at 550 °C for 60 minutes. The disappearance of the mottled structure in the ferritic phase indicates that the Fe-rich α and Cr-rich α' is dissolved inside the ferrite matrix. But still some Mo-rich precipitate was found near the ferrite austenite grain boundary as seen in the Figure 4.13. In the HAADF image as seen in the Figure 4.14 the precipitate free ferritic and austenitic phase can be seen and also from the elemental mapping results it is evident that both the phases are precipitate free in this heat treated condition

Mechanism of recovery

According to Fe-Cr phase diagram, the spinodal decomposition in ferrite is due to the presence of the miscibility gap in the Fe-Cr system. The spinodal decomposition in the ferrite matrix takes a very long time because of the low atomic mobility at lower temperature (400 °C) (Li, S. L. et.al (2013). However the reversion heat treated temperature 550 °C is above this (α + α') miscibility gap, the ferrite gets homogenized again or in other words (α + α') will become thermodynamically unstable and dissolve quickly inside the ferrite matrix when they are heat treated at 550 °C for shorter duration i.e. maximum of about 60 minutes. If the time exceeds beyond 60 minutes there is a possibility for the formation of other intermetallic phases like R-phase, σ-phase or γ-phase.

Effect of time on reversion heat treatment

If the reversion heat treatment time exceeds more than 60 minutes it will result in the formation of R-phase precipitate in the ferrite matrix which is evident in our studies. The Figure 4.17 to Figure 4.20 shows the SEM image of reversion heat treated samples for various durations. In 75 minutes reversion heat treated sample, we can see the white spot in the ferrite phase as seen in the Figure 4.17 and is identified as the R-phase. The volume

fraction of R-phase was increasing with the increase in the reversion heat treatment time as seen in Figures 4.17 to 4.20. As seen in the Figure 4.21, the HR-TEM image of the 120 minutes reversion heat treated sample shows the R-phase which is distributed throughout the ferrite matrix. This R-phase again results in the embrittlement of the ferrite phase, which degrades its mechanical properties. From the EDS and elemental mapping results as shown in the Figure 4.22, it is evident that this R-phase is rich in Cr and Mo atoms.

But for the sample reversion heat treated at 550 ºC for 120 minutes, also showed the presence of secondary austenite (γ_2) and R-phase in the matrix as shown in the Figure 4.19 and Figure 4.20. The chemical composition of secondary austenite and R phase was obtained from EDS as shown in the table 4.5 proved the existence of secondary austenite and R phase. Kuroda, T., and Matsuda, F. (1994) found that Secondary austenite is the phase transformation product of ferrite with FCC crystal structure. In the Figure 4.20 we can see that the γ_2 is formed at γ/α phase boundaries and is also formed in the interior of the ferrite grains. (Ramirez, A. J. Et al. 2003) Also, we can see the lack of uniformity in the thickness of the secondary austenite which may be due to the following factors

1. A variation in α/γ interface energy which depends on the orientation relationship of the primary austenite (γ_1) particle with ferrite and also depends on the interface plane. The energy of the interface is an important factor for determining its mobility which makes the γ_2 growth reaction faster in certain locations along α/γ interface.

2. The availability and diffusion path for γ forming elements. When the α/γ interface has the large amounts of ferrite, the growth of γ_2 is more prone to occur because of the advancing interface looks at fresh ferrite. This is supported by the lateral planes of Widmansttaten Austenite have thicker γ_2 films at their tip than along their sides.

From the EDS values it is evident that there exists a significant difference between these two types of Austenite.

The growth of secondary austenite is mainly induced because of the chromium depletion arising due to dissolution of chromium rich alpha prime precipitate in the ferritic phase. From

the Figure 4.19 we can see that the secondary austenite is formed in two different ways ie., the coupled lamellar growth and only austenite growth leaving larva type carbides.

SEM image 120 minutes reversion heat treated samples confirm that very fine R phase (white spots) is precipitated continuously throughout the ferritic phase. The EDS results clarified that the R phase is identified as an intermetallic compound, composed of higher Mo and Ni contents. Hwang, T. H Et al. (2014) also found R phase as an intermetallic compound with higher Mo and Ni contents

Table 4.1 EDS values obtained from 120 minutes reversion heat treated sample

Intermetallic phase	**Cr**	**Ni**	**Mo**
R phase	24.4	4.8	9.8
Secondary Austenite	24	7	12

When the samples are reversion heat treated for 120 minutes, the ferrite phase is again embrittled by the R-phase, which can be seen in the Figure 4.20. As reported in Gunn, R. (Ed.). (1997) R-phase is a Molybdenum rich precipitate which will be formed when DSS is exposed to the temperature of 550 – 600 ^{0}C for longer duration and will be mainly formed in both inter and intra-granular sites. It is evident in our studies that the R-phase is found throughout the ferrite matrix and is rich in Molybdenum. While in the case of 60 minutes RHT d condition, very few Mo rich precipitate was found only near the grain boundary. But when the reversion heat treatment time was increased to 120 minutes, the R-phase was distributed throughout the ferrite matrix resulting in the embrittlement of the ferrite phase.

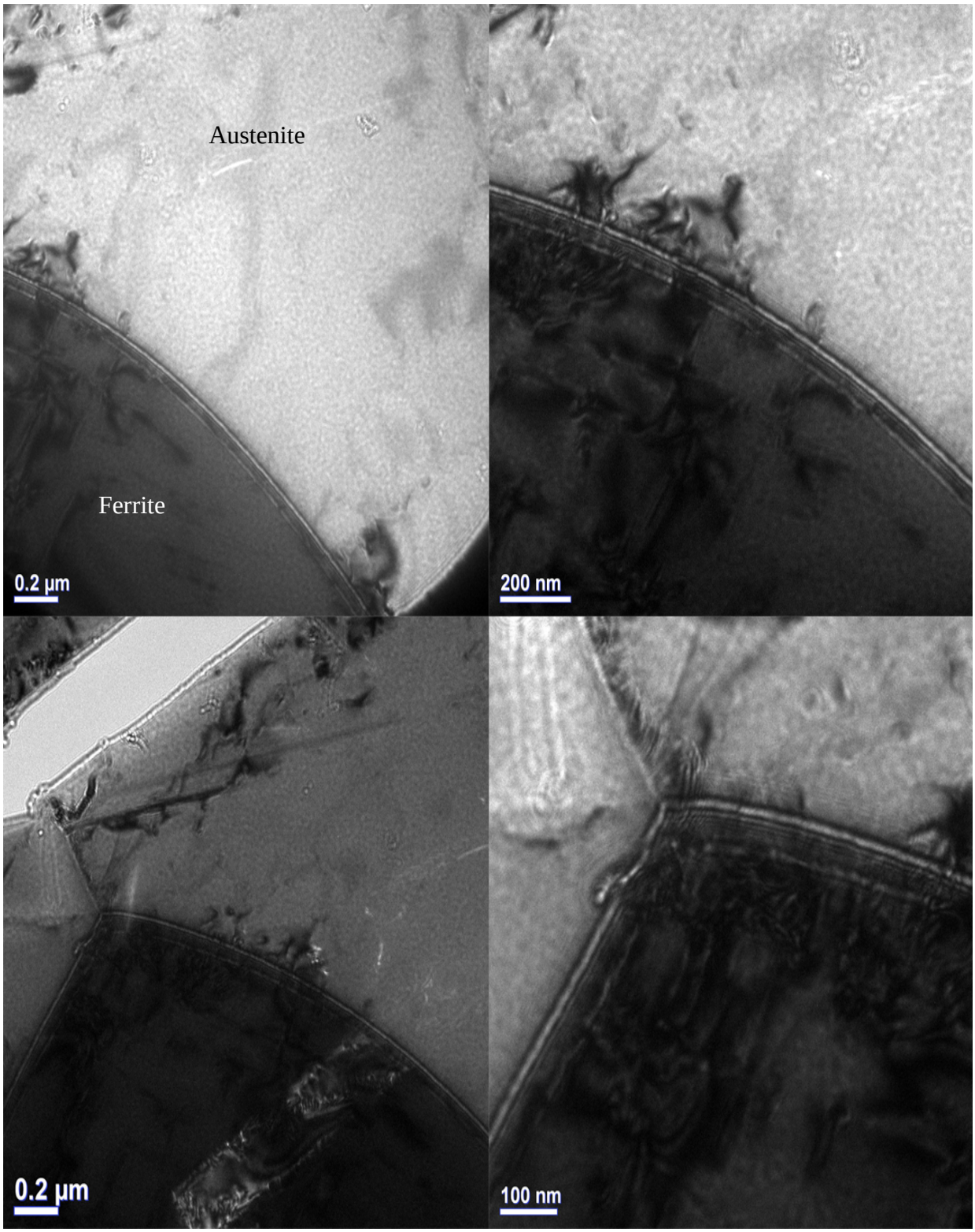

Figure 4.12 HR-TEM image of 60 minutes reversion heat treated sample showing clear austenite phase and ferrite phase with some dislocations.

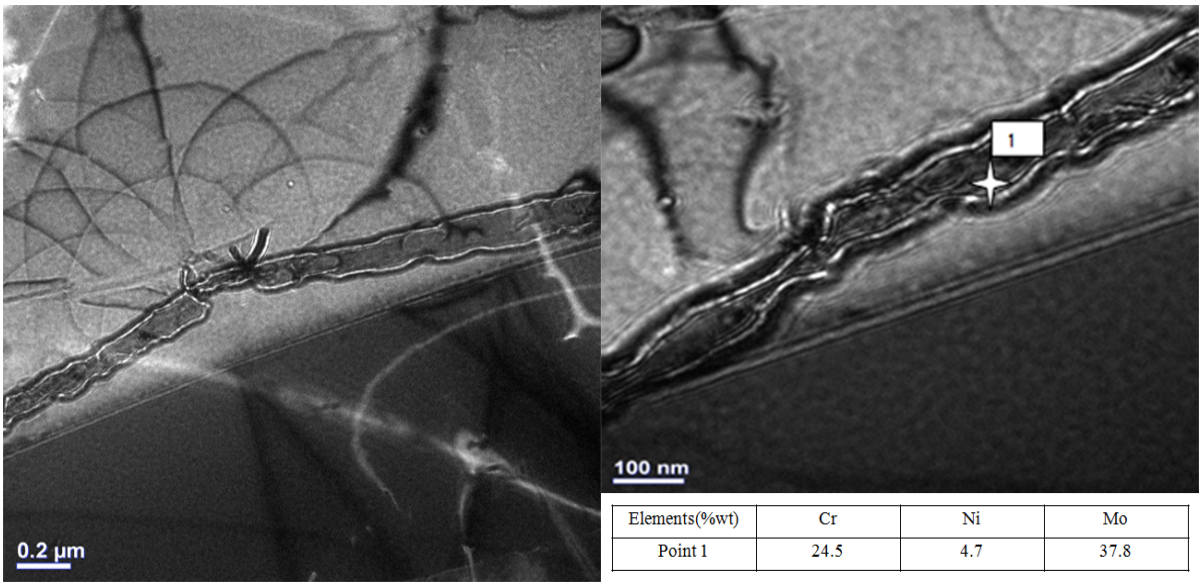

Elements(%wt)	Cr	Ni	Mo
Point 1	24.5	4.7	37.8

Figure 4.13 HR-TEM image of 60 minutes reversion heat treated sample showing the Mo-rich precipitate near the grain boundary with EDS result at higher magnification.

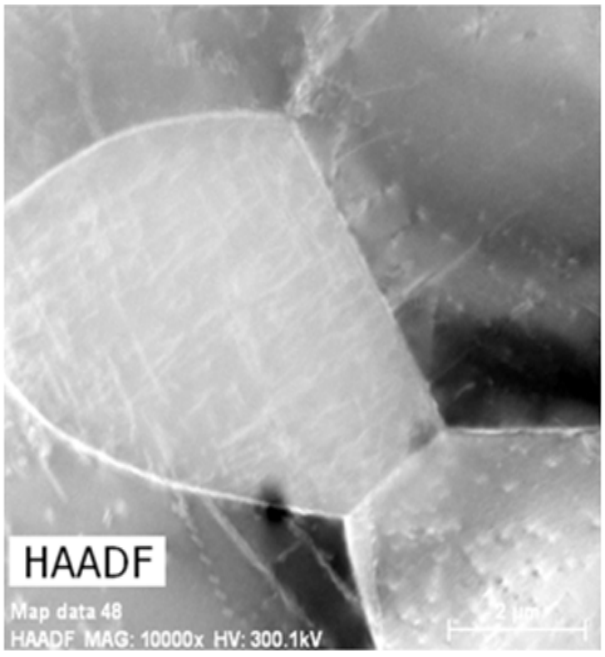

Figure 4.15 HR-STEM image of the 60 minutes reversion heat treated sample

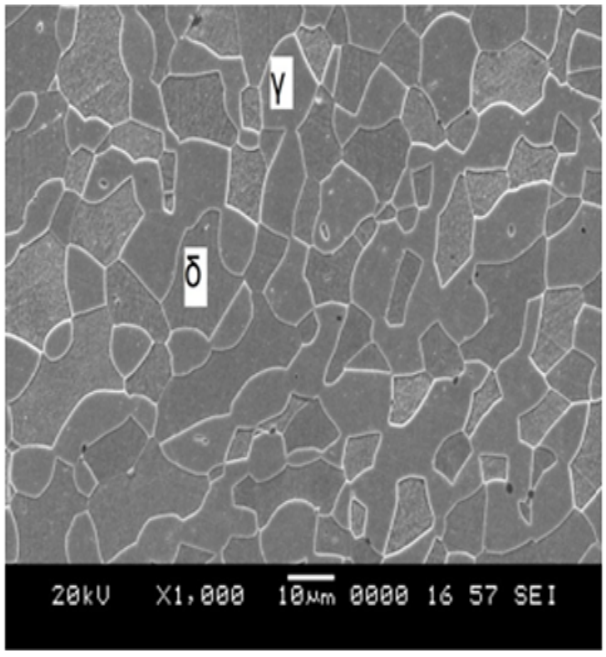

Figure 4.14 SEM image of the 60 minutes reversion heat treated sample.

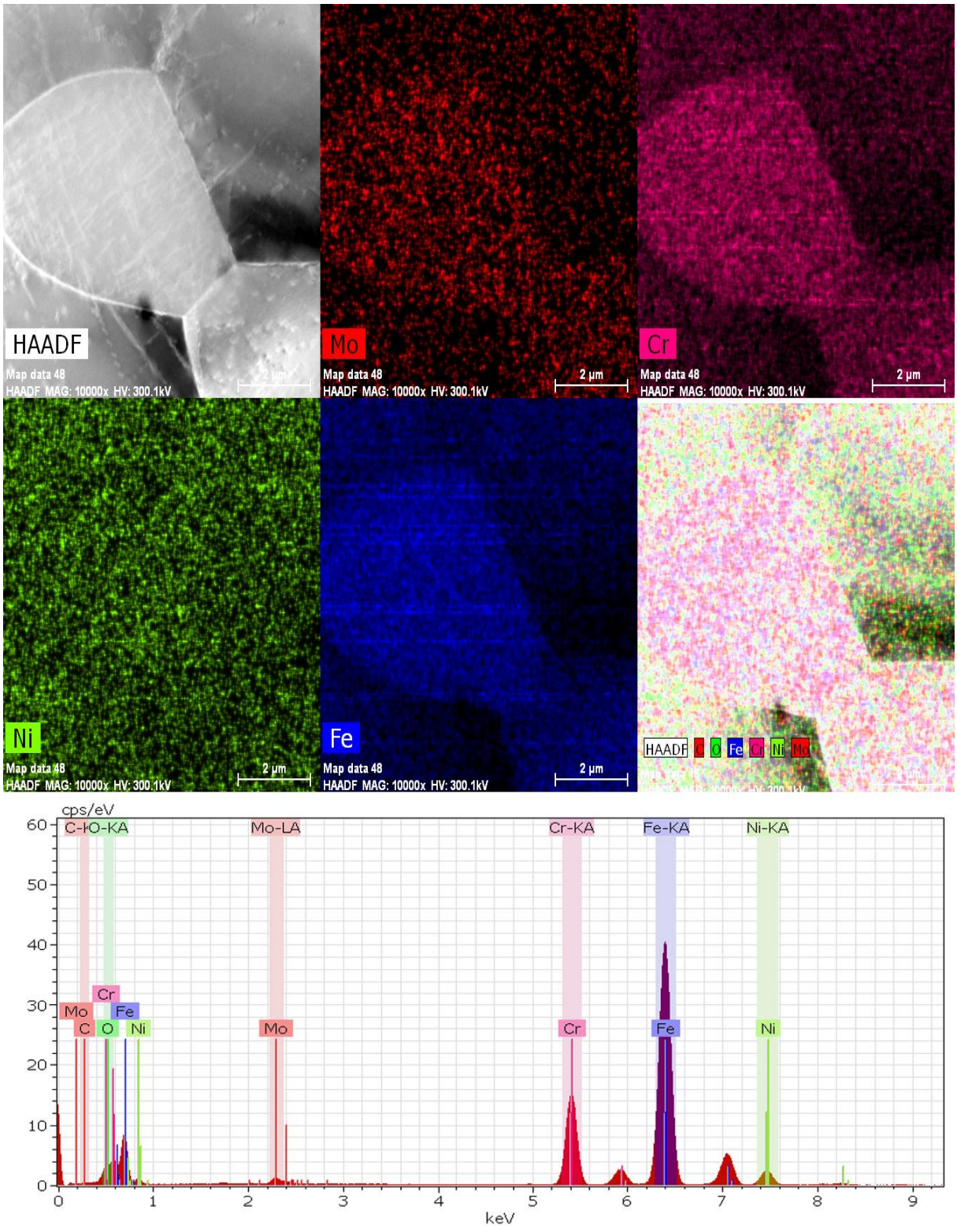

Figure 4.16 Elemental mapping and spectra analysis result of 60 minutes reversion heat treated sample.

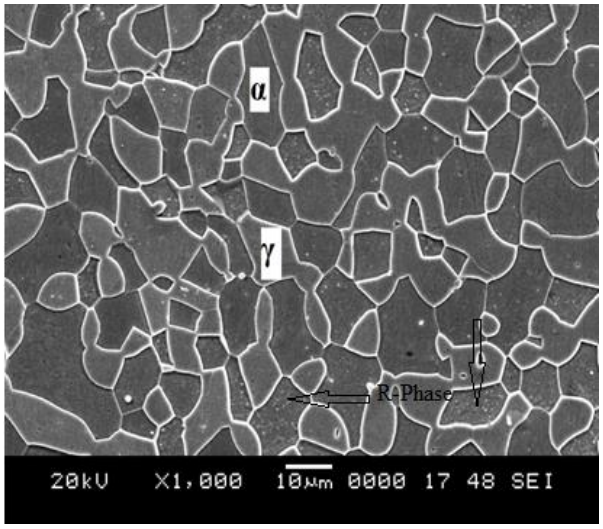

Figure 4.17 Microstructure of 75 minutes reversion heat treated sample observed under SEM.

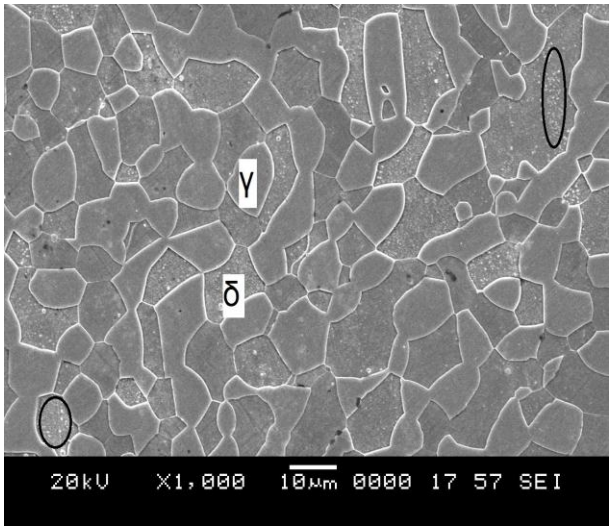

Figure 4.18 Microstructure of 90 minutes reversion heat treated sample observed under SEM.

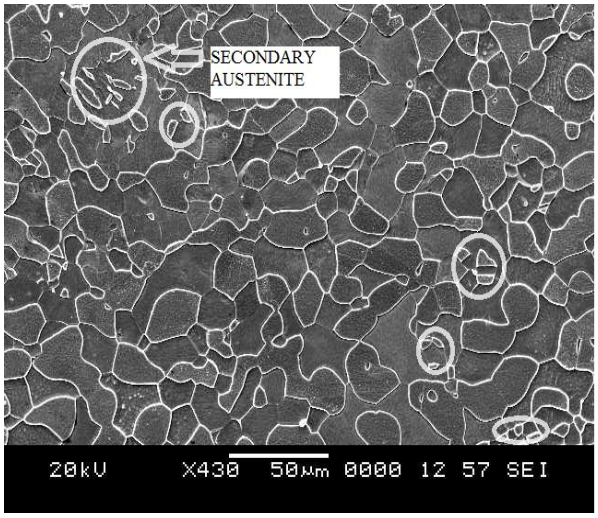

Figure 4.19 Microstructure of 120 minutes reversion heat treated sample observed under SEM.

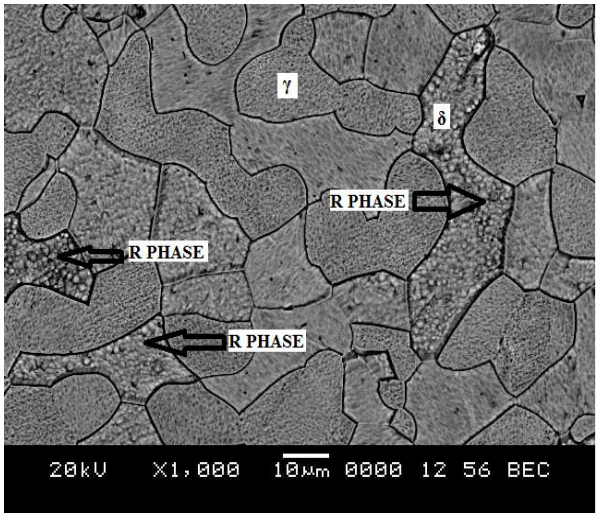

Figure 4.20 Microstructure of 120 minutes reversion heat treated sample observed under SEM.

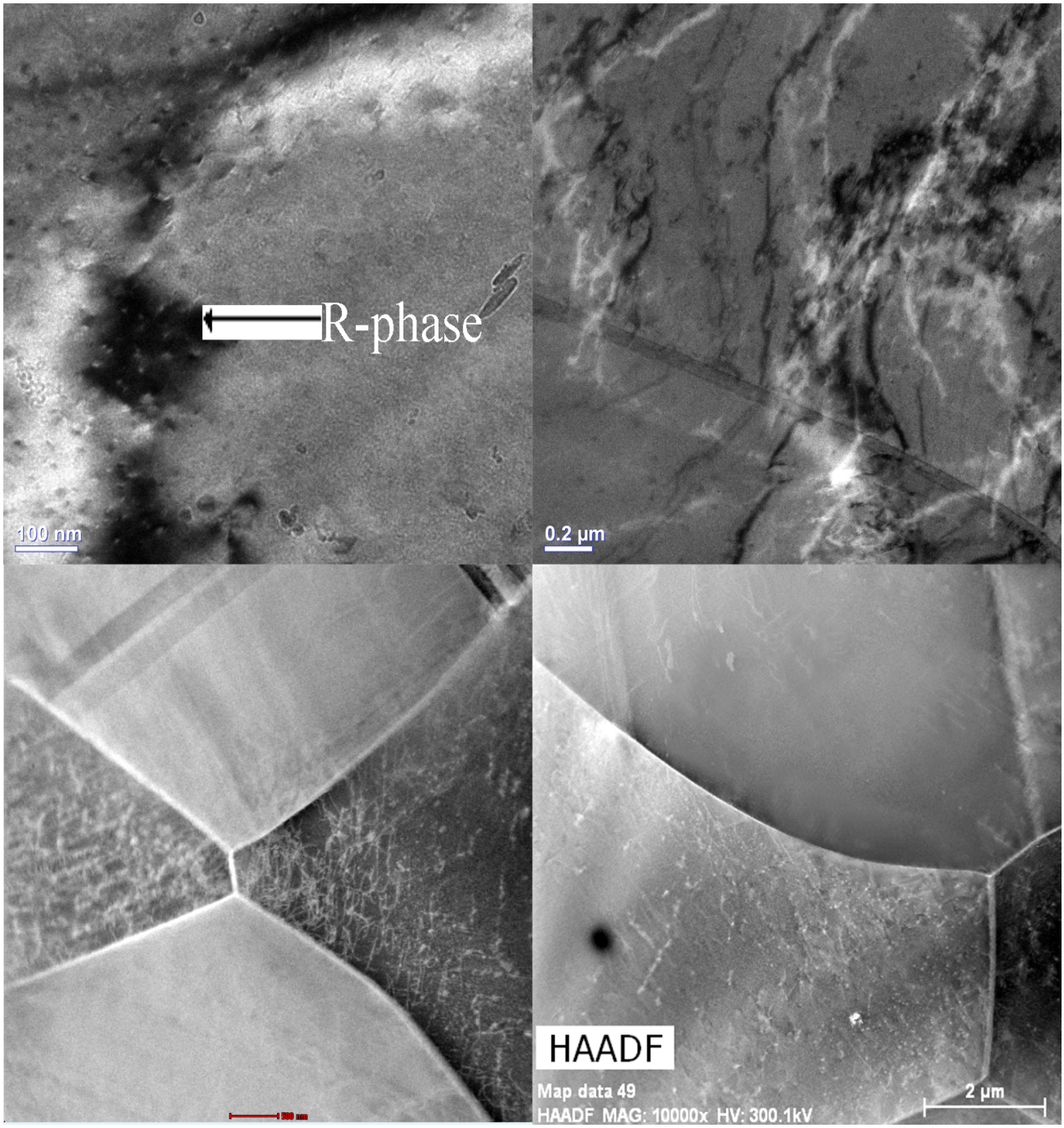

Figure 4.21 HR-TEM image of the 120 minutes reversion heat treated sample.

Table 4.2 EDS value of R-phase.

Elements(%wt)	Cr	Ni	Mo
R-phase	26.5	4.5	9.8

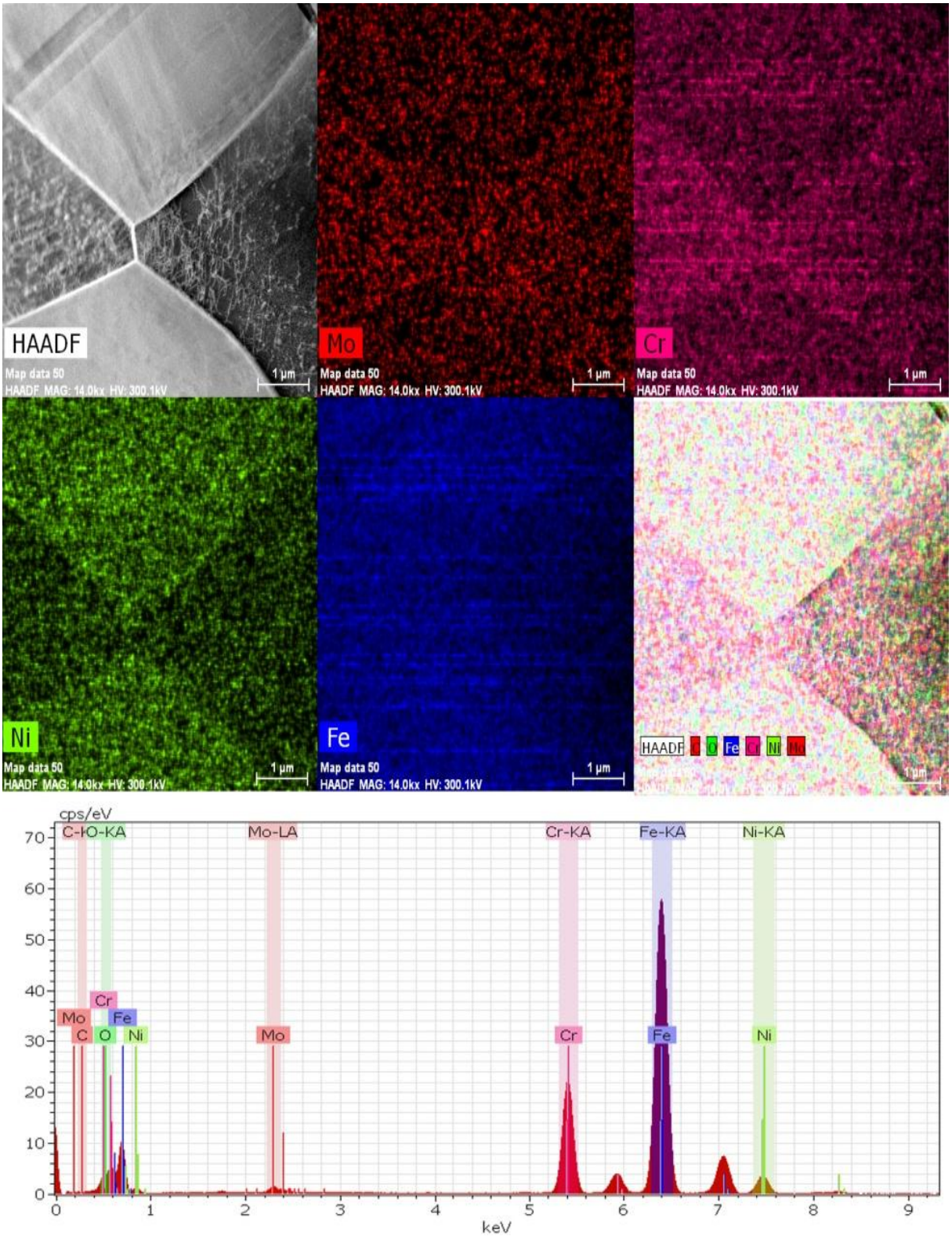

Figure 4.22 Elemental mapping and spectra analysis result of 120 minutes reversion heat treated sample.

4.4 Effect of re-aging on the microstructure of the 60 minutes reversion heat treated DSS

The Figure 4.23 shows HR-TEM image of the [Annealed + 1000hours aged + 60minutes RHTd + re-aged] sample and Figure 4.24 depicts the elemental mapping results and the spectral analysis of the re-aged sample. The mottled contrast with the ferrite matrix at nanoscale can be seen in the Figure 4.23 (a) which is the typical indication of the spinodal decomposition as seen in the aged sample. Therefore, we can say that during re-aging despite the reversion heat treatment, the spinodal decomposition remained as the primary mechanism of thermal embrittlement. In this heat treated condition, we can see needle shaped chromium nitride precipitates formed near γ/α phase boundaries. However, it is also found that Cr_2N precipitate being propagated inside the Cr and Mo lean austenitic phase near the grain boundary as seen in the Figure 4.23 (b). This is because Cr_2N are usually associated with the Chromium depleted zone in its vicinity which is referred as an interphase attack zone.

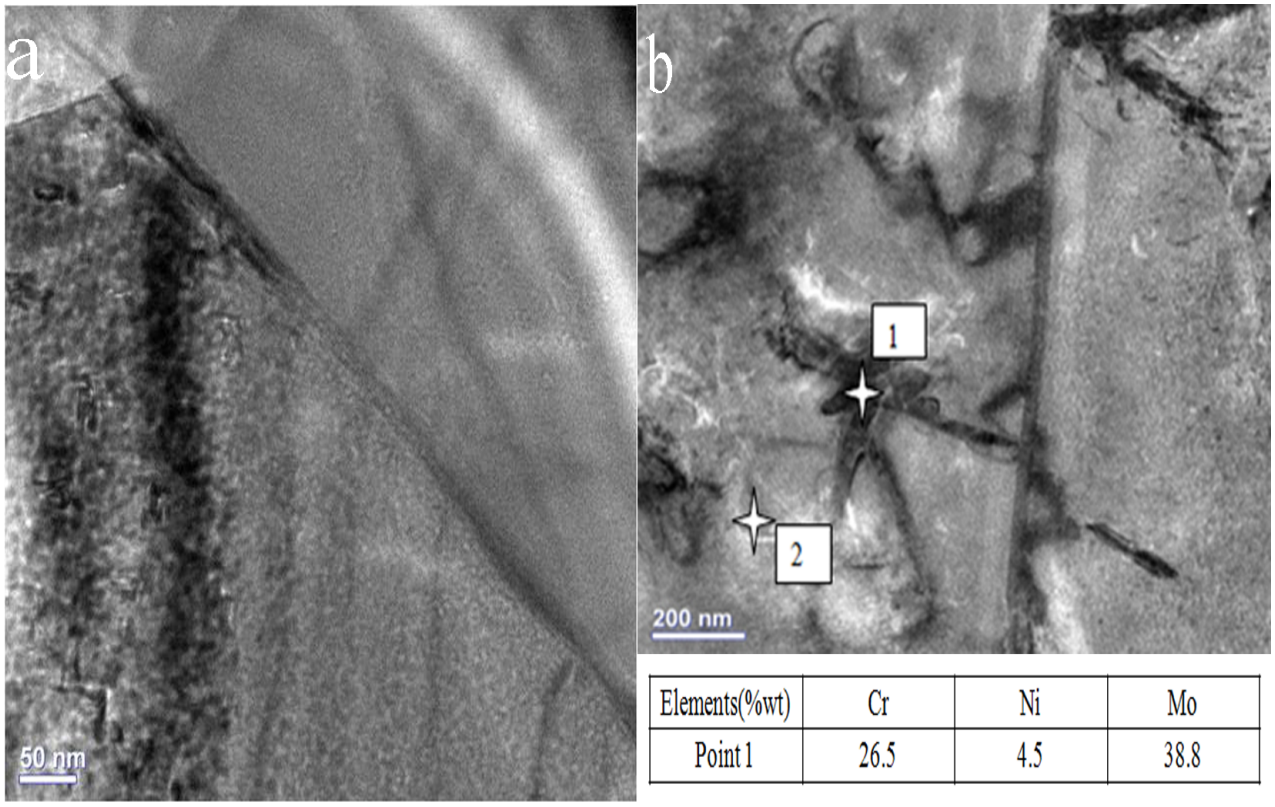

Elements(%wt)	Cr	Ni	Mo
Point 1	26.5	4.5	38.8

Figure 4.23 (a) HR-TEM image of the 100 hours re-aged sample and (b) HR-TEM image of the 100 hours re-aged sample with EDS

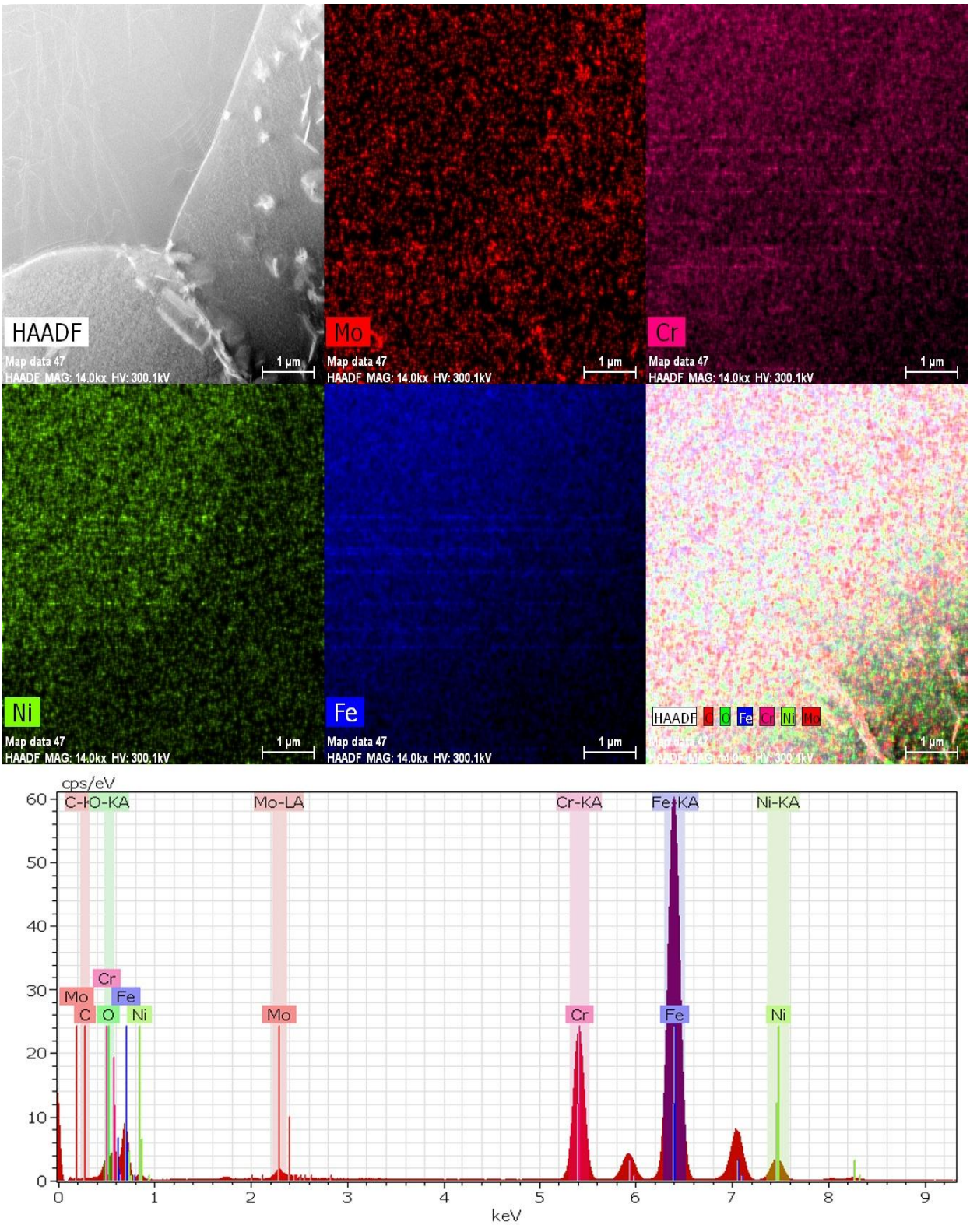

Figure 4.24 Elemental mapping and spectra analysis result of 100 hours re-aged sample

4.5 Effect of heat treatment on the mechanical properties

4.5.1 Microhardness

The micro-Vickers hardness (MVH) indentations were made on the ferrite and austenite phases as shown in Figure 4.25. The variation of MVH with respect to reversion heat treatment time is shown in Figure 4.26. The table 4.3 shows the obtained VHN values for all heat treated conditions. For the austenite phase, the change in micro-Vickers hardness after ageing was insignificant, whereas for the ferritic phase, the increase in hardness was quite significant. This indicates that embrittlement occurred only in ferritic phase and the austenitic phase remained ductile during the ageing process. There was a reduction in the micro-hardness values of the 60 minutes RHT samples because the Fe-rich alpha and Cr-rich alpha prime precipitate formed by the spinodal decomposition during ageing was dissolved when the embrittled samples were reversion treated. Sample reversion heat treated for 60 minutes showed maximum restorative effectiveness of 94.73%. When the RHT time was increased, the micro-hardness of the ferrite phase also increased with the RHT time. This is because of the formation of intermetallic phases such as R-phase and the secondary austenite.

However, the re-aging behaviors were compared with the initial aging behaviors. The initial microhardness values of the [60 minutes RHT + 100 hours re-aged] specimens were slightly higher than those of the [Solutionized + 100 hours aged] specimen, because of the precipitation of Mo-rich particles during the reversion heat treatment as explained in the previous section. However, the rates of re-embrittlement of the recovered samples were similar to those of the initial aging embrittlement.

Our results are somewhat consistent with the observation reported in several literatures. For example, Newell (1946) and Blackburn and Nutting (1964) reported that the 475 ^{0} C embrittlement in ferritic stainless steels may be alleviated by heating the embrittled alloys to the temperature of 550 ^{0} C or higher. Chung H M and Leax TR (1990) also reported that the hardness and toughness of the aged CF8 and CF8M were recovered to the level of the un-aged material after the R-HT at 550 ^{0} C for 60 minutes.

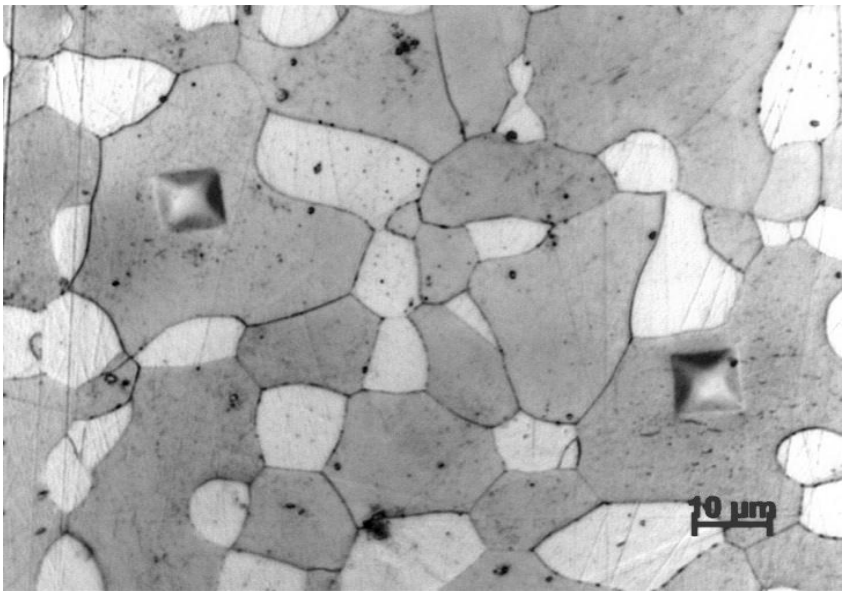

Figure 4.25 Diamond shaped indentations formed on ferrite phase of the 1000hrs aged sample.

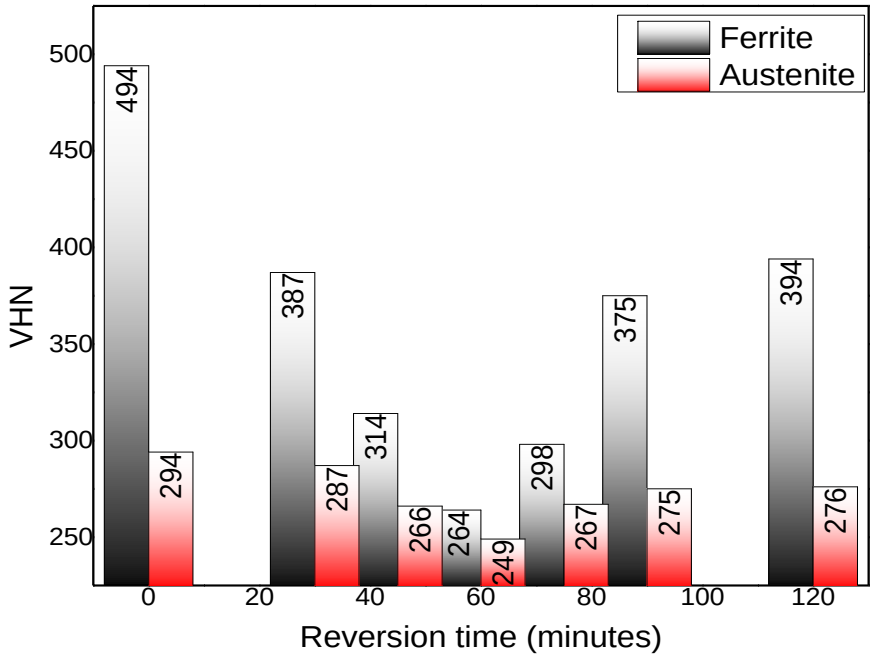

Figure 4.26 Variations in micro-hardness values of ferrite and austenite phases with the reversion heat treatment time.

Table 4.3 Vickers microhardness values for different heat treatment condition.

Heat treatment condition	Austenite (VHN)				Ferrite (VHN)			
	Min.	Max.	Avg.	SD	Min.	Max.	Avg.	SD
SOLUTIONISED	229	246	237	15.8	244	262	254	20.6
100 hours aged	288	303	297	4.3	398	444	433	21.3
1000 hours aged	278	325	315	16.8	434	465	444	18.5
15 minutes RHT	288	299	298	5.4	387	410	404	9.3
30 minutes RHT	288	310	306	6.4	377	398	387	10.4
45 minutes RHT	258	277	266	10.8	303	329	314	19.4
60 minutes RHT	220	259	249	14.4	255	268	264	11.6
75 minutes RHT	254	273	267	11.8	289	314	298	13.7
90 minutes RHT	291	306	295	9.5	368	287	375	12.3
120minutes RHT	318	340	329	18.8	390	405	394	9.8
100 hours re-aged	298	316	308	9.6	467	488	475	11.5

4.5.2 Impact behavior

The impact strength of the solutionized sample is very high (290J) because the sample in this heat treated condition very soft and ductile in nature.

Figure 4.27 shows the variation of room temperature impact strength with ageing time. The sigmoidal curve was obtained when the change in impact values was plotted against ageing time. The impact strength of 6J was obtained for samples aged at 90, 100, 250, 500 and 1000 hours. Hence we can say that embrittlement reaches saturation at 90 minutes.

Figure 4.28 shows the fracture surface of the 1000 hours aged impact sample. The fractured surface shows that it was predominantly brittle mode of fracture with the cleavage facets in most regions as well as a few sheared regions. The cleavage facets are the embrittled ferrite grains while the sheared grains were those of austenite. Under impact loading in aged condition the plastic deformation is severely constrained in the austenitic phase by the surrounding ferrite since plastic deformation hardly occurs in the ferrite phase. When the applied load reaches break strength of ferrite, cracks initiates in ferrite and then quickly propagate through the ferrite grains, this propagation is hindered by austenite and ferrite phase boundaries which results in the stress concentration. When the loading is further increased, the shear stress at the crack exerts pressure on the austenite phase and tears them off as shown in the Figure 4.28.

The impact strength of the RHTd samples for different durations was evaluated and the impact values are given in the table 4.4. The impact strength of the 15 minutes and 30 minutes RHTd sample was higher than that of the embritteled sample as the demodulation of spinodal microstructure initiated. But, the impact strength of 60 minutes RHTd sample was almost equal to that of the solutionized state which indicated complete dissolution of spinodal microstructure in the ferrite matrix. While the impact strength was again decreasing with increasing RHT time (90 and 120 minutes) because of the precipitation of R-phase and secondary austenite in ferrite phase which in turn embrittled the ferritic phase.

Since the embrittlement rate is highest at 475 ºC (Sahu.J.K et al. 2009), this temperature was again chosen for to evaluate the re-ageing behavior of the 60 minutes reversion heat treated samples in our investigation. In order to evaluate the aging properties the samples were raged for 25, 50, 70, 80, 90 and 100 hours. The Figure 4.29 shows the variation of room temperature impact values with ageing time. Sigmoid curve, which is similar to that obtained during aging was obtained when changes in impact values were plotted against ageing time. Impact strength of 6J was obtained for samples aged at 100 hours. Hence, from the results we found that the time taken for the re-embrittlement was also 100 hours and also we can say that samples are completely embrittled when they are re-aged at 475 ºC for 100 hours.

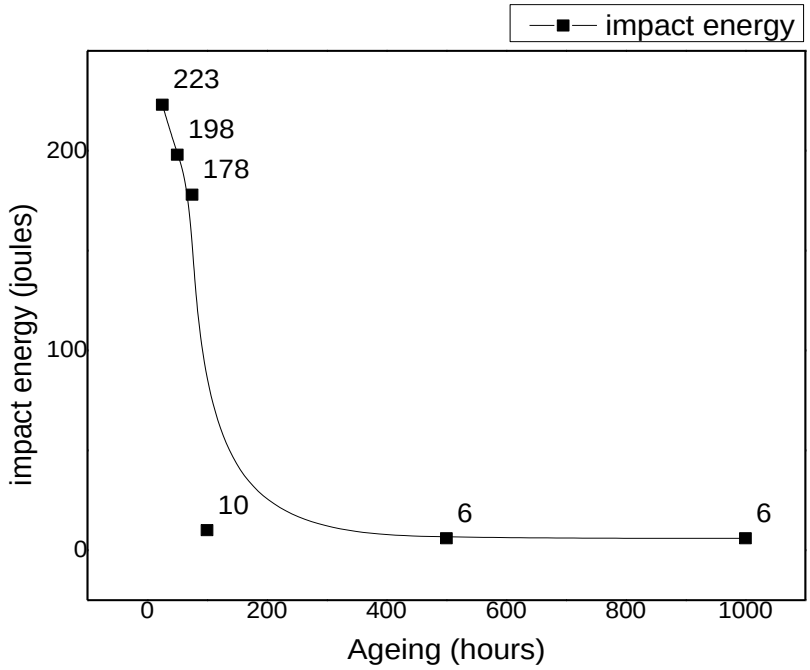

Figure 4.27 Variation of the impact energy with ageing time.

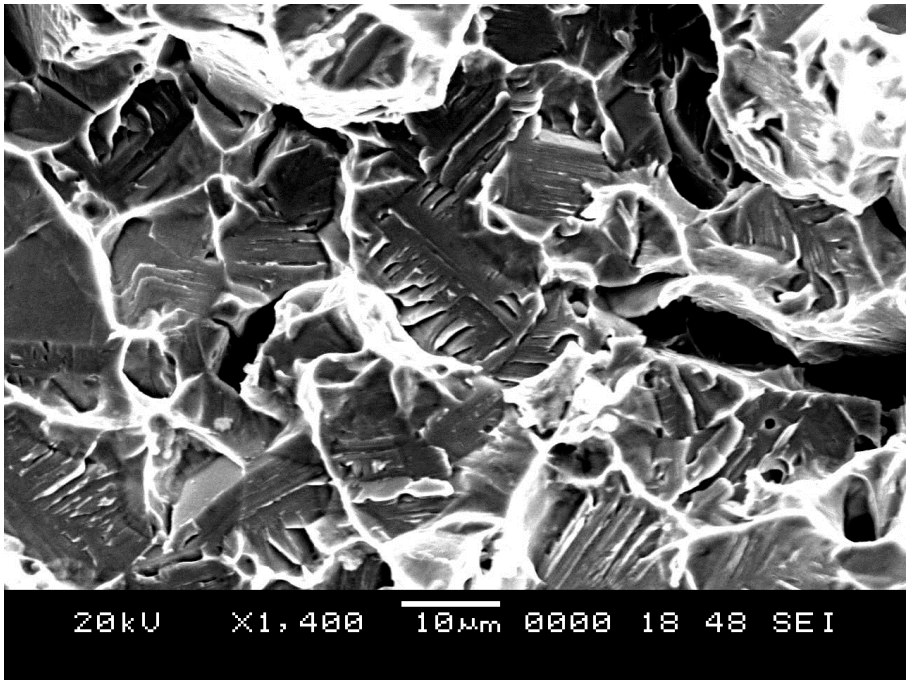

Figure 4.28 SEM image of the fractured surface of 1000 hours aged impact sample.

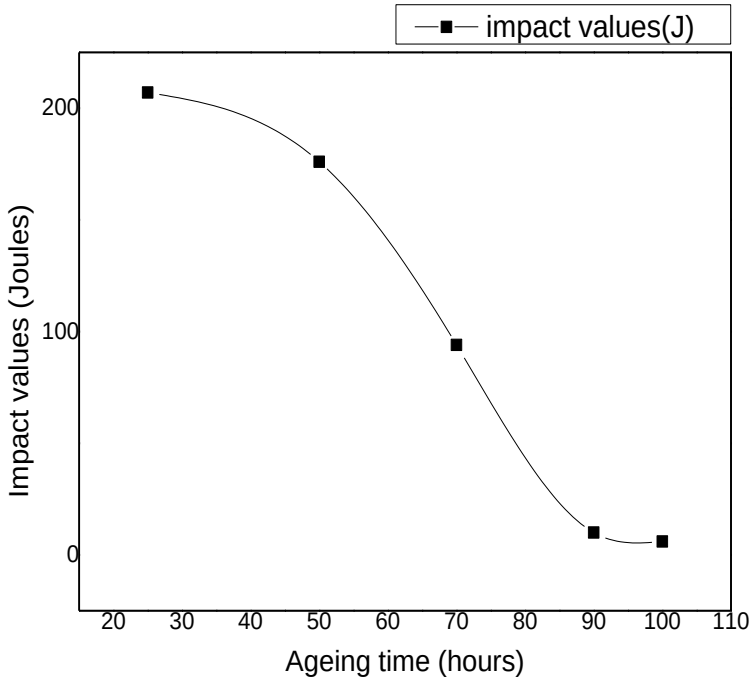

Figure 4.29 Variations of impact energy with re-ageing time.

Table 4.4 Impact energy with varying reversion heat treatment time.

Reversion heat treatment time (minutes)	**Impact energy (J)**
15	140
30	190
60	270
90	200
120	190

Tensile behavior

The measured values of ultimate tensile strength and % elongation for aged conditions are given in Table 4.5. The ultimate tensile strength of 1000 hours aged sample was increased by 35% and accompanied by the 57% loss in the ductility. The variation in tensile properties with the ageing time is as shown in Figure 4.30. After ageing at 475 ^{0} C, the material exhibited a drastic increase in strength and decrease in ductility due to the embrittlement associated with the formation of α and α′ precipitates in the ferrite phase at this temperature. The tensile strength is increased because of α and α-prime precipitates interfere the motion of dislocation.

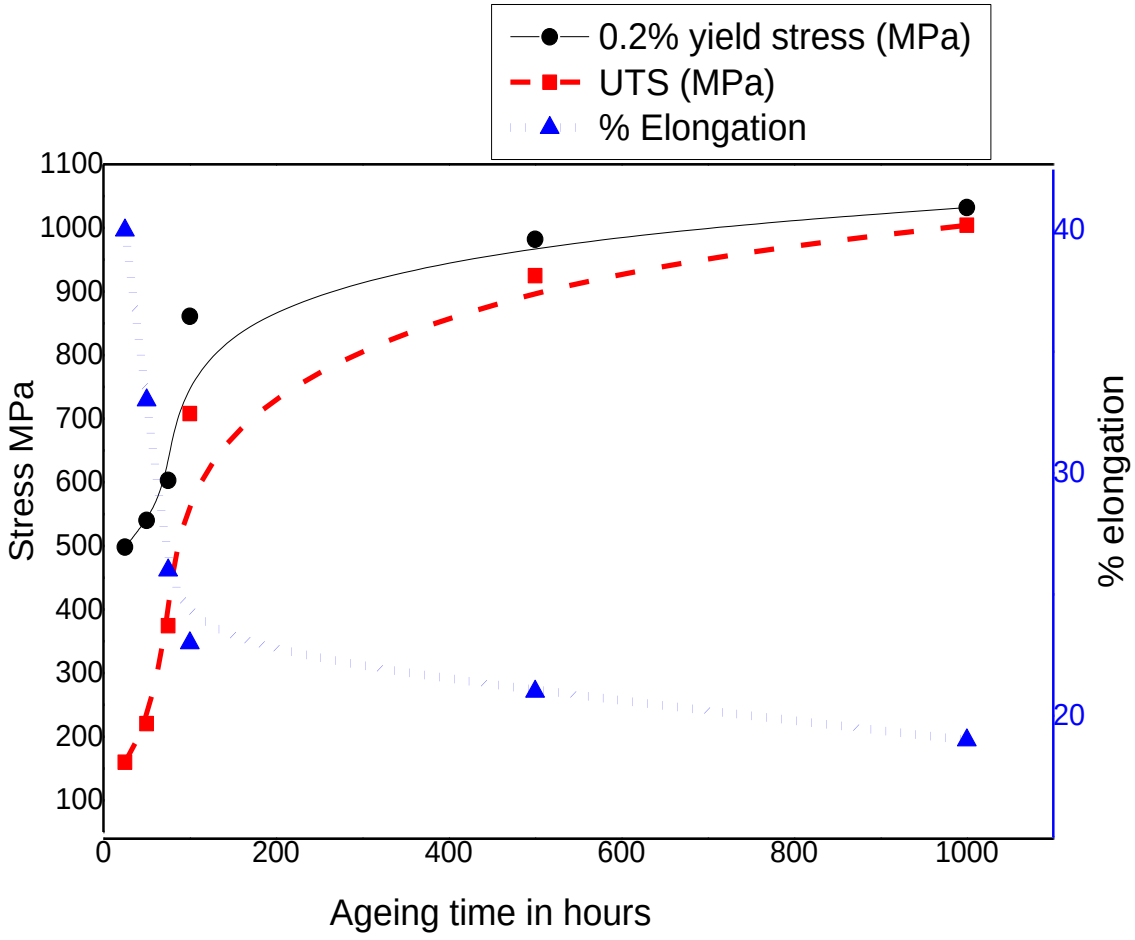

Figure 4.30 Variation of tensile properties with ageing time.

Table 4.5 Tensile properties of embrittled S2205 DSS for different duration.

Heat treatment	0.2% yield stress	UTS (MPa)	% elongation
Ageing-25 hours	498	797	40
Ageing-50 hours	540	823	33
Ageing-75 hours	603	889	26
Ageing-100 hours	861	1032	23
Ageing-500 hours	982	1125	21
Ageing-1000 hours	1032	1159	19

The Figure 4.31 shows engineering stress-strain curves for the specimens for all heat treatment conditions. Table 4.6 shows the tensile properties of the material such as tensile strength, yield strength and percentage elongation for Reversion heat treated conditions. The variation of tensile strength, yield strength and percentage elongation with duration of reversion treatment is shown in the Figure 4.32.

On subjecting the embrittled specimens to reversion heat treatment at 550 ^{0} C, it was observed that the strength dropped while the ductility increased, owing to the dissolution of α and α′ precipitates into the ferrite matrix. After 30 and 45 minutes of reversion treatment, the decrease in strength was marginal, whereas, the increase in ductility was significant. The material exhibited a further drop in strength and increase in ductility for 60 minutes of reversion, after which, both the strength and ductility remained more or less constant. The reversion treatment, however, was unable to completely restore the properties of the material back to those corresponding to the un-aged or solution annealed condition. The yield strength was more sensitive to reversion heat treatment, varying much more than the tensile strength with respect to duration of reversion heat treatments. It is because of the further

embrittlement that occurred simultaneously with the dissolution of α and α′ precipitates, during reversion heat treatment and, as a result, the mechanical properties were not fully recovered. The temperature range of the reversion heat treatment is favorable for the formation of a Mo-rich precipitate called R-phase, which is known to be an embrittling phase (Hwang et al. 2014), and in fact, previous investigators (Jang et al. 2014), had found unidentified Mo-rich precipitates in super-duplex stainless steels reversion treated for 30 minutes at the same temperature as in the current investigation. Another possible reason for this behavior could be residual inhomogeneties in the ferrite grains as a result of the Cr and Mo atoms that were part of the precipitates might have been redistributed. This in turn may have resulted in the formation of dislocation substructures in the ferrite grains during deformation. From the results it was also very clear that after 75 minutes reversion treatment the strength was again increasing and the ductility was decreasing because of the embrittlement caused by the R-phase and secondary austenite which were quantitatively seen in SEM and TEM micrograph for 120 minutes reversion heat treated sample.

The measured values of ultimate tensile strength and % elongation for re-aged conditions are given in Table 4.7. The 100 hours re-aged sample had maximum ultimate tensile strength. The variation tensile properties with ageing time are shown in Figure 4.32 and 4.33. From the measured values of tensile properties it is clear that strength is increased and ductility has decreased with ageing time. Tensile strength is again increased because of the spinodal decomposition in which, the precipitates interferes the motion of dislocation and ductility is decreased because of the movement of interstitial atoms which diffuse the dislocation obstacles in the solid solution.

Table 4.6 Tensile properties of Reversion heat treated condition.

Reversion Heat Treatment (minutes)	0.2% YS(MPa)	UTS (MPa)	Ductility (%)
30	727	932	31
45	606	839	38
60	528	746	39
75	552	780	33
90	604	790	34
120	629	844	34

Table 4.7 Tensile properties of embrittled S2205 DSS for different duration

Heat treatment (Re-aging)	0.2% yield stress (MPa)	UTS (MPa)	% elongation
25 hours	514	787	28
50 hours	521	813	27
75 hours	632	873	26
90 hours	841	974	24
100 hours	861	995	23

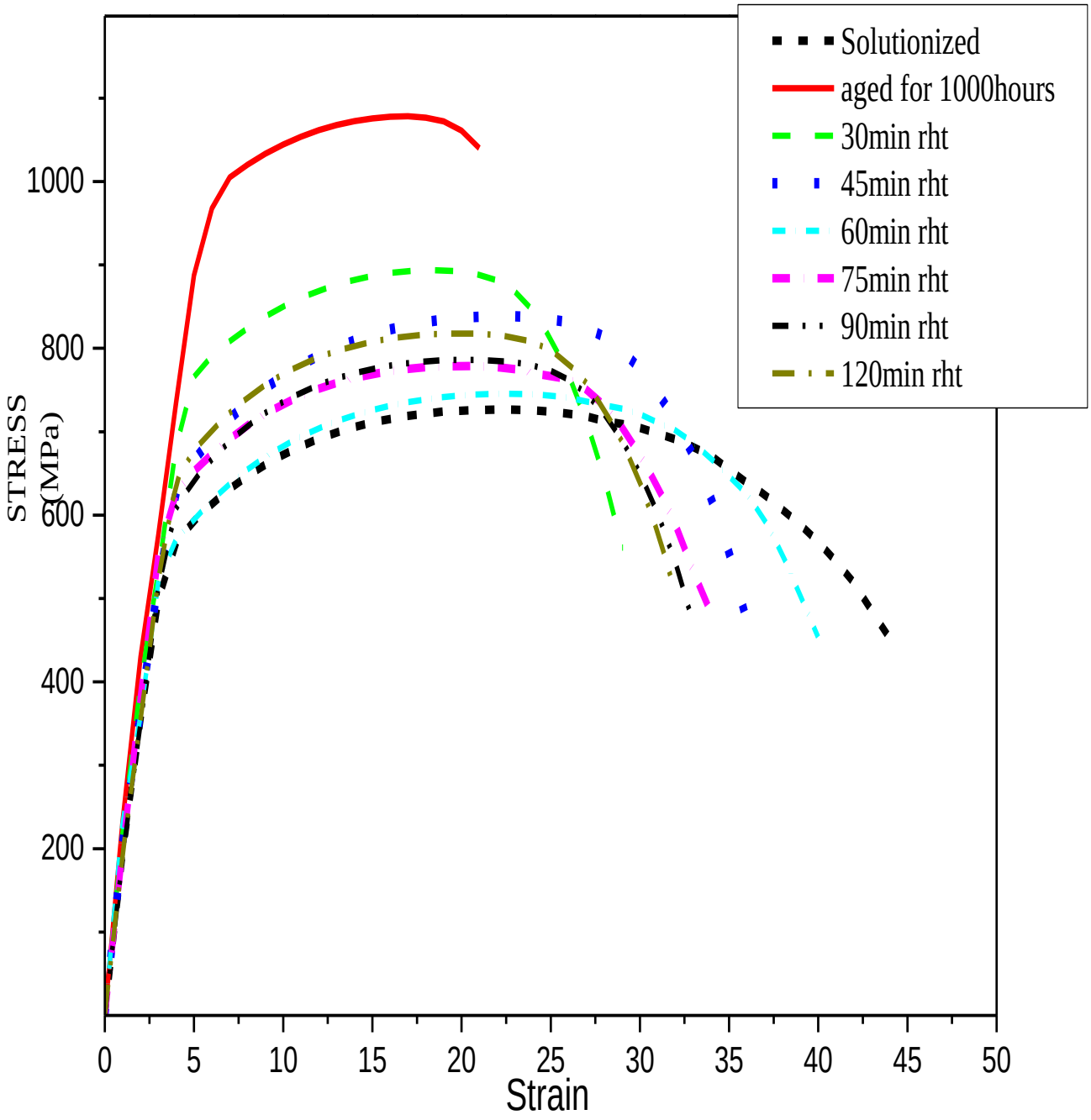

Figure 4.31 Engineering Stress-Strain plots for UNS S2205 under each heat treated condition.

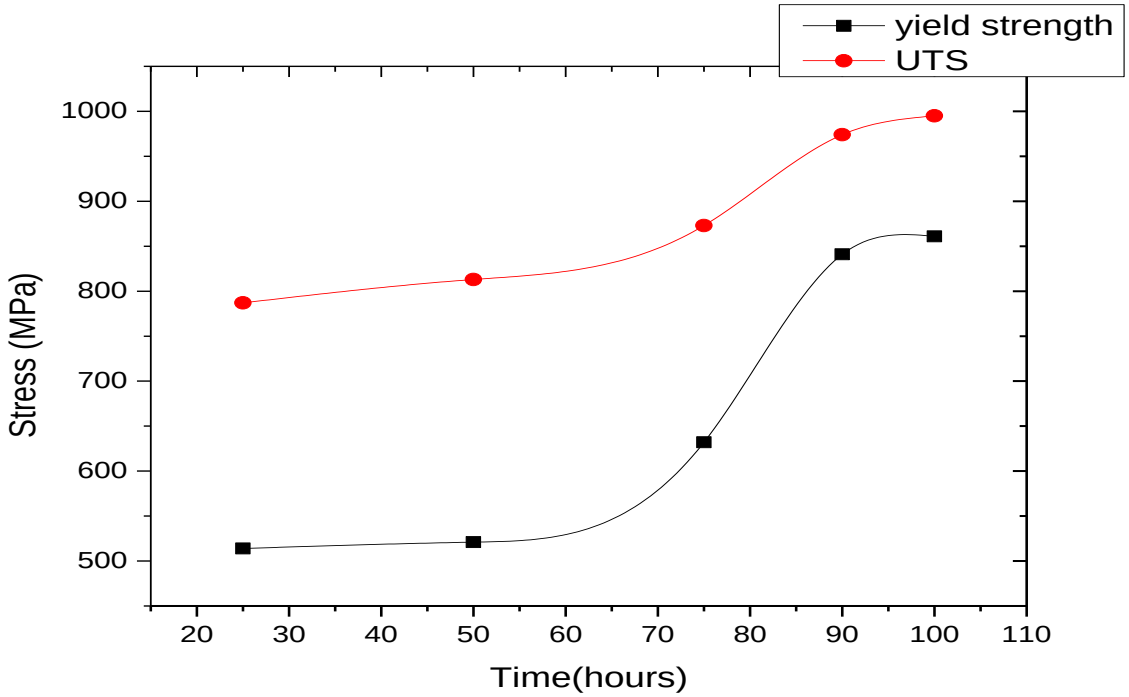

Figure 4.32 Variations of yield strength and UTS with re-ageing time

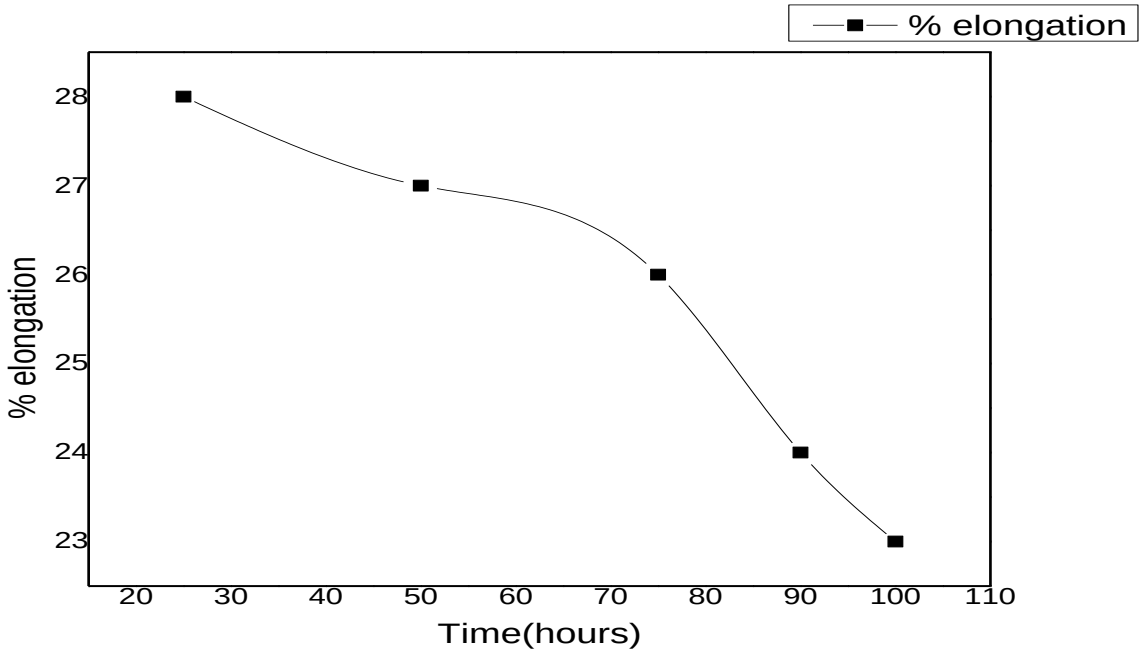

Figure 4.33 Variations of ductility with re-ageing time

Effect of grain size on the tensile strength

The table 4.8 depicts the volume fraction and grain size measurements for various heat treatment conditions. The volume fraction of the ferritic phase was increased during aging process because of the migration of the Cr and Mo atoms from the austenitic phase to ferritic phase which inturn also lead to the increased ferrite grain size. Since ferritic phase was the hardening phase during aging the increase in volume fraction and the ferritic grain size lead to the increase in the tensile and fatigue strength of the material.

The grain size and the volume fraction of the RHT-30 and RHT-60 had decreased because of the dissolution of Cr and Mo rich precipitates and these atoms during dissolution might have been redistributed. This inturn lead to the decrease in the tensile and fatigue strength of the material. After 60min RHT the grain size and the volume fraction was found to increase again which inturn lead to the increase in the tensile strength. The grain size and volume fraction of the reaged sample was found to be more than the aged sample which inturn reflected the increased tensile and fatigue strength

Table 4. 8 Grain size and volume fraction for different heat treatment condition

Heat treatment condition	Austenitic Phase grain size(μm)			Ferritic Phase grain size (μm)		
	Minimum value	Maximum value	Volume fraction	Minimum value	Maximum value	Volume fraction
Annealed	9	85	0.46	30	85	0.54
Aged	18	150	0.356	100	800	0.644
RHT-15	13	200	-	80	316	-
RHT-30	25	181	0.454	70	350	0.546
RHT-60	60	110	0.488	35	213	0.512
RHT-90	20	194	0.409	35	297	0.591
RHT-120	80	215	0.453	35	357	0.547
Re-aged	22	215	0.376	90	750	0.624

Strain hardening behaviour

The stress-strain diagrams obtained during the tensile tests were used to study the strain hardening behavior after different durations of reversion. For this purpose it was assumed that the flow curve could be expressed by the Holloman relationship (Holloman 1945);

$$\sigma = K\varepsilon^{n} \text{ ----- } (4.1)$$

Where, σ is the true stress, ε is the true plastic strain and K is the strength coefficient. According to this, a double log plot of true stress against true strain should result in a straight line with a slope of "n". In the present investigation, "n" values for reversion heat treatments of different durations were determined by considering the corresponding stress-strain diagrams shown in Figure 4.31. The points from the stress up to the ultimate tensile stress were considered for plotting the of true stress-strain diagram on a logarithmic scale as shown in Figure 4.34. These data points followed a linear relationship in each case confirming the validity of the Holloman relationship. The strain hardening exponent 'n' was calculated for each case by measuring the slope of the straight line. The variation of strain hardening exponent with different heat treatment is as shown in Figure 4.35. The value of 'n' was least for aged sample and highest for solutionized and 60 minutes RHT d sample.

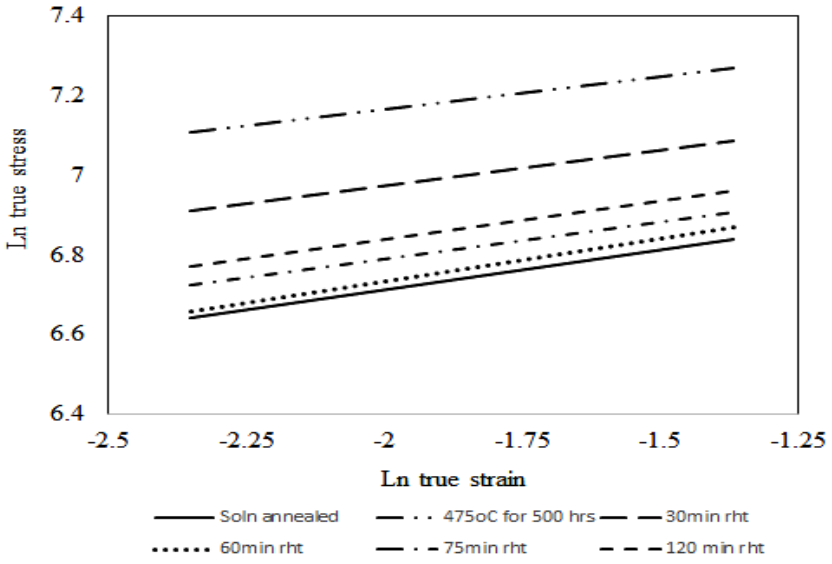

Figure 4.34 Plot of ln (true stress) versus ln (true strain) for aged and reversion treated specimens

The value of ‘n’ for 60 minutes RHT and solutionized sample was almost same which indicated that the recovery was almost equal to that of solutionized state.

It is believed that the ductility of a material increases with the increase in ‘n’ value and so does the resistance to neck formation. This co-relation can be observed by comparing the variation in ‘n’ values with engineering stress-strain curves of the specimens in the current investigation. The ductility increases with reversion time upto 60 minutes and so does the ‘n’ value. After 60 minutes the ‘n’ value decreases while the ductility decreases upto 75 minutes and from there upto 120 minutes remains more or less constant. It is understood that, a change in ‘n’ value signifies a change in the deformation behavior. At first, the dissolution of the alpha prime precipitates which acted as dislocation pinning sites due to the reversion heat treatment, resulted in the free movement of dislocations leading to an increased ductility and reduction in strength. However the formation of R-phase, secondary austenite or dislocation substructures during RHT has affected the deformation behavior and caused the value of ‘n’ to drop after 60 minutes RHT.

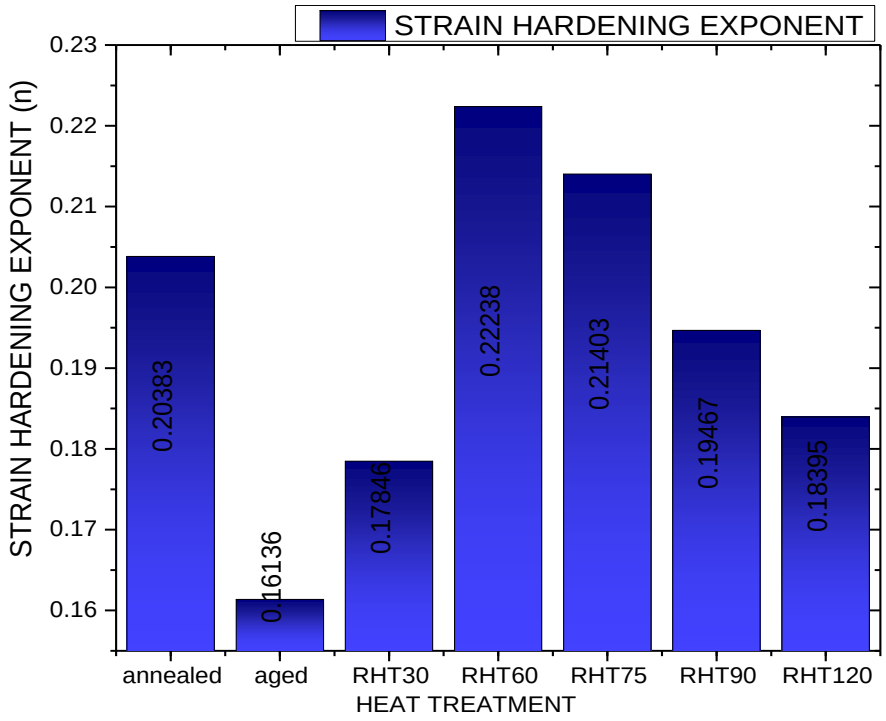

Figure 4.35 Variations of strain hardening exponent ‘n’ values for different heat treatment condition

4.5.3 Fractography

The fracture surfaces of the tensile tested specimens of all heat treatment conditions were observed under a scanning electron microscope and images were recorded. In the solutionized condition (Figure 4.36), the fracture was fully ductile with dimples throughout the fracture surface. The aged specimen (Figure 4.37) revealed a predominantly brittle fracture surface with cleavage facets in most regions as well as a few sheared regions. The cleavage facets correspond to the ferrite grains, which were embrittled by α′ precipitation during the ageing treatment (Wang et al. 2010). The sheared grains correspond to those of austenite, since the austenite remains ductile even after ageing (Yang et al. 2009). The cleavage cracks initiate at the α′ precipitates and then propagate across the ferrite network. The ductile fracture forms at the weak phase boundaries and propagates through the austenite phase.

After 30 minutes of reversion treatment, a fully ductile fracture surface with well defined dimples was observed (Figure 4.38). This indicates that the dissolution of α′ begins at a very early stage of reversion, and, that although the reduction in strength is marginal, the volume fraction of α′ has reduced to an extent that is insufficient to have a serious effect on the ductility of the material. But in the 60 minutes reversion heat treated sample (Figure 4.39), we can see the complete ductile fracture with even larger dimples than the 30 minutes reversion heat treated sample. The nature of the fracture surface for the 120 minutes reversion heat treated specimen was brittle in nature as we can see the cleavages in the ferrite grain, which is due to the presence of R-phase (Figure 4.40).

The fractured surface of re-aged samples is as seen in the Figure 4.41. It has undergone brittle fracture. The failure surface is essentially covered with transgranular brittle grains containing crystallographic rivers and numerous secondary cracks. The fracture morphology changes when the crack crosses ferritic phase to austenitic phase.

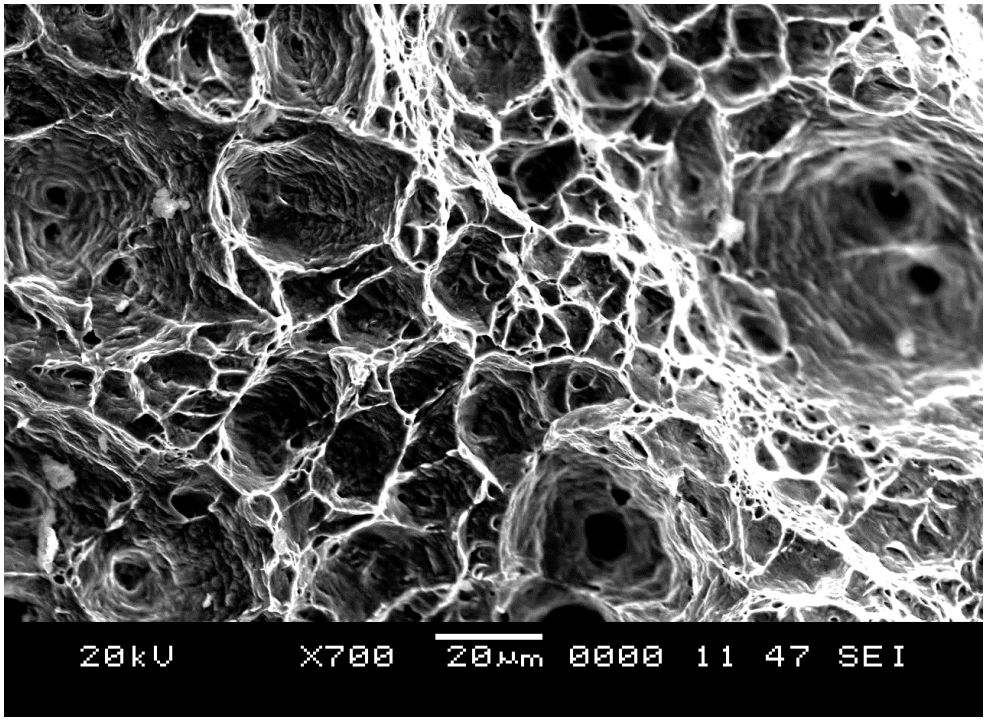

Figure 4.36 Fractograph of the solutionized tensile sample.

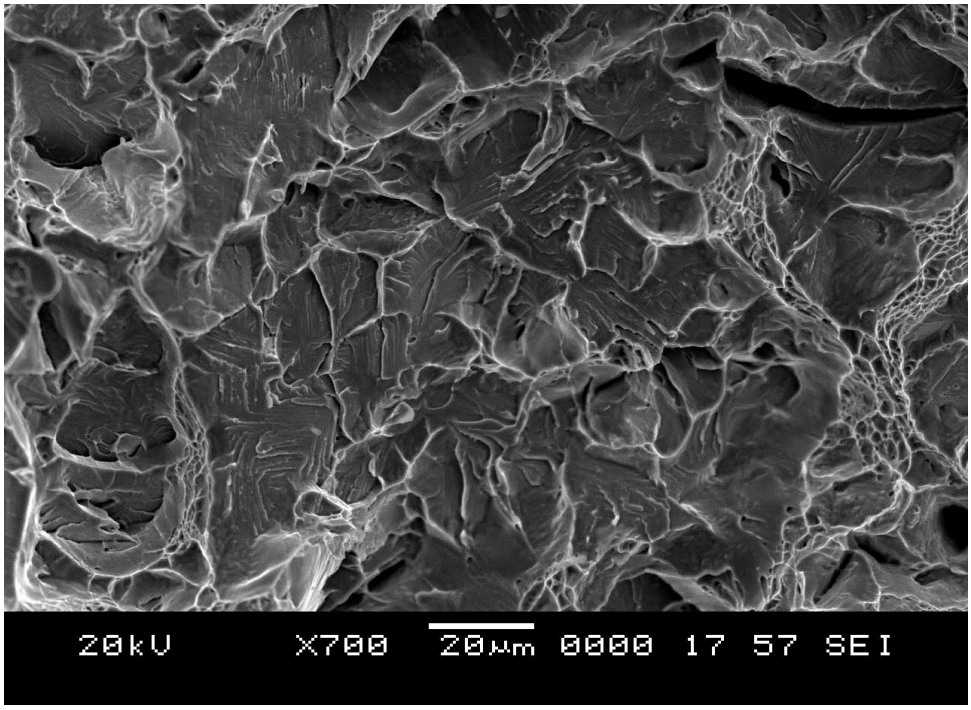

Figure 4.37 Fractograph of the 1000 hours aged tensile sample.

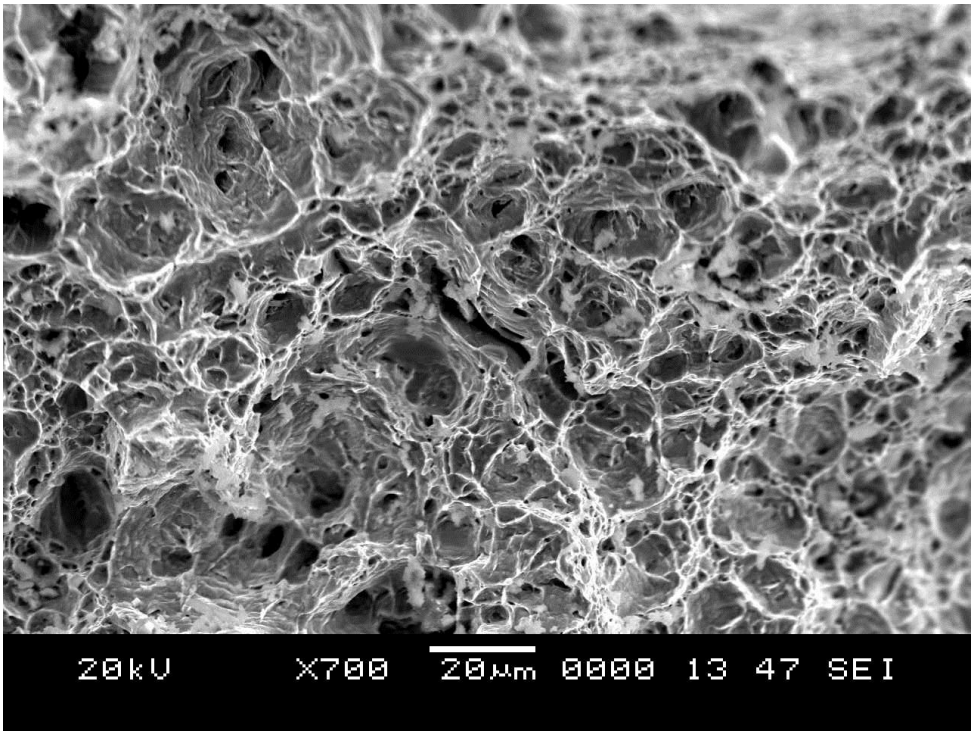

Figure 4.38 Fractograph of the 30 minutes RHT tensile specimen.

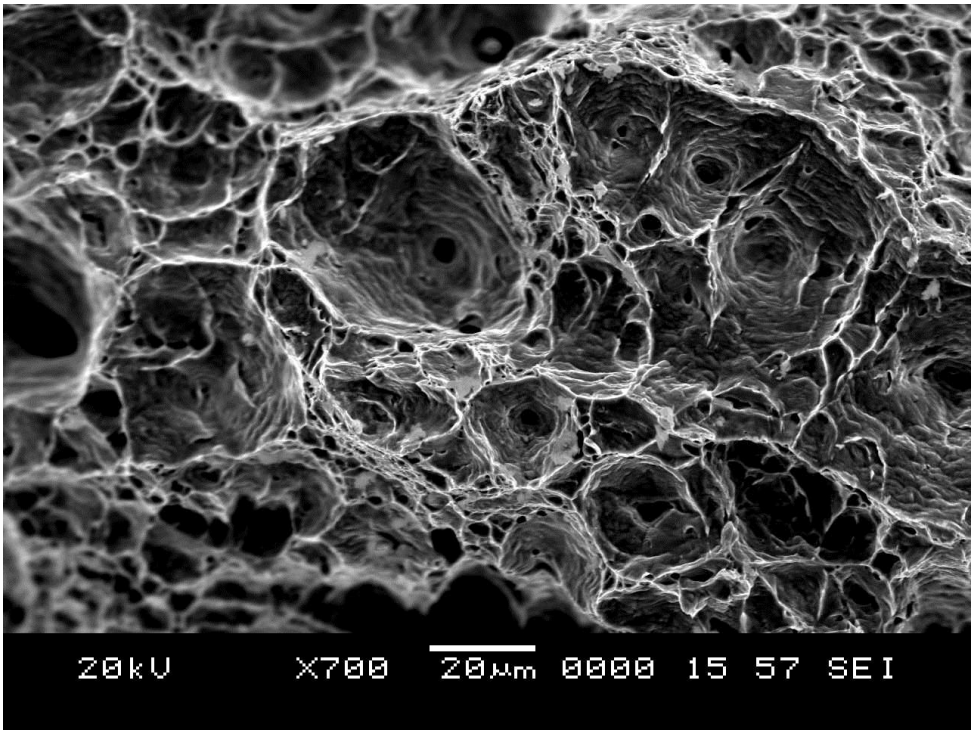

Figure 4.39 Fractograph of the 60 minutes RHT tensile specimen.

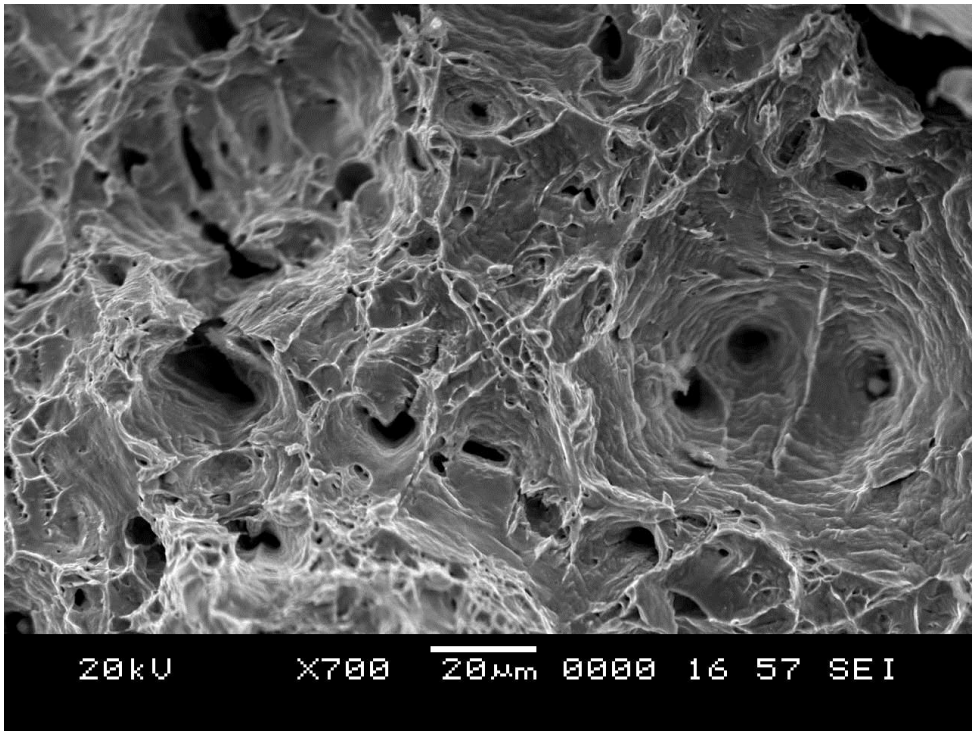

Figure 4.40 Fractograph of the 120 minutes RHT tensile specimen.

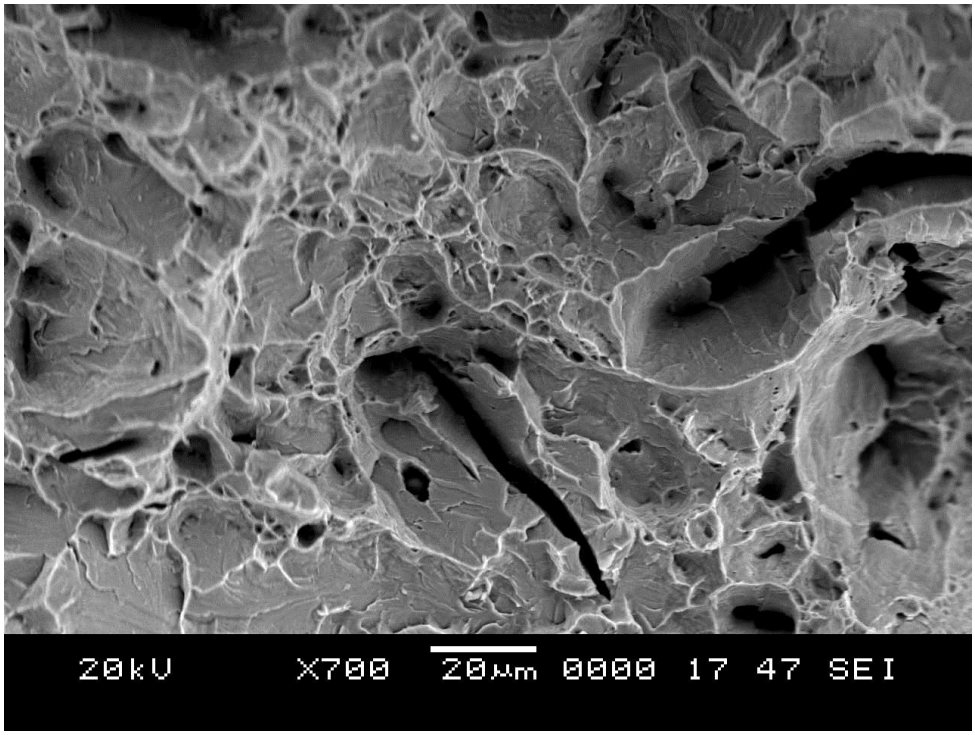

Figure 4.41 Fractograph of the 100 hours re-aged tensile sample.

Restorative effectiveness

For evaluating this restoration phenomenon Mateo.A et al. (1996) defined the parameter named as "Restorative effectiveness" which is given by the equations below

$$\%\text{R. E of yield stress} = \frac{(\text{Aged yield stress} - \text{Restored yield stress})}{(\text{Aged yield stress} - \text{Annealed yield stress})}$$

$$\%\text{R. E of UTS} = \frac{(\text{Aged UTS} - \text{Restored UTS})}{(\text{Aged UTS} - \text{Annealed UTS})}$$

$$\%\text{R. E of ductility} = \frac{(\text{Aged ductility} - \text{Restored ductility})}{(\text{Aged ductility} - \text{Annealed ductility})}$$

$$\%\text{R. E of VHN} = \frac{(\text{Aged VHN} - \text{Restored VHN})}{(\text{Aged VHN} - \text{Annealedyield VHN})}$$

Table 4.8 gives the Restorative effectiveness values for different RHT time and the Figure 4.42 shows the variation of restorative effectiveness of mechanical properties with RHT time. At 60 minutes RHT 87.3% yield strength, 95.3% UTS and 86.4% ductility were restored. From the reversion heat treatment, however, it was not able to recover the mechanical properties completely. This is because with the dissolution of alpha prime precipitate in the ferrite phase further embrittlement was initiated at 60min of reversion heated samples. It is likely that secondary austenite or R phase was initiated when reversion heat treated at 550 ºC for 60 minutes but it was not evident in the microstructure. From the results it was very clear that after 75 minutes reversion treatment the strength was again increasing and the ductility was decreasing and the R-phase and secondary austenite were quantitatively seen in SEM and TEM micrograph for 120 minutes reversion heat treated sample.

Another possible reason for not achieving 100% restoration effectiveness might be because of the residual inhomogeneties which arise in the ferrite phase due to Cr and Mo atoms which are part of precipitates not being redistributed. This in turn may have resulted in the formation of dislocation substructures in the ferrite grains during deformation.

Table 4.9 Mechanical properties restorative effectiveness with RHT time.

Reversion Heat Treatment (minutes)	%RE (0.2% YS)	%RE (UTS)	%RE (Ductility)	%RE (α-VHN)
30	52	52.4	50	30
45	73.4	73.9	81	68.4
60	87.3	95.3	86.4	94.73
75	83	87.5	59	76.84
90	73.9	85.2	63.6	36.31
120	69.4	72.8	63.6	26.31

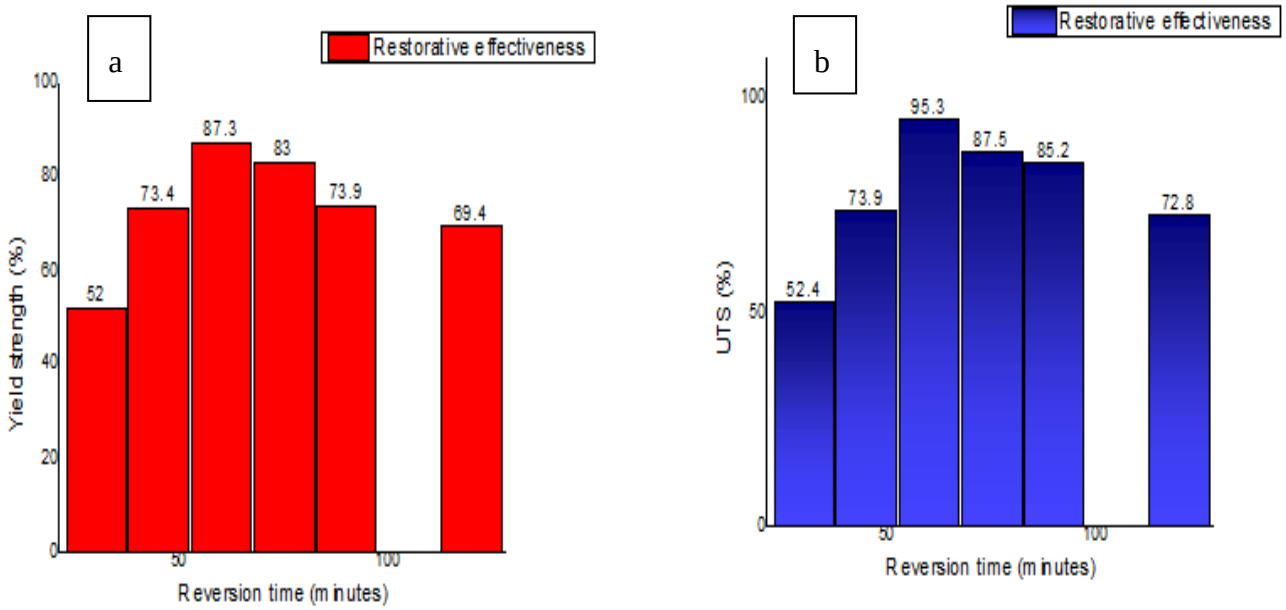

Figure 4.42 (a) Variation of restorative effectiveness of Yield strength with RHT time and (b) Variation of restorative effectiveness of Yield strength with RHT time.

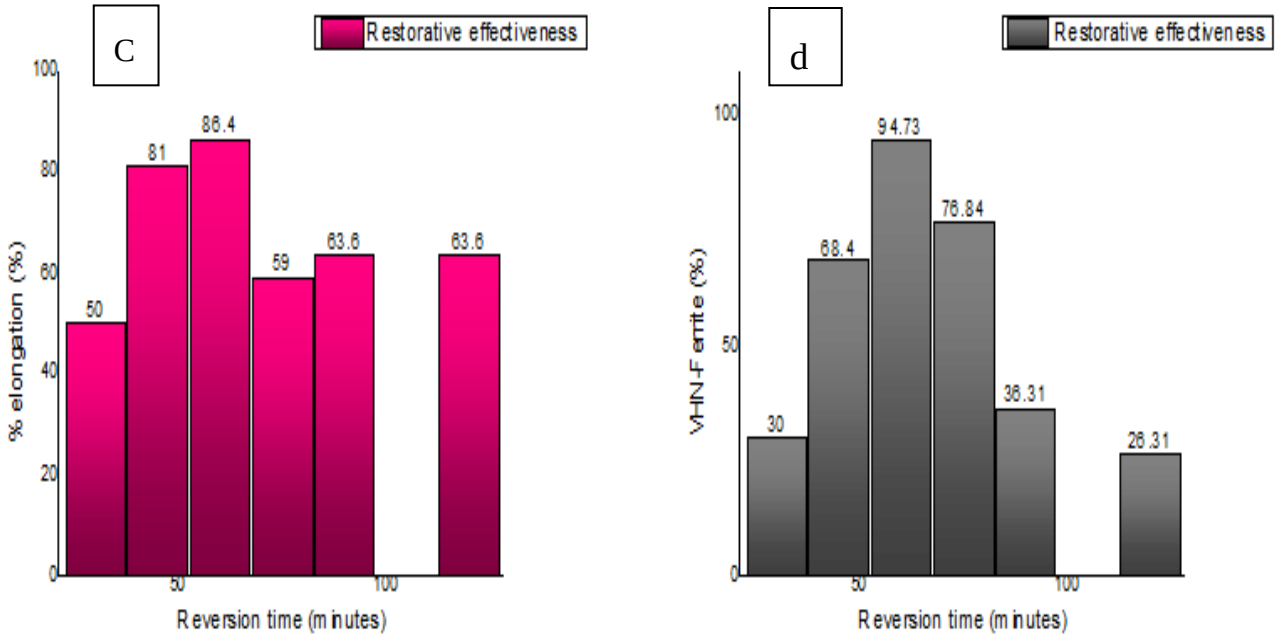

Figure 4.42 (c) Variation of restorative effectiveness of % elongation with RHT time and (d) Variation of restorative effectiveness of Yield strength with RHT time.

4.5.4 Effect of heat treatment on the high cycle fatigue properties

The S-N curves for the annealed, aged, 60-RHT and Re-aged heat treated DSS are as depicted in the Figure 4.43. The high cycle fatigue strength for the aged and re-aged condition i.e. in the embrittled state is higher than the annealed and RHT heat treated condition. Aged and re-aged conditions had an almost similar fatigue limit and HCF strength, while the S-N curve for annealed and RHT conditions was also similar, but the fatigue limit was higher than that of the annealed condition because of the presence of the Mo-rich intermetallic phase in the ferritic phase. However the improvement of fatigue strength is not as remarkable as that observed for the tensile properties. Hence the fatigue sensitivity of different heat treated conditions is correctly correlated with the difference in the crack nucleation and propagation behavior within the HCF regime. For evaluating restorative effectiveness of the fatigue strength equation (1) was used and the restorative effectiveness for HCF was found to be about 82%. The fatigue behavior of the re-aged DSS was similar to the aged DSS samples.

$$\%\text{R. E of HCF} = \frac{(\text{Aged HCF} - \text{Restored HCF})}{(\text{Aged HCF} - \text{Annealed HCF})} \qquad \ldots\ldots\ldots\ldots\ldots\ldots\ldots\ldots(1)$$

Effect of Annealing and reversion heat treatment on the high cycle fatigue properties of DSS

The S-N curves for the annealed, aged, 60-RHT and Re-aged heat treated DSS are as depicted in the Figure 4.43. The high cycle fatigue strength for the aged and re-aged condition i.e. in the embrittled state is higher than the annealed and RHT heat treated condition because of the presence of alpha, alpha prime and some molybdenum rich chromium nitride precipitates in their ferrite matrix which resists the movement dislocations.

The fatigue behaviors of the aged/re-aged materials vary significantly from that of the annealed/RHTd materials, i.e., the fatigue resistance of the aged/re-aged materials are high when compared to that of annealed/RHTd materials. As shown in the Figure 4.44 initially slip bands were mainly found in the ferritic phase at higher stress regime because the strain-hardening rate of the austenite is lesser than that of the ferrite. But in annealed/RHTd condition hardness variation of austenite and ferritic phase is not high. Hence, under the stress level the strain hardening, in extent makes austenite a stronger phase, which is more resistant to plastic deformation under cyclic loading. Subsequently the ferritic phase also suffers from plastic deformation slightly more than the austenitic phase. Hence, in annealed/RHTd condition dislocation bundles or dislocation pile ups which are seen in the form of cell structures is seen in the ferrite phase as depicted in the Figure 4.45.

Interesting features were revealed when TEM analysis of dislocation structures was done. Planar arrangement of dislocation structure that is in the form of cell structure was observed as shown in the Figure 4.46. However, these dislocation structures are responsible for the localization of cyclic plastic strain into slip bands. Hence, in this condition slip band are formed first and acts as nucleation sites for micro cracks, in other words strain localization are the result of persistent slip bands nucleation in the hard matrix structure after large strain accumulations.

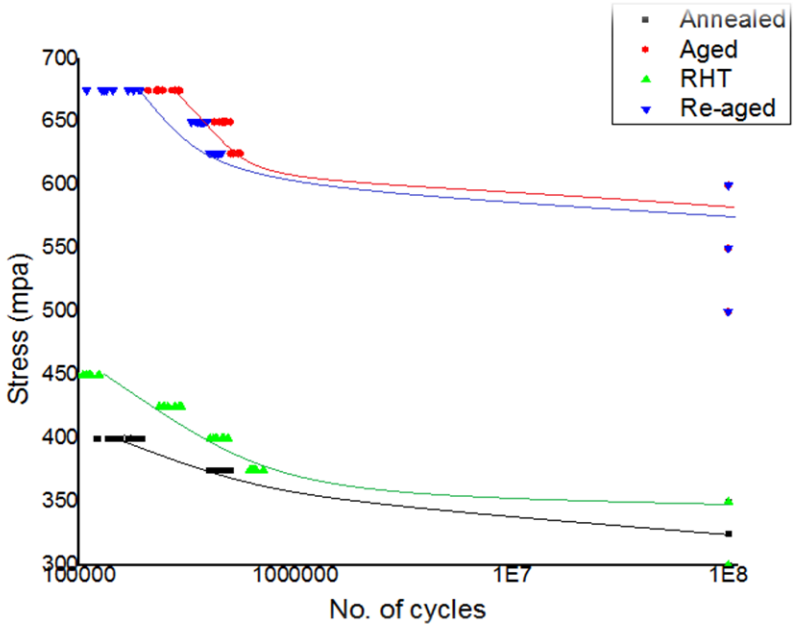

Figure 4.43 S-N curves for different heat treated condition

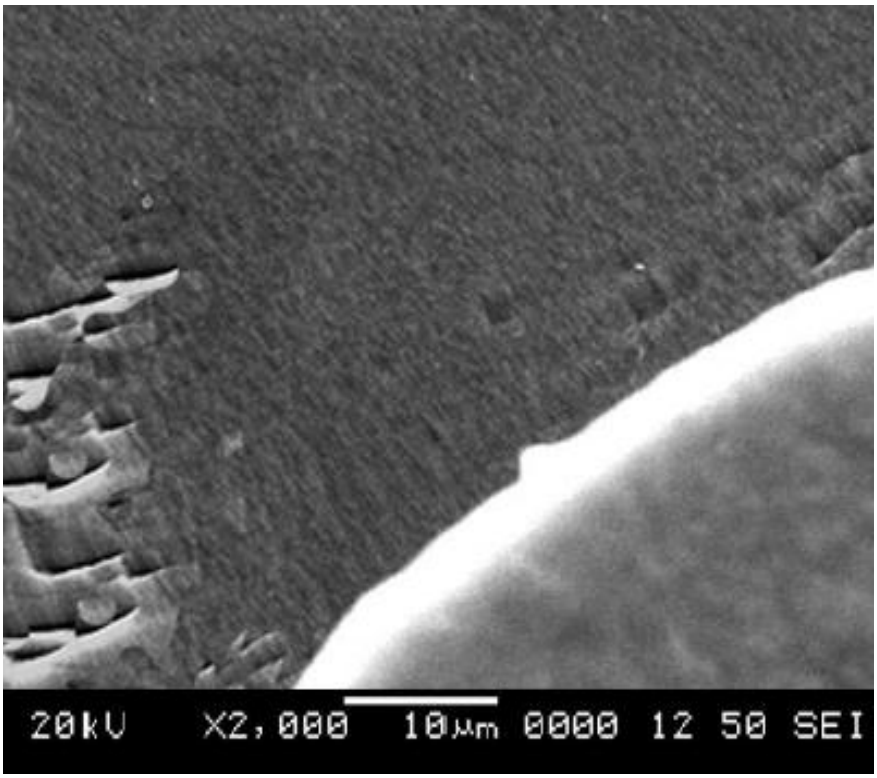

Figure 4. 44 SEM image of annealed sample stressed at 400 MPa showing slip bands in ferrite phase.

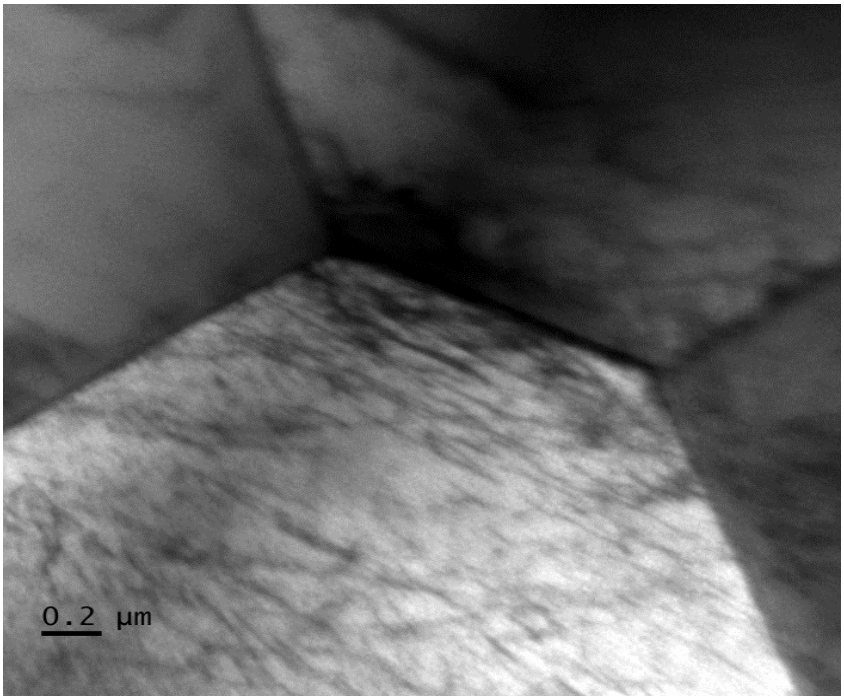

Figure 4. 45 TEM image of 60 minutes RHT sample stressed at 400 Mpa.

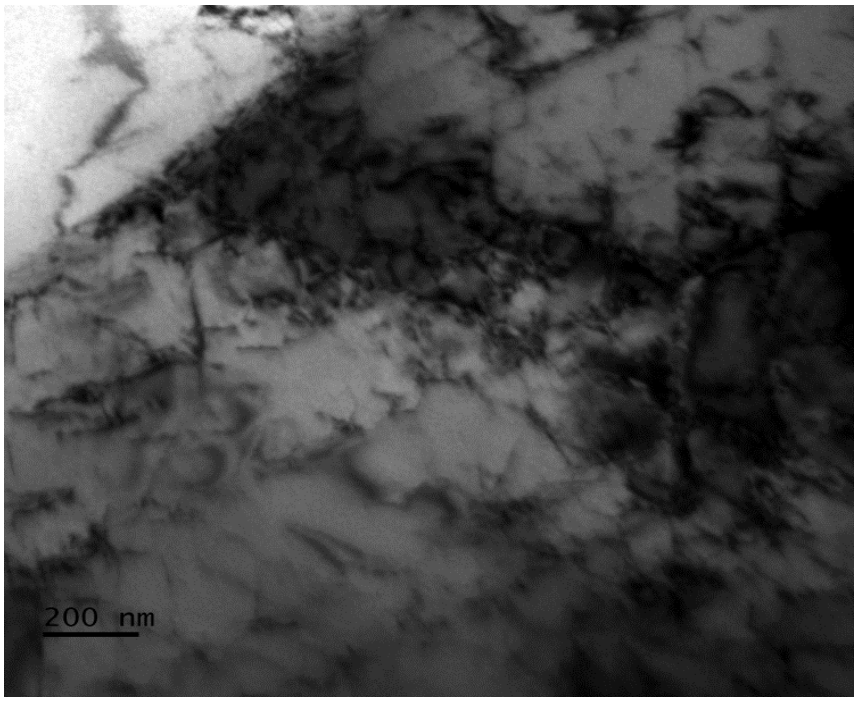

Figure 4. 46 TEM image of 60 minutes RHT sample stressed at 450 MPa showing dislocations in ferrite matrix

Effect of aging and re-aging on the high cycle fatigue properties of DSS

The 475 ^{0} C aging treatment results in an embrittlement of the ferritic phase. When this was detected for the first time in ferritic stainless steels the term embrittlement referred to as change from ductile to brittle failure (R.O. Williams and H.W. Paxton (1957). So this temperature is understood to express a detrimental effect to mechanical properties. This holds true for the mechanical behavior such as tensile and impact. However, under fatigue loading conditions the term embrittlement need not necessarily be detrimental. This is because a multitude of parameters defining the fatigue loading condition, such as stress/strain amplitude, load ratio, frequency, may interact differently with the microstructure that results from the aging treatment. Furthermore, the so-called embrittled microstructure may be beneficial for some aspects of fatigue features under some combination of cyclic load parameter

In this condition the one set of the annealed samples were aged at 475 ^{0} C for 1000 hours and another set of aged samples were 60 minutes reversion heat treated at 550 ^{0} C and then re-aged at 475 ^{0} C for 100 hours.

Aging and re-aging the samples at 475 ^{0} C for 100 hours lead to spinodal decomposition of ferrite matrix into iron rich (α) phase and chromium rich (α') phase. Due to this spinodal decomposition the micro cracks propagation developed in the ferrite phase is completely different from that of the annealed and reversion heat treated condition. The formation of the slip markings on the ferritic phase starts from the beginning of the cyclic loading and is a result of deformation by gliding and twinning. In the Figure 4.50, we can see the microstructure consisting of planar dislocations and several extended micro twins throughout the ferrite matrix. Array of micro twins is also seen because the unit dislocation is either dissociated or it has the asymmetric core structure which resists the screw dislocation free movement. Dislocations as seen in the Figure 4.48 are in the form of cell structure and this dislocation structure is responsible for the strain localization. Figure 4.47 is taken in the austenitic phase where deformation is more localized and this shows the dislocation arrangement corresponding to the localization of plastic strain leading to cell formation. The dislocations are piled-up in the Austenite-ferrite phase boundaries. The ferrite-ferrite or

ferrite-austenite phase boundaries are the preferred sites for micro-cracks which are located nearly perpendicular to the tensile stresses. The micro-cracks usually nucleate along the slip markings in the ferrite phase. Similar results were obtained for M Balbi et al. (2009) for 475 ^{0} C embrittled samples. From analyzing the dislocation structure and the structure associated with the strain localization, we can conclude the fact that whether micro-cracks nucleate first at phase or grain boundaries. From the microstructure as seen in Figure 4.46 it is clear that there is a discontinuity of plane in the interface between the matrix and the slip bands through which there is an abrupt dislocations distribution. Thus, these interfaces act as a preferential nucleation site for micro-cracks under cyclic loading in the free surface grains. Whereas in the interior grains, the slip bands form along the grain boundaries as shown in the Figure 4.52 and the crack nucleation with the increase in stress concentration. Depending on the slip band density and the austenite-ferrite phase boundary strength, the intersection point may form the micro-crack nucleation site.

With the increase in cyclic loading the mechanical twins with the thin lamellae appear very quickly. Twinning occurs because of the partial movement of dislocations and the stress required for causing twinning is dependent on the source of the dislocation and the surface tension of the twin boundary. Therefore, stress required to cause twinning is greater than that of the slip. Hence, in this harder ferrite matrix the critical shear stress for slip increases and then twinning is more likely because the general stress level which is required for the deformation twinning is higher. As seen in the Figure 4.49 and 4.50 twin nucleation is strongly locked with dislocations. Hence twins once they are formed, they themselves act as a barrier like grain boundaries.

The simple mechanism where glide dislocations are converted into micro-cracks is that dislocation pile-up against the twin interface. Then the applied stress pushes the dislocations together to form a crack. This could also explain the high density micro-crack nucleation of the slip bands over the entire strained area of the sample. In summary, the micro-crack first initiates in the ferrite phase because of the sudden nucleation of micro twins. The twinning is driven by high applied stresses which is a consequence of the hardened ferrite matrix. In the Figure 4.48 we can see ferrite phase having single slip and austenite phase having double slips hence crack propogation rates from the grain boundaries will be different. Düber et al.

(2006) reported that α/γ phase boundary offers more resistance to slip transfer as compared to α/α and γ/γ grain boundaries

Fractured surface of the aged and re-aged samples as seen in the Figure 4.53 and 4.54 has undergone brittle fracture. The failure surface is essentially covered with transgranular brittle grains containing crystallographic rivers and numerous secondary cracks. The fracture changes its morphology when crack crosses the ferritic phase to austenitic phase.

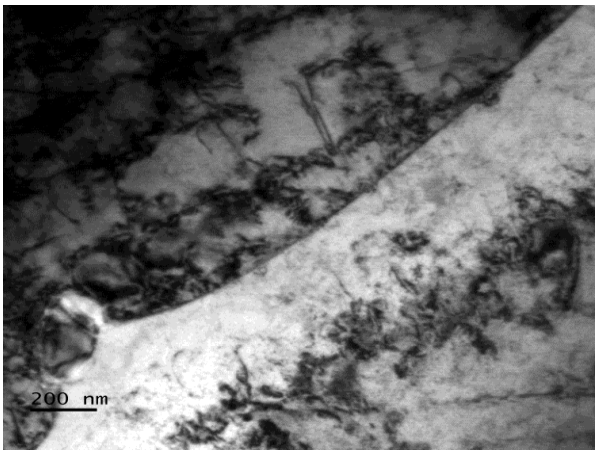

Figure 4.47 TEM image of aged HCF sample stressed at 700 Mpa.

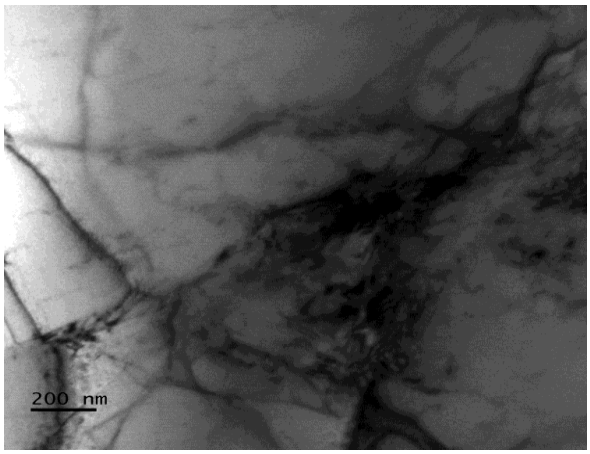

Figure 4.48 TEM image of aged HCF sample stressed at 700 Mpa.

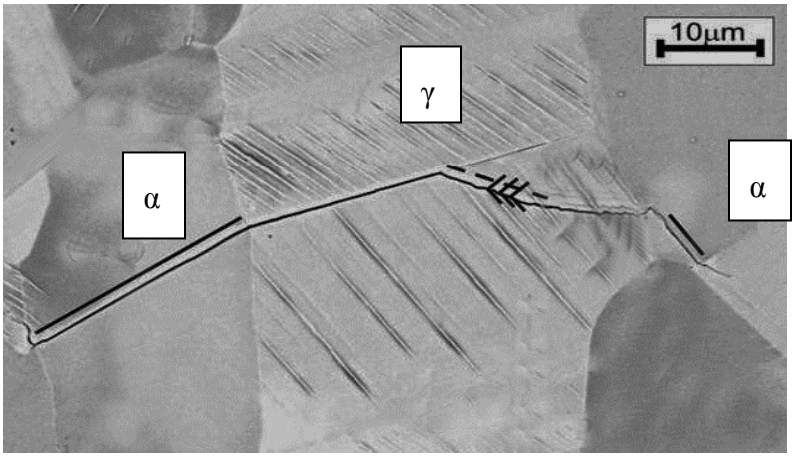

Figure 4.49 SEM image of Aged fatigue sample showing path of short cracks propogating from ferrite to austenite.

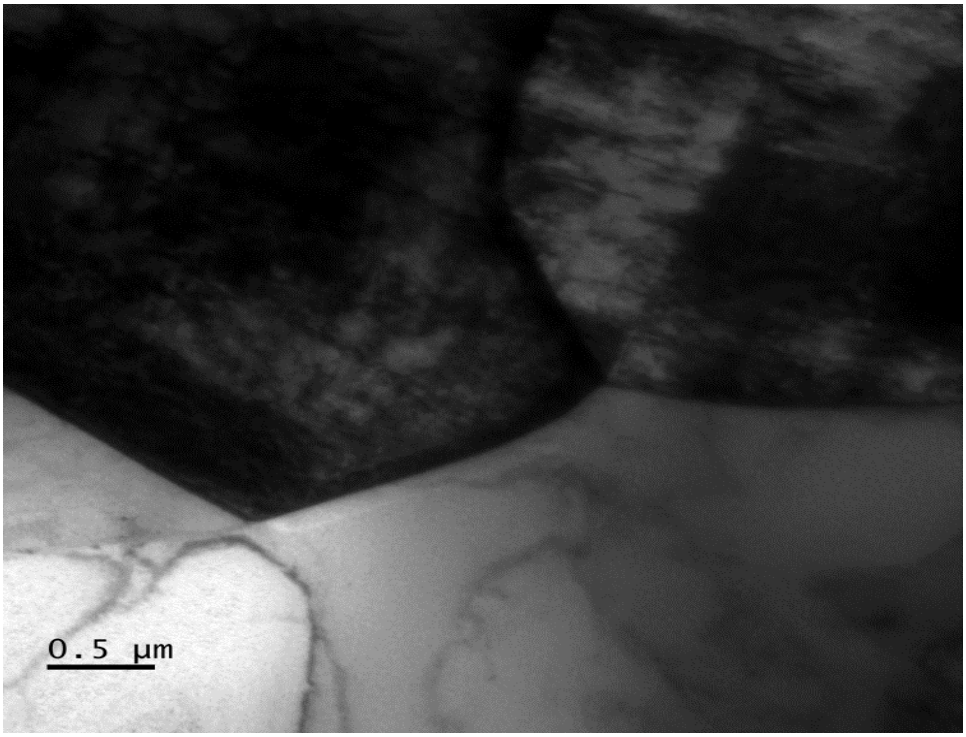

Figure 4.50 TEM image of aged HCF sample stressed at 700 MPa.

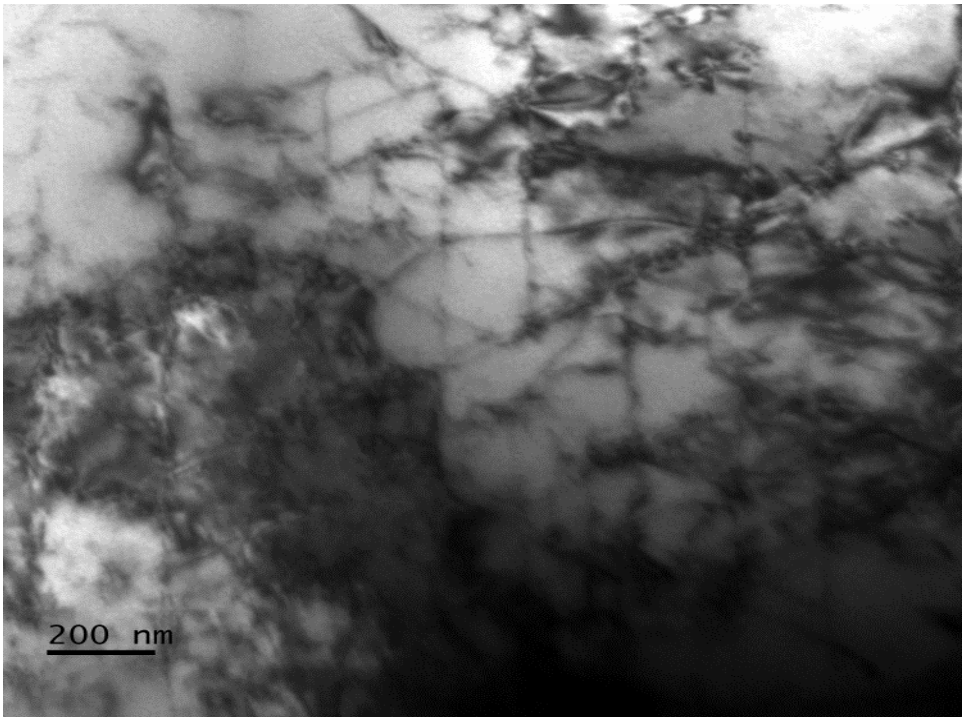

Figure 4.51 TEM image of aged HCF sample stressed at 700 MPa (arrays of microtwins with dislocations distribution in ferrite matrix).

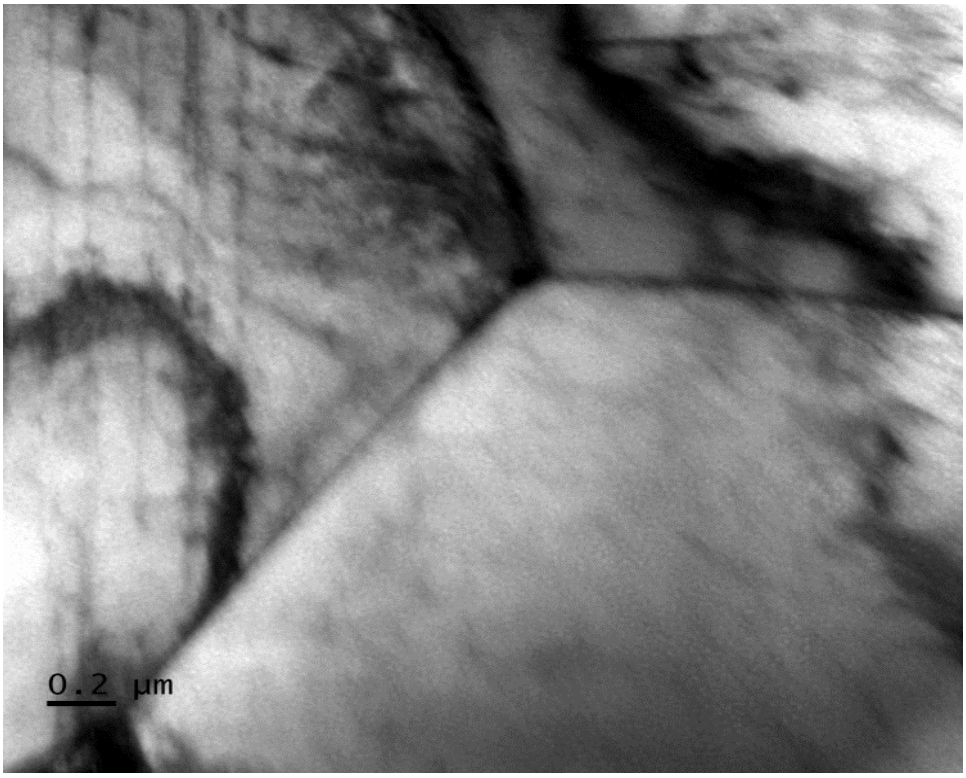

Figure 4.52 TEM image of HCF aged sample stressed at 700 MPa.

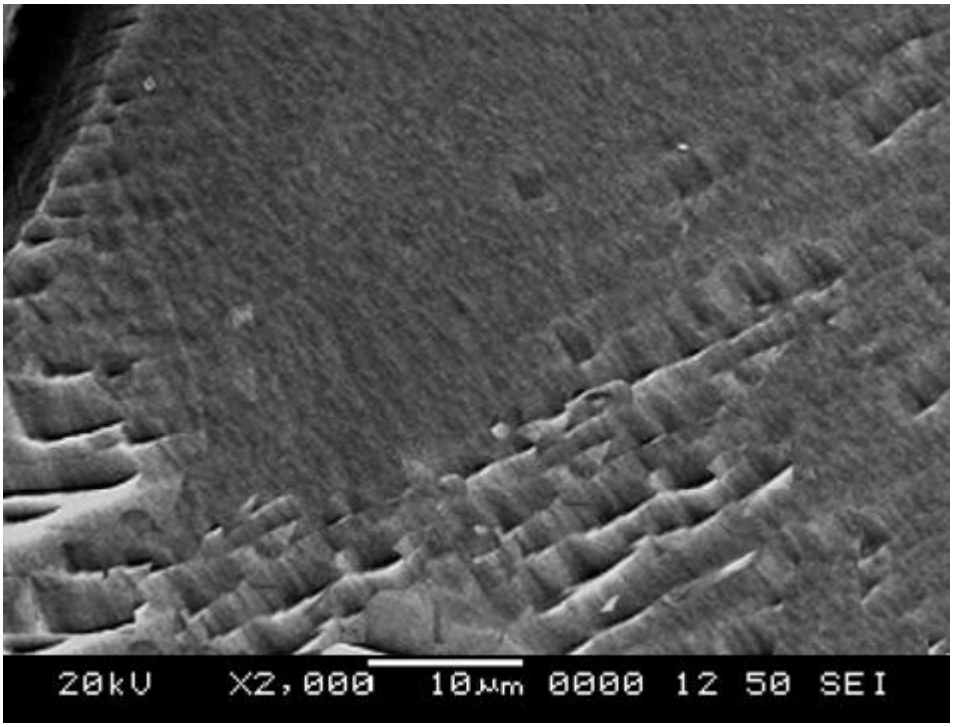

Figure 4.53 SEM image of aged ferrite matrix stressed at 700 MPa.

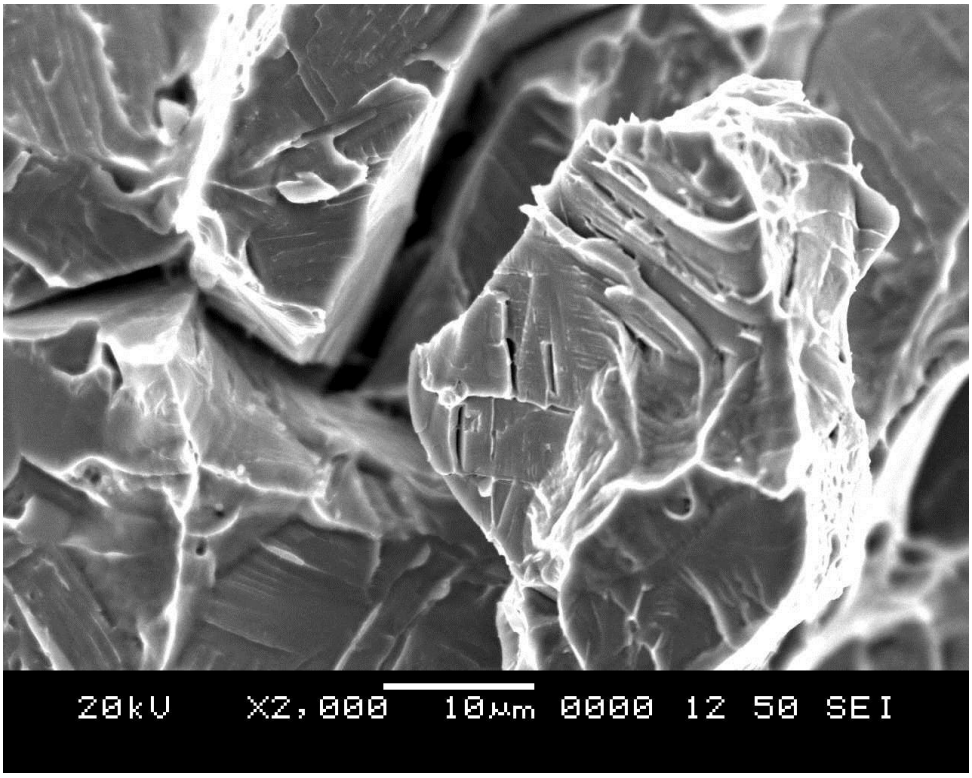

Figure 4. 54 Fracture surface of the aged HCF sample stressed at 700 MPa.

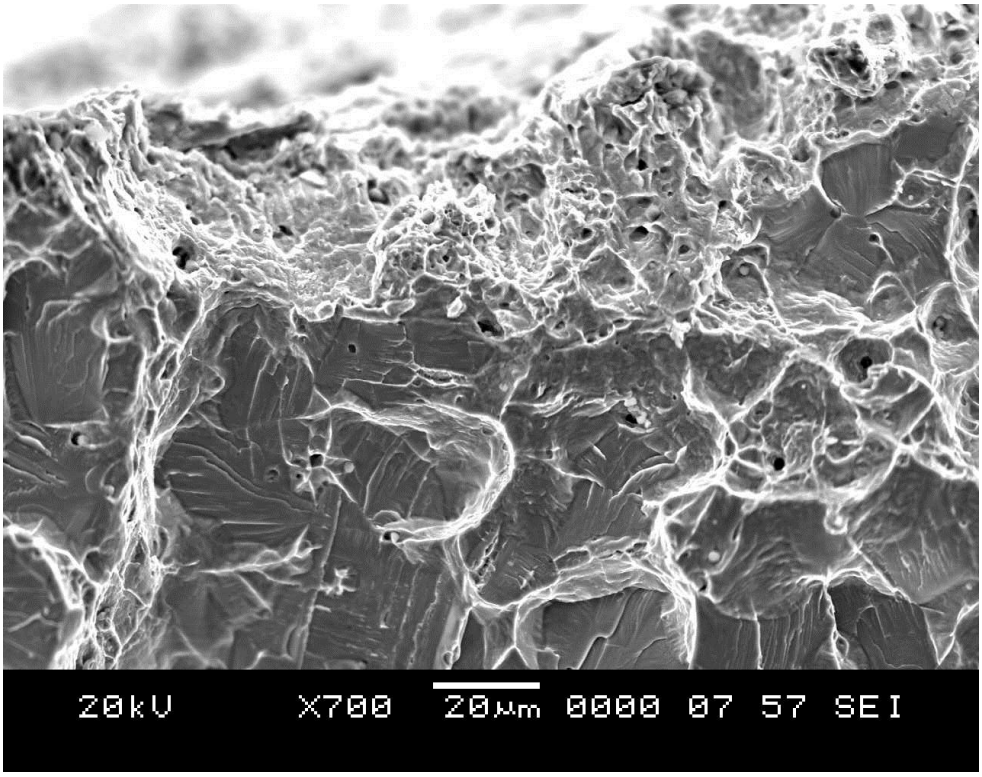

Figure 4.55 Fracture surface of the re-aged HCF sample stressed at 700 MPa.

Chapter 5 Conclusions and Future aspects

The results from transmission electron microscopy studies lead to the following conclusions.

1. The ageing treatment at 475 ^{0} C results in the precipitation of Fe-rich α and Cr-rich α' precipitate because of the spinodal decomposition. Also Cr_2N precipitates were seen in the aged ferritic matrix.

2. After reversion heat treating at 550^{0} C for 60 minutes the alpha-prime precipitates was completely dissolved and some Mo rich precipitates was found near the ferrite grain boundary.

3. Reversion heat treating at 550^{0} C for 120 minutes again leads to the embrittlement of the ferritic matrix because of the formation of R-phase throughout the ferritic matrix. Hence 60 minutes was the ideal reversion heat treatment time.

4. Re-ageing the 60 minutes RHTd samples at 475 ^{0} C for 100 hours the spinodal decomposition again remained as the primary mechanism in the ferritic phase.

5. In re-aged heat treated condition Cr_2N precipitates was found near the ferrite phase boundary and also found penetrated into austenite phase near its grain boundary.

The results from the study of aging, reversion and reading heat treatment by electron microscopy and routine mechanical tests leads to the following conclusions:

1. In aged condition (475 ºC for 1000 hours), the yield strength was increased by 56% and ultimate tensile strength was increased by 60% accompanied by 55% loss in ductility. The strain hardening exponent n, also reached a minimum value of 0.16 and this can be attributed to the formation of the Fe-rich α and Cr-rich α-prime precipitates in the ferritic phase which reduced ductility and increased the resistance to the neck formation.

2. Samples when reversion heat treated at 550 ºC for 60 minutes had a maximum restorative effectiveness that is 87.3% for yield strength, 95.3% for ultimate tensile strength, 86.4% for ductility and the strain hardening exponent “n”, reached a peak

value which was almost equal to the solutionized because ferrite gets homogenized at this elevated temperature which is above (α+α') miscibility gap. In other words Cr-rich alpha prime and Fe-rich alpha precipitates gets dissolved into the ferritic phase.

3. Extending the reversion time beyond 60 minutes lead to the increase in strength and decrease in ductility and the "n" value mainly because of the formation of secondary austenite and R-phase. These precipitates acted as dislocation substructures during reversion heat treatment which inturn affected the deformation behavior.

4. The restorative effectiveness of 100% could not be achieved by the reversion heat treatment because of the residual inhomogeneties which arise in the ferrite phase due to Cr and Mo atoms which are part of precipitates not being redistributed. However, it was found that a reversion heat treatment of 60 minutes yielded optimum results in terms of recovery of tensile properties.

The results from the study of high cycle fatigue behavior of duplex stainless steels in annealed, aged, reversion heat treated and re-aged condition by mechanical testing and electron microscopy lead to the following conclusions.

1. The fatigue strength of S2205-DSS is sensitive to the heat treatment condition. In the present investigation aged and re-aged samples had high fatigue strength than when compared to that of the annealed and reversion heat treated samples.

2. In annealed and reversion heat treated condition initially single slips were mainly found in the ferrite phase because of the difference in the strain hardening rate. Since there is no much difference in the hardness between ferrite and austenite under certain stress levels the strain hardening in the austenite makes it a stronger phase which is more resistant to plastic deformation under cyclic loading. Hence double slips were found in both the phases.

3. Nucleation and the growth of the micro crack in the annealed state is the generation of persistent slip bands which formed the sites for micro crack propagation. Whereas in the embrittled state the micro crack first initiated in the ferrite matrix because of

the sudden nucleation of micro twins and this twinning is driven by the applied stresses which is the consequence of the hardened ferrite.

4. In all heat treated condition the major resistance to crack growth came from α/γ phase boundaries because α/γ phase boundary offers more resistance to the slip transfer as compared to α/α and γ/γ grain boundaries.

Application

Reversion heat treating the S2205 DSS samples at 550 ^{0} C is the optimum heat treatment condition to extend the service life of long term working duplex stainless steel components i.e., variety of primary pressure boundary components of nuclear power plants, such as valves, pressure vessel components, pump bodies and pipes.

Some gap areas of immediate future research could be:

1. Studying the effect of reversion heat treatment on corrosion resistance and in-situ crack initiation studies during fatigue test.
2. The study of effect of initial grain size on the fatigue behavior during aging and reversion heat treatment.
3. A comprehensive study of the influence of alloying elements on thermodynamics and kinetics of aging in the ferritic phase of wrought grades of laboratory melt DSS.

References

Adhe, K.N., Kain, V., Madangopal, K. and Gadiyar, H.S (1996). Influence of Sigma phase formation on the Localized Corrosion Behavior of a Duplex Stainless Steel. *Journal of Materials Engineering and Performance*, *5*(4), 500-506.

Ager, F. J., Elmrabet, S., Paúl, A., Cea-Naharro, Á., Ynsa, M. D., Respaldiza, M. A., and Odriozola, J. A. (2002). Determination of nitrogen in metallic phases using the 14N (d, pγ) 15 N nuclear reaction. *Nuclear Instruments and Methods in Physics Research Section B: Beam Interactions with Materials and Atoms*, *188*(1), 96-101.

Akdut, N. (1999). Phase morphology and fatigue lives of nitrogen alloyed duplex stainless steels, *International Journal of Fatigue*, 21, S97-103.

Alvarez-Armas, I. and Degallaix-Moreuil, S., eds. (2009). *Duplex Stainless Steels*, John Wiley and Sons, Inc., New Jersey.

Alvarez-Armas, I., Marinelli, M. C., Herenu, S., Degallaix, S., and Armas, A. F. (2006). On the cyclic softening behavior of SAF 2507 duplex stainless steel. *Acta materialia*, *54*(19), 5041-5049.

Alvarez-Armas, I., Marinelli, M. C., Malarrı, J. A., Degallaix, S., and Armas, A. F. (2007). Microstructure associated with crack initiation during low-cycle fatigue in a low nitrogen duplex stainless steel. *International Journal of Fatigue*, *29*(4), 758-764.

Alvarez-Armas, I. and Degallaix-Moreuil, S., eds. (2009). Duplex Stainless Steels, John Wiley and Sons, Inc., New Jersey.

Anson, D.R., Pomfret, R.J., Hendry, A. and Beattie, G.T (1994). Castable High-Nitrogen Duplex Stainless Steels: in *The Institute of British Foundrymen 91st Annual Conference. Castcon.*

ASTM A370-14, Standard Test Methods and Definitions for Mechanical Testing of Steel Products, ASTM International, West Conshohocken, PA, 2014.

ASTM E23-12c, Standard Test Methods for Notched Bar Impact Testing of Metallic Materials , ASTM International, West Conshohocken, PA, 2012.

ASTM E8 / E8M-15a, Standard Test Methods for Tension Testing of Metallic Materials, ASTM International, West Conshohocken, PA, 2015.

Atamert S. (1992). Super Duplex Stainless Steels Part I: Heat Affected Zone Microstructure. *Materials Science and Technology, 8*(10), 896-911.

Atamert, S., and King, J. E. (1993). Sigma-phase formation and its prevention in duplex stainless steels. *Journal of materials science letters, 12*(14), 1144-1147.

Baker, H. (1992). Introduction to alloy phase diagrams. *Materials Park, OH: ASM International, 1992. 1. 1*.

Balbi, M., Avalos, M., El Bartali, A., and Alvarez-Armas, I. (2009). Microcrack growth and fatigue behavior of a duplex stainless steel. *International Journal of Fatigue*, *31*(11), 2006-2013.

Blackburn, M.J. and Nutting, J., (1964) "Metallography of Fe-21%Cr alloy subjected to 457 ºCembrittlement", *Journal of the Iron and Steel Institute*, 202, 610-613.

Bliznuk, T., Mola, M., Polshin, E., Pohl, M., and Gavriljuk, V. (2005). Effect of nitrogen on short-range atomic order in the feritic δ phase of a duplex steel.*Materials Science and Engineering: A*, *405*(1), 11-17.

Bonnet, S., Bourgoin, J., Champredonde, J., Guttmann, D., and Guttmann, M. (1990). Relationship between evolution of mechanical properties of various cast duplex stainless steels and metallurgical and aging parameters: outline of current EDF programmes. *Materials Science and Technology*, *6*(3), 221-229.

Brown, J. E., and Smith, G. D. W. (1991). Atom probe studies of spinodal processes in duplex stainless steels and single-and dual-phase Fe-Cr-Ni alloys. *Surface Science*, *246*(1), 285-291.

Bugat, S., Besson, J., Gourgues, A. F., N'Guyen, F., and Pineau, A. (2001). Microstructure and damage initiation in duplex stainless steels. *Materials Science and Engineering: A*, *317*(1), 32-36.

Cahn, J. W. (1961). On spinodal decomposition. *Acta metallurgica*, *9*(9), 795-801.

Chandra, D., and Schwartz, L. H. (1971). Mössbauer effect study of the 475‡ C decomposition of Fe-Cr. *Metallurgical Transactions*, *2*(2), 511-519.

Charles, J. (1994), Structure and Mechanical Properties of Duplex Stainless Steels: In *Duplex Stainless Steels 94.*

Charles, J. (1995). Composition and Properties of Duplex Stainless Steel: in *the World. 36*, 43-55.

Charles, J. (1997) Why and Where Duplex Stainless Steels: *5th World Duplex Stainless Steels*.

Charles, J. (2000) How to Improve Suplex Stainless Steel Properties with Copper Addition: *in 6th World Duplex Stainless Steels. Venezia, Italy*.

Chen, T.H.; Weng, K.L. and Yang, J.R. (2002). "The effect of high-temperature exposure on the microstructural stability and toughness property in a 2205 duplex stainless steel." *Mat. Sci. Eng. A.*, 338, 259-270.

Chung, H. M. (1992). Aging and life prediction of cast duplex stainless steel components. *International journal of pressure vessels and piping*, *50*(1), 179-213.

Chung, H.M. and Chopra, O.K. (1990). "Characterization of Duplex Stainless Steels by TEM, SANS and APFIM Techniques." *Characterization of Advanced Materials*, Altergott, William and Henneke, Edmund, eds., Springer Science+Business Media, New York, 123-147.

Cortie, M. B., and Pollak, H. (1995). Embrittlement and aging at 475 C in an experimental ferritic stainless steel containing 38 wt.% chromium. *Materials Science and Engineering: A*, *199*(2), 153-163.

Culity, B. D., and Stock, S. R. (1978). Elements of X-ray Diffraction. *Reading: Addition-Wesley*.

Davis, Joseph R. (1994). *Stainless Steels*, ASM International.

Davison, (1990), Practical Guide to Using Duplex Stainless Steels. *Materials Performance, 29*(1): 57-62.

Devillers-Guerville, L., Besson, J., and Pineau, A. (1997). Notch fracture toughness of a cast duplex stainless steel: modelling of experimental scatter and size effect. *Nuclear Engineering and Design*, *168*(1), 211-225.

Devillers-Guerville, L., Besson, J., and Pineau, A. (1997). Notch fracture toughness of a cast duplex stainless steel: modelling of experimental scatter and size effect. *Nuclear Engineering and Design*, *168*(1), 211-225.

Druce, S. G., Gage, G., and Popkiss, E. (1988). Effects of notch geometry on the impact fracture behaviour of a cast duplex stainless steel. *International journal of pressure vessels and piping*, *33*(1), 59-81.

Düber, O., Künkler, B., Krupp, U., Christ, H. J., and Fritzen, C. P. (2006). Experimental characterization and two-dimensional simulation of short-crack propagation in an austenitic–ferritic duplex steel. *International Journal of Fatigue*, *28*(9), 983-992.

Düber, O. (2007). *Investigations on the propagation behavior of microstructural short-term fissures in two-phase metallic materials using the example of austenitic-ferritic duplex steel* (Doctoral dissertation, Dissertation). VDI-Verlag.

Farrar, R.A. (1995). The Importance of Microstructural Transformations for Welding and the Stability of Long Term Service Properties: Welding in the World, 36, 143-151.

Fisher, R. M., Dulis, E. J., and Carroll, K. G. (1953). Identification of the precipitate accompanying 885 F embrittlement in chromium steels. *Trans. AIME*, *197*(5), 690-695.

Garfisa-Mesias, L.F., Sykes, J.M. and Tuck, C.D.S. (1996). The Effect of Phase Compositions on the Pitting Corrosion of 25 Cr Duplex Stainless Steel in Chloride Solutions: *Corrosion Science, 38*(8) 319-1330.

Gironès, A., Llanes, L., Anglada, M., and Mateo, A. (2004). Dynamic strain ageing effects on superduplex stainless steels at intermediate temperatures. *Materials Science and Engineering: A, 367*(1), 322-328.

Gironès, A., Villechaise, P., Mateo, A., Anglada, M., and Méndez, J. (2004). EBSD studies on the influence of texture on the surface damage mechanisms developed in cyclically loaded aged duplex stainless steels. *Materials Science and Engineering: A, 387*, 516-521.

Goh, C. S., and Yip, T. H. (2002). Fatigue deformation-induced response in a superduplex stainless steel. *Metallurgical and Materials Transactions A*, *33*(11), 3433-3442.

Grobner, P. J. (1973). The 885 F (475 C) embrittlement of ferritic stainless steels. *Metallurgical transactions*, *4*(1), 251-260.

Gunn, R. N. (1997). *Duplex stainless steels: microstructure, properties and applications*. Woodhead Publishing.

Hansen, M. and Anderko, K., (1958) *Constitution of Binary Alloys*, McGraw-Hill, p. 527.

Hertzman, S., Nilsson, M., and Jargelius-Pettersson, R. (1994). Influence of W and Cu on Microstructure, Mechanical Properties and Corrosion Resistance in Super Duplex Weld Metals. *In Proceedings Conference Duplex Stainless Steels(Vol. 94).*

Hilders, O. A., Ramos, M., Peña, N. D., and Sáenz, L. (1999). Effect of 475 C embrittlement on fractal behavior and tensile properties of a duplex stainless steel. *Journal of materials engineering and performance*, *8*(1), 87-90.

Hoffmeister, H. (1994). Effects of Chemical Composition of Duplex Stainless Steels on Microstructure and Pitting Corrosion after Solution Heat Treatment and Various Weld Simulation Cooling Cycles: *Welding in the World, 33*(2), 18-23.

Hwang, T. H., Kim, J. H., Kim, K. H., Moon, W. J., and Kang, C. Y. (2014). Effect of R-phase on impact toughness of 25Cr-7Ni-4Mo super duplex stainless steel.*Metals and materials international*, *20*(1), 13-17.

J.E. Hilliard. H.I. Aaronson (Ed.) (1970). Phase Transformations, American Society for Metals, Metals Park, Ohio

Jang, H., Hong, S., Jang, C., and Lee, J. G. (2014). The effects of reversion heat treatment on the recovery of thermal aging embrittlement of CF8M cast stainless steels. *Materials and Design*, *56*, 517-521.

Jayet-Gendrot, S., Gilles, P., and Migné, C. (2000). Behavior of duplex stainless steel casting defects under mechanical loadings. *Nuclear Engineering and Design*, *197*(1), 141-153.

Jayet-Gendrot, S., Ould, P., and Meylogan, T. (1998). Fracture toughness assessment of in-service aged primary circuit elbows using mini-CT specimens taken from outer skin. *Nuclear engineering and design*, *184*(1), 3-11.

Johansson, J., and Odén, M. (2000). Load sharing between austenite and ferrite in a duplex stainless steel during cyclic loading. *Metallurgical and Materials Transactions A*, *31*(6), 1557-1570.

Johnson Jr, A. B., Sundaram, S. K., and Garner, F. A. (2001). Program plan for acquiring and examining naturally aged materials and components from nuclear reactors. *Pacific Northwest National Laboratory, Richland, WA, PNNL-13930*.

Josefsson, B., Nilsson, J. O., and Wilson, A. (1991). Phase transformations in duplex steels and the relation between continuous cooling and isothermal heat treatment. *Duplex Stainless Steels'91*, *1*, 67-78.

Karlsson, L. (1999). Intermetallic phase precipitation in duplex stainless steels and weld metals: Metallurgy, influence on properties, welding and testing aspects.

Kawaguchi, S., Sakamoto, N., Takano, G., Matsuda, F., and Kikuchi, Y. (1997). Microstructural changes and fracture behavior of CF8M duplex stainless steels after long-term aging. *Nuclear engineering and design*, *174*(3), 273-285.

Kazior, J.; Nykiel, M.; Pieczonka, T.; Puscas, T.M. and Molinari, A. (2004). "Activated Sintering of P/M Duplex Stainless Steel Powders." *J. Mater. Process. Tech.*, 157-158, 712-717.

Ki Leuk Lai, J.; Shek, H.S. and Ho Lo, K., eds. (2012). *Stainless Steels: An Introduction and their Recent Developments*, Bentham Science Publishers, Sharjah.

Kokawa, H., STORY, E., and North, T. H. (1995). Nitride precipitation in duplex stainless steel weld metal: *ISIJ international*, *35*(10), 1277-1283.

Konosu, S. (1992). Effect of reversion heat treatments on the mechanical properties of a 13% Cr steel subjected to 475° C embrittlement. Scripta *Acta Metall. Mater.*, *26*(10), 1631-1636.

Kotecki. (1989). Heat Treatment of Duplex Stainless Steel Weld Metals: *Welding Journal. 68*(11), 431s-441s.

Kuroda, T., and Matsuda, F. (1994). Role of Secondary Austenite on Corrosion and Stress Corrosion Cracking of Sensitized Duplex Stainless Steel Weldments (Materials, Metallurgy and Weldability). *Transactions of JWRI*, *23*(2), 205-211.

Kyung-Ho, P., Lasalle, J. C., and Schwartz, L. H. (1985). The low cycle fatigue behavior of spinodally decomposed Fe□ 26Cr□ 1Mo alloys. *Acta Metallurgica*, *33*(2), 205-211.

Lai, J.K.L., Wong, K.W. and Li, D.J. (1995), Effect of Solution Treatment on the Transformation Behavior of Cold 207 Rolled Duplex Stainless Steels. *Materials Science and Engineering A*, *203*(1-2), 356-364.

Le Delliou, P., Julisch, P., Hippelein, K., and Bezdikian, G. (1999). Analysis of a bending test on a full-scale PWR hot leg elbow containing a surface crack. *Nuclear engineering and design*, *193*(3), 273-282.

Li, S. L., Zhang, H. L., Wang, Y. L., Li, S. X., Zheng, K., Xue, F., and Wang, X. T. (2013). Annealing induced recovery of long-term thermal aging embrittlement in a duplex stainless steel. *Materials Science and Engineering: A*, *564*, 85-91.

Lippold, John C. and Kotecki, Damien J. (2005). *Welding Metallurgy and Weldability of Stainless Steels*, John Wiley and Sons, Inc., New Jersey.

Llanes, L., Mateo, A., Iturgoyen, L., and Anglada, M. (1996). Aging effects on the cyclic deformation mechanisms of a duplex stainless steel. *Acta materialia*, *44*(10), 3967-3978.

Llanes, L., Mateo, A., Violan, P., Méndez, J., and Anglada, M. (1997). On the high cycle fatigue behavior of duplex stainless steels: Influence of thermal aging. *Materials Science and Engineering: A*, *234*, 850-852.

Machado, (1996). *Precipitation Behavior of 25% Cr - 5.5 Ni Austenitic Stainless Steel Containing 0.87% Nitrogen.* Steel Research. 67(7), 285-290

Mateo, A., Gironès, A., Keichel, J., Llanes, L., Akdut, N., and Anglada, M. (2001). Cyclic deformation behaviour of superduplex stainless steels. *Materials Science and Engineering: A*, *314*(1), 176-185.

Mateo, A., Llanes, L., Anglada, M., Redjaimia, A., and Metauer, G. (1997). Characterization of the intermetallic G-phase in an AISI 329 duplex stainless steel. *Journal of materials science*, *32*(17), 4533-4540.

Mateo, A., Palomino, J. L., Salan, N., Llanes, L., and Anglada, M. (1996). Mechanical evaluation of a reversion heat treatment for a duplex stainless steel thermally embrittled. *ECF 11--Mechanisms and Mechanics of Damage and Failure.*, *1*, 1996.

Mathew, M. D., Lietzan, L. M., Murty, K. L., and Shah, V. N. (1999). Low temperature aging embrittlement of CF-8 stainless steel. *Materials Science and Engineering: A*, *269*(1), 186-196.

Miller, M. K., and Russell, K. F. (1996). Comparison of the rate of decomposition in Fe-45% Cr, Fe- 45% Cr and 5% Ni and duplex stainless steels. *Applied surface science*, *94*, 398-402.

Miller, M. K., Beaven, P. A., Lewis, R. J., and Smith, G. D. W. (1978). Atom probe microanalytical studies of some commercially important steels. *Surface Science*, *70*(1), 470-484.

Miller, M.K. and Bentley, J., (1990) “APFIM and AEM investigation of CF8 and CF8M primary coolant pipe steels”, *Materials Science and Technology*, 6, 285-292.

Miura, M., Koso, M., Kudo, T., and Tsuge, H. (1990). The effects of nickel and nitrogen on the microstructure and corrosion resistance of duplex stainless steel weldments. *Welding International*, *4*(3), 200-206.

Nilsson, J. O., Huhtala, T., Jonsson, P., Karlsson, L., and Wilson, A. (1996). Structural stability of super duplex stainless weld metals and its dependence on tungsten and copper. *Metallurgical and Materials Transactions A*, *27*(8), 2196-2208.

Nilsson, J.O. (1992), Overview: Super Duplex Stainless Steels. Materials *Science and Technology*. *8*(8), 686-700.

Nyström, M., and Karlsson, B. (1996). Fatigue of duplex stainless steel influence of discontinuous, spinodally decomposed ferrite. *Materials Science and Engineering: A*, *215*(1), 26-38.

Ogawa, K., Okamoto, H., Ueda, M., Igarashi, M., Mori, T., and Kobayashi, T. (1996). *Effects of tungsten on pitting corrosion resistance and impact toughness in the HAZ of duplex stainless steel- study of weldability of high- tungsten duplex stainless steel (1st Report)*.

Ogawa, T., Koseki, T., and Inoue, H. (1990). Weld Phase Chemistries of Duplex Stainless Steels. *Weldability of Materials*.

P. V. Scheers. J.K., R. Paton.(2000) Characterization of A 20Cr-Ni Duplex Stainless Steel with Additions of Manganese and Nitrogen. in *6th World Duplex Stainless Steel,* Venezia, Italy.

R.O. Williams, H.W. Paxton, The nature of ageing of binary iron-chromium alloys around 500oC, J. Iron Steel Inst. 185 (1957) 358-374.

R.O. Williams. (1958). Further studies of the Iron-chromium system.Trans. TMS-AIME, 212, 497–502.

Ramirez, A. J., Lippold, J. C., and Brandi, S. D. (2003). The relationship between chromium nitride and secondary austenite precipitation in duplex stainless steels. *Metallurgical and materials transactions A*, *34*(8), 1575-1597.

Redjaimia, A., Metauer, G., and Gantois, M. (1991). Decomposition of Delta Ferrite in an Fe--22 Cr--5 Ni--3 Mo--0.03 C Duplex Stainless Steel. A Morphological and Structural Study. *Duplex Stainless Steels'91*, 1, 119-126.

Russell, S. W., and Lundin, C. D. (2005). The Development of Qualification Standards for Cast Duplex Stainless Steel.

S. Bonnet, J. Bourgoin, J. Champredonde, D. Guttmann, M. Guttmann. (1990). Relationship between evolution of mechanical properties of various cast duplex steel and metallurgical and aging parameter: outline for current EDF programmes. *Materials Science and Technology*, *6*, 221–229.

S. K. Ahn, K.T.K., Y. H. Lee and Y. D. Lee. (2000). Develepoment of a New Type of Duplex Stainless Steel: in 6th World Duplex Stainless Steel. Venezia, Italy.

Sahu, J. K. (2008). *Effect of 475 ºC embrittlement on the fatigue behaviour of a duplex stainless steel* (Doctoral dissertation, University Siegen).

Sahu, J. K., Krupp, U., Ghosh, R. N., and Christ, H. J. (2009). Effect of 475 C embrittlement on the mechanical properties of duplex stainless steel. *Materials Science and Engineering: A*, *508*(1), 1-14.

Sahu, J. K., Krupp, U., Ghosh, R. N., and Christ, H. J. (2009). Effect of 475 C embrittlement on the mechanical properties of duplex stainless steel. *Mater. Sci. Eng: A*, *508*(1), 1-14.

SCRATA Materials Fact Sheets on Duplex Cr-Ni Steels, Section D, April 1991.

Singh Raman, R.K. and Siew, W.H. (2010). "Role of nitride addition in chloride stress corrosion cracking of a Super Duplex Stainless Steel." *Corrosion Science*, 52, 113-117.

Solomon, H. D., and Levinson, L. M. (1978). Mössbauer effect study of '475 C embrittlement' of duplex and ferritic stainless steels. *Acta Metallurgica*, *26*(3), 429-442.

Soylu, B.(1991). Microstructural Refinement of Duplex Stainless Steels. *Materials Science and Technology, 7*(2), 137-145.

Sriram, R.(1989). Pitting Corrosion of Duplex Stainless Steels. *Corrosion, 45*(10), 804-810.

Stolarz, J., and Foct, J. (2001). Specific features of two phase alloys response to cyclic deformation. *Materials Science and Engineering: A, 319*, 501-505.

Taisne, A., Decamps, B., and Priester, L. (2006). Role of interfaces in duplex stainless steel deformation micromechanisms. *Composite Interfaces, 13*(1), 89-102.

Takemoto, T., Mukai, K., and Hoshino, K. (1986). Effect of nitrogen on low cycle fatigue behavior of austenitic stainless steel. *Transactions of the Iron and Steel Institute of Japan, 26*(4), 337-344.

Taylor, R. (1994). *Duplex Stainless Steel Production:* in *SFSA TandO conference*.

Technical Report of International Atomic Energy Agency. (2003). Assessment and management of ageing of major nuclear power plant components important to safety; Primary piping in PWRs, IAEA-TECDOC-1361.

Technical Report of International Atomic Energy Agency. (2003). Assessment and management of ageing of major nuclear power plant components important to safety; PWR vessel internals, *IAEA-TECDOC-1119*.

Thorvaldsson, T., Nilsson, J. O., and Liu, P. (1991). Microstructural characterization of stainless steel-industrial applications. *Micron and Microscopica Acta, 22(*1), 185-186.

Tujikura, Y., and Urata, S. (1999). Fracture mechanics evaluation of cast duplex stainless steel after thermal aging. *Nuclear engineering and design, 191*(2), 255-261.

Vannevik, H., Nilsson, J. O., Frodigh, J., and Kangas, P. (1996). High Nitrogen Steels. Effect of Elemental Partitioning on Pitting Resistance of High Nitrogen Duplex Stainless Steels. *ISIJ International, 36*(7), 807-812.

Vogt, J. B., Massol, K., and Foct, J. (2002). Role of the microstructure on fatigue properties of 475º C aged duplex stainless steels. *International journal of fatigue,24*(6), 627-633.

Wang, X. G., Dumortier, D., and Riquier, Y. (1991). Structural Evolution of Zeron 100 Duplex Stainless Steel Between 550 and 1100 deg C. *Duplex Stainless Steels'91*, 1, 127-134.

Weng, K. L., Chen, H. R., and Yang, J. R. (2004). The low-temperature aging embrittlement in a 2205 duplex stainless steel. *Materials Science and Engineering: A*, *379*(1), 119-132.

Zieliński, W., Światnicki, W., Barstch, M., and Messerschmidt, U. (2003). Non-uniform distribution of plastic strain in duplex steel during TEM in situ deformation. *Materials chemistry and physics*, *81*(2), 476-479.

LIST OF PUBLICATIONS

1. **Shamanth, V**., and Ravishankar, K. S. (2015). "Dissolution of alpha-prime precipitates in thermally embrittled S2205-duplex steels during reversion-heat treatment". *Results in Physics, 5*, 297-303. (Elsevier Publications, Impact factor- 1.39).
2. **Shamanth, V**, Arun, T. N, and Ravishankar K. S. "Effect of Alpha Prime (A') Precipitate on the Mechanical Properties of Thermally Embrittled S2205 Duplex Stainless Steels". *International Advanced Research Journal in Science, Engineering and Technology* Vol. 2, Issue 5, May 2015. (Status: Published).
3. Natesh, M., **Shamanth, V**., and Ravishankar, K. S. (2015, September). "Effect of Reversion Heat Treatment on the Mechanical Properties of Thermally Embrittled UNS S32760 Duplex Stainless Steel". In *Materials Science Forum* (Vol. 830, pp. 127-130). (Trans Tech Publications, Impact factor- 0.28).
4. **Shamanth, V**., and Ravishankar, K. S. (2016). "Effect of Reversion heat treatment and Re-aging on the Mechanical Properties of S2205 Thermally Embrittled Duplex Stainless Steels". *Materials today proceedings.* Elsevier Publications (Status: Accepted for publication).
5. **Shamanth, V**., and Ravishankar, K. S. (2016). "Effect of Heat Treatment on the High Cycle Fatigue Behaviour of S2205 Duplex Stainless Steels". *Materials today proceedings.* Elsevier Publications (Status: published),
6. **Shamanth, V**., and Ravishankar, K. S. (2016). "Influence of Heat Treatment Temperature on the Microstructure and Mechanical Properties of the Thermally Embrittled S2205 Duplex Stainless Steels" *Journal of Thermal Engineering and Technology Volume 2 Issue 2 Page 1-18. Mantech publications. (Status: Published)*